Inclusive Measurement of the Charm Contribution to the Structure Function of the Proton

Kenan Mujkić

University College London (UCL)

London 2013

Contents

I confirm that the work presented in this thesis is my own. Where information has been derived from other sources, I confirm that this has been indicated in the thesis.

Kenan Mujkić, UCL

London, 2013

Abstract

The inclusive measurement of charm production in deep inelastic scattering with the ZEUS detector at HERA is presented in this thesis. In a first step, the existing algorithm from the inclusive secondary vertexing analysis was generalised using the signed impact parameter of jet-associated tracks to extract the heavy quark content of the data sample, with the beam spot as reference point. In a second step, the algorithm was extended by using the secondary vertex in events containing a well-reconstructed decay vertex, the impact parameter of jet-associated tracks in events not containing a secondary vertex, and a combination of vertexing and tracking information in all other events. The combined tracking and vertexing algorithm has significantly reduced the relative statistical and systematic uncertainties on the measured double differential cross sections in Q^2 and x. The relative statistical error has been reduced by 40 % on average, whilst the systematic uncertainty decreased due to an improved tracking efficiency. In order to extend the kinematic region and further reduce the uncertainty on the extrapolation of the charm contribution, $F_2^{c\bar{c}}$, to the structure function of the proton the cut on the transverse energy for the jet selection has been relaxed from $E_T^{\text{jet}} > 4.2$ GeV to $E_T^{\text{jet}} > 2.5$ GeV. An extrapolation of the measured, visible cross sections to the full kinematic phase space was performed allowing an extraction of $F_2^{c\bar{c}}$ to be made for a well-defined set of points in the x and Q^2 plane. A comparison with previous results shows that lowering the cut on the transverse energy of the selected jets has particularly reduced the uncertainty on the extrapolation in the low Q^2 and low x region. The present analysis is well described by next-to-leading order QCD predictions generated with the HVQDIS program for the extended phase space. At present it is the most precise measurement of charm production cross sections with the ZEUS detector, and will have a significant impact on future combinations of ZEUS and H1 data.

Acknowledgments

First and foremost, I would like to thank my supervisor, Matthew Wing, for his support and supervision during the time I have spent at University College London (UCL). With his brilliant physical intuition he has been a constant source of conceptions throughout the entire time of my PhD. I am thankful to the high energy physics group of UCL for the welcoming atmosphere, in particular to my colleagues, Stephen (M.Sci.) Bieniek, Sam Cook, James Mott, Benjamin Watt and Peter Wijeratne, and I feel obliged to Gordon Crone, Tony Hoare, Erdem Motuk and Matthew Warren for their support in computing. Furthermore, I would like to thank Mark Lancaster for inspiring discussions in the Jeremy Bentham's, some of which also had to do with physics.

The research relevant for the present thesis was performed in close collaboration between the Department of Physics and Astronomy, University College London and the ZEUS collaboration at the Deutsches Elektronen Synchrotron (DESY). Thanks to a joint UCL/DESY studentship I have been able to spend a significant amount of time in Hamburg, allowing for a closer collaboration with members of the ZEUS collaboration. Therefore, I would in the first instance like to thank the directorate of DESY for the generosity of awarding me the studentship and consequently making this thesis possible. I would like to thank the ZEUS collaboration, in particular Achim Geiser, who has been a source of support throughout the entire time I have spent in Germany, and Aharon Levy, as spokesperson of the collaboration. Finally, I would like to thank Olaf Behnke, Vladyslav Libov and Philipp Roloff for the collaboration on the secondary vertexing analysis, and for the welcoming atmosphere they have created. I would also like to thank Ingo Martens, Janusz Szuba and Dorota Szuba for their technical support in computing and simulations.

Last but not least, I would like to thank my friends who have always encouraged me to continue with research and complete a PhD. In particular, I would like to thank Anne-Caroline Allemand, Marcello Borri, Inti Cabredo-Hofherr, Federico Chavez, Yusuf Cökelekoglu, Thomas Danckaert, Fabrice Dikoume Kede, Aziz Dossanov, David Furch and Francesca Regina, Paolo Gandini, Alexander Hasselhuhn, Gintaras Hinz, David Houseman, Thomas Kecker, Oleg Lebedev, Liat Loeffelstiel, Jasmin Lübbe, Janusz Malka, Manuel Mittenzwey, Hayk Pirumov, Angela Romano, Mark Williams and Mohammed Zakaria. Finally, I am thankful

to my house mates Giuseppe Sturiale and Adriano Di Pietrantonio for supporting me during the final stage of the thesis.

Chapter 1

Introduction

The HERA (Hadron Elektron Ring Anlage) accelerator was the world's first and to date only lepton-proton collider, providing a unique facility to perform precision tests of perturbative QCD, and resolve the structure of the proton. A particularly interesting testing ground for perturbative QCD is provided by heavy flavour production, since the heavy quark mass, the photon virtuality and the transverse jet energy provide competing scales in the hard scatter to test theoretical predictions.
In lepton-proton collisions, heavy quarks are produced at leading-order in boson-gluon fusion (BGF), a process sensitive to the gluon density inside the proton. Measurements of heavy quark production cross sections at HERA have therefore the potential to constrain the gluon density inside the proton. These constraints of the parton density functions are of particular interest in a time that the Large Hadron Collider (LHC) has started data taking, since they reduce the model uncertainty of Standard Model predictions in proton collisions.
At HERA different techniques have been applied to measure heavy flavour production in deep inelastic scattering. The best signal-to-background ratio for charm production cross sections is given in the full reconstruction of the D^* meson. On the other hand, the branching ratios are small and the phase space accessible with D^* mesons is restricted, because all decay products of the charmed meson have to be reconstructed. The reconstruction of semi-leptonic decays of charmed hadrons profits from larger branching fractions and a better coverage in polar angle, but suffers from a worse signal-to-background ratio. The advantage of inclusive analyses based on lifetime information is that they are not limited by specific branching fractions, provide the largest phase space coverage and are sensitive to low transverse momenta.
Inclusive measurements of charm quark production in deep inelastic scattering have been performed previously with the ZEUS detector. The standard technique is based on the reconstruction of the decay length significance and secondary vertex mass of heavy flavoured hadrons. The secondary vertex significance is plotted

in bins of the secondary vertex mass, and the negative part of the distribution is subsequently mirrored onto and subtracted from the positive part. This technique enriches the heavy quark contribution, since the heavy flavoured hadrons have a larger asymmetry in the decay length significance distributions than the light flavoured hadrons.
An alternative technique to perform an inclusive measurement is based on the signed impact parameter of jet-associated tracks. The impact parameter is calculated as the distance between beamspot and point of closest approach, and a positive or negative sign is assigned depending on the angle between the line joining the beamspot with the point of closest approach and the heavy quark jet-axis. The events are subsequently categorised according to the absolute value of the impact parameter significance, and the signed track significance is plotted for the different scenarios of the categorisation. In analogy to the secondary vertexing analysis, the negative part of the signed impact parameter significance distributions is then mirrored onto and subtracted from the positive part in order to obtain a charm and beauty enriched sample.
The above mentioned techniques of signal extraction have a comparable statistical precision and similar systematic uncertainties, such that one technique cannot be favoured with respect to the other. However, a combination of secondary vertexing and tracking information allows for a fully inclusive measurement to be made by exploiting information that has not been considered in the individual measurements. Aiming to make the most inclusive measurement of the charm contribution to the structure function of the proton, a novel three-step algorithm will therefore be presented in this thesis. In events that contain a well-reconstructed secondary vertex the decay length significance and secondary vertex mass are used to extract the heavy quark content of the data sample. In events without a well-reconstructed secondary vertex the impact parameter of jet-associated tracks is used for the signal extraction. Finally, in events containing a jet associated to a vertex that did not pass the secondary vertex selection, the signed impact parameter of jet-associated tracks is used additionally for the extraction of the heavy quark content of the data sample. In order to reduce the dependence of the estimated values on the theoretical predictions and obtain sensitivity in the charm mass threshold region the cut on the transverse jet energy was further relaxed compared to previous measurements.
The thesis is organized in the following way: a review of the theoretical background of perturbative QCD and heavy flavour production in deep inelastic scattering at HERA is given in **chapter 2**. The relevant components of the HERA accelerator and the ZEUS detector are discussed in **chapter 3**. The reconstruction of physical observables from measurements of the individual detector components is detailed in **chapter 4**. The event selection and novel technique of signal extraction are discussed in **chapter 5**. The measured differential cross sections are presented and compared to theoretical predictions in **chapter 6**. The estimated values of the charm contribution to the proton structure function are presented

in **chapter 7**. Finally, the conclusions of the present analysis and an outlook are given in **chapter 8**.

Chapter 2

Theoretical Overview

This chapter will provide the theoretical background [1–8] for the inclusive measurement of the charm contribution to the structure function of the proton at HERA. In section 2.1 the theory of strong interactions, quantum chromodynamics (QCD) [9–11], will be introduced. The content of matter and interactions will be derived starting from the fundamental principle of gauge invariance. The renormalisation group equation will be introduced leading to the scale dependence of the theory and consequently to the running of the strong coupling constant [12]. Section 2.2 will explain the fundamental principles of deep inelastic scattering (DIS). In a first step the naive quark parton model [13] and the structure functions which parametrise inclusive DIS cross sections will be introduced. In a second step it will be explained how the scaling behaviour of the theory is broken and logarithmic, collinear and soft divergences arise [14, 15]. Finally, it will be illustrated how these divergences can be absorbed by the technique of renormalisation [16] and the factorisation [17] of the DIS scattering cross sections. In this context the DGLAP evolution equations [18–21] will be illustrated which describe the evolution of the parton densities with the respective scale. In section 2.3 the dominant mechanism for heavy flavour production at HERA will be discussed [22]. It will be illustrated that heavy flavour production allows precision tests of perturbative QCD to be made, by providing a hard scale. Finally, three different schemes will be introduced which allow for the incorporation of heavy flavours within the framework of perturbative QCD [23–40].

2.1 Quantum Chromodynamics (QCD)

Quantum Chromodynamics (QCD) is the theory of the strong interaction [9–11], one of the four fundamental forces in nature. The $SU(3)$ invariant gauge theory describes the interaction between quarks and gluons, and explains how these bind together to form hadrons. The Feynman rules required to perform a perturbative

calculation in QCD can be derived from the Lagrangian [5–8]:

$$\mathcal{L}_{classical} + \mathcal{L}_{gauge} + \mathcal{L}_{ghost}. \tag{2.1}$$

For a discussion of the gauge fixing term the reader is referred to [1–7], and of the ghost field term to [41]. The Faddeev-Popov ghosts arise upon quantisation, and cancel unphysical degrees of freedom that would otherwise propagate in covariant gauges. The classical Lagrangian is invariant under local $SU(3)$ transformations, and describes the interaction of spin-$\frac{1}{2}$ particles of mass m and massless spin-1 gauge fields, the gluons:

$$\mathcal{L}_{classical} = -\frac{1}{4} F^A_{\alpha\beta} F^{\alpha\beta}_A + \sum_{flavour} \bar{q}_a (i\not{D} - m)_{ab} q_b, \tag{2.2}$$

where $\not{D} = \gamma_\mu D^\mu$, the index A runs over the eight colour degrees of freedom, and the spinor indices of γ_μ and q_a are suppressed. Under a $SU(3)$ gauge transformation the quark fields q_a transform in the following way:

$$q_a(x) \to q'_a(x) = \exp(i\, t \cdot \theta(x))_{ab}\, q_b(x) \equiv \Omega(x)_{ab}\, q_b(x), \tag{2.3}$$

where t are the generators of the fundamental representation that fulfill

$$[t^A, t^B] = i f^{ABC} t^C, \tag{2.4}$$

and f^{ABC} are the structure constants of the group $SU(3)$. The covariant derivative $\not{D}$ is required to transform covariantly under the same transformations:

$$D_\alpha q(x) \to (\partial_\alpha + igt\, \mathcal{A}'_\alpha)\, \Omega(x)\, q(x) \equiv \Omega(x)\, D_\alpha\, q(x). \tag{2.5}$$

This transformation property is given if and only if the gauge field $\mathcal{A}_\alpha$ transforms in the following way:

$$t \cdot \mathcal{A}'_\alpha = \Omega(x)\, t \cdot \mathcal{A}_\alpha\, \Omega^{-1}(x) + \frac{i}{g} (\partial_\alpha\, \Omega(x))\, \Omega^{-1}(x). \tag{2.6}$$

The field strength tensor $F^A_{\alpha\beta}$ in equation 2.2 derives from the gluon field $\mathcal{A}^A_\alpha$,

$$F^A_{\alpha\beta} = [\partial_\alpha \mathcal{A}^A_\beta - \partial_\beta \mathcal{A}^A_\alpha - g f^{ABC} \mathcal{A}^B_\alpha \mathcal{A}^C_\beta], \tag{2.7}$$

and contains a non-Abelian term giving rise to gluon self-interactions and the property of asymptotic freedom [5–8]. Under local $SU(3)$ transformation the field strength tensor transforms in the following way:

$$t \cdot F_{\alpha\beta}(x) \to \Omega(x)\, t \cdot F_{\alpha\beta}(x)\, \Omega^{-1}(x). \tag{2.8}$$

To understand the confinement of quarks and gluons inside hadrons one can consider a dimensionless physical observable R that depends on a single energy scale

Q. Assuming that this scale is larger than the other dimensionful parameters, one would naively expect that R assumes a constant value that is independent of Q. However, if one calculates an observable in perturbative quantum field theory, the perturbative series will require the procedure of renormalisation in order to remove ultraviolet divergences. This introduces another scale μ, which defines at which point the ultraviolet divergencies are cut off, such that the observable R will generally depend on the ratio Q^2/μ^2 and not be constant [8].
Provided that the renormalisation scale does not appear in the classical Lagrangian, physical quantities cannot explicitly depend on the choice of scale. The scale μ is rather introduced during the procedure of quantisation, and the dimensionless observable R can only depend upon the ratio Q^2/μ^2 and the coupling constant α_s. This means that the observable R has to fulfill the following equation:

$$\Big[-\frac{\partial}{\partial t} + \beta(\alpha_s)\frac{\partial}{\partial \alpha_s}\Big] R(e^t, \alpha_s) = 0, \tag{2.9}$$

where t and $\beta(\alpha_s)$ are defined as

$$t = \ln\left(\frac{Q^2}{\mu^2}\right), \quad \beta = \mu^2 \frac{\partial \alpha_s}{\partial \mu^2}, \tag{2.10}$$

and the derivative in the definition of the β function is performed at fixed bare coupling [8]. This partial differential equation can be solved by the implicit definition of the running coupling constant $\alpha_s(Q^2)$:

$$t = \int_{\alpha_s}^{\alpha_s(Q^2)} \frac{dx}{\beta(x)}, \quad \alpha_s(\mu^2) \equiv \alpha_s. \tag{2.11}$$

Differentiation with respect to t and $\alpha_s(Q^2)$ gives the relations:

$$\beta(\alpha_s(Q^2)) = \frac{\partial \alpha_s(Q^2)}{\partial t}, \quad \frac{\beta(\alpha_s(Q^2))}{\beta(\alpha_s)} = \frac{\partial \alpha_s(Q^2)}{\partial \alpha_s}. \tag{2.12}$$

Now, one can use the relations defined in equation 2.12 to resolve equation 2.9 and find the solution $R(1, \alpha_s(Q^2))$, which shows that the scale dependence in R enters through the running of the coupling constant $\alpha_s(Q^2)$ [8]. This means that the function $R(1, \alpha_s(Q^2))$, calculated in fixed-order perturbation theory, predicts the variation of the physical observable R with respect to Q^2 as long as equation 2.11 has a solution. In general the running coupling constant is defined by the renormalisation group equation:

$$Q^2 \frac{\partial \alpha_s}{\partial Q^2} = \beta(\alpha_s). \tag{2.13}$$

The β function can be expanded in perturbative QCD allowing equation 2.13 to be written in the following notation:

$$Q^2 \frac{\partial \alpha_s^2(Q^2)}{\partial Q^2} = -b\,\alpha_s^2(Q^2)\Big[1 + b'\alpha_s(Q^2) + O(\alpha_s^2(Q^2))\Big], \tag{2.14}$$

where b and b' are coefficients of the perturbative expansion [8]. Provided that $\alpha_s(Q^2)$ and $\alpha_s(\mu^2)$ are in the perturbative regime one may simplify the right-hand side and solve the resulting differential equation for $\alpha_s(Q^2)$. Neglecting coefficients of second and higher order gives the solution:

$$\alpha_s(Q^2) = \frac{\alpha_s(\mu^2)}{1 + \alpha_s(\mu^2)\, b\, t}, \quad t = \ln\frac{Q^2}{\mu^2}. \tag{2.15}$$

Equation 2.15 defines the relation between $\alpha_s(Q^2)$ and $\alpha_s(\mu^2)$ for the scenario where both are in the perturbative regime, and proves that the running coupling constant $\alpha_s(Q^2)$ decreases to zero as the variable t approximates large values. This property is known as asymptotic freedom and guarantees that we can always solve equation 2.11 [8] in perturbation theory for sufficiently large Q^2.

2.2 Deep Inelastic Scattering (DIS)

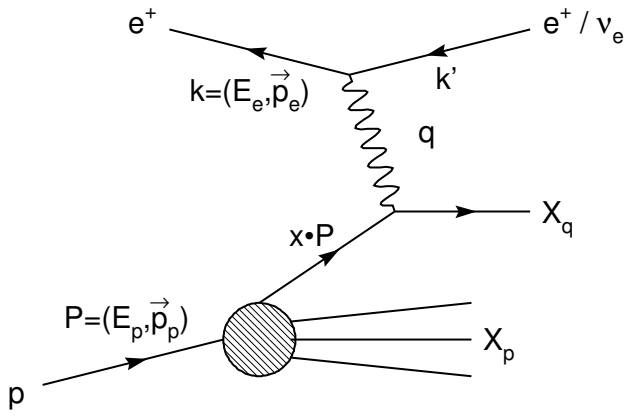

Figure 2.1: Feynman diagram of deep inelastic scattering (DIS).

Neutral current deep inelastic scattering (DIS) [2] between an electron[1] and a proton occurs when the incoming electron emits an off-shell boson (i.e. γ or Z^0) that interacts with the constituents of the proton causing it to break up. Figure 2.1 shows the Feynman diagram of DIS. In this scheme k and $k^{'}$ refer to the four-momentum of the incoming and outgoing lepton respectively, and p denotes the four-momentum of the incoming proton. The four-momentum q of the exchanged vector boson is then given as the difference between the four-momentum of the scattered and the incoming lepton:

$$q = k - k^{'} \tag{2.16}$$

[1]In the following, the term electron will be used for electrons and positrons unless stated otherwise.

In DIS the physical process can be completely described in terms of four Lorentz scalars [42, 43], see figure 2.1:

$$Q^2 = -q^2 = (k - k')^2, \tag{2.17}$$

$$s = (k + P)^2 \simeq 2k \cdot P, \tag{2.18}$$

$$y = \frac{P \cdot q}{P \cdot k} \simeq \frac{2P \cdot q}{s}, \tag{2.19}$$

$$x = \frac{Q^2}{2P \cdot q}, \tag{2.20}$$

where s denotes the square of the centre-of-mass energy, the Bjorken variable x represents the fraction of the proton momentum carried by the struck parton, and the Bjorken variable y denotes the inelasticity of the event. The variables are related through the following equation:

$$Q^2 = sxy. \tag{2.21}$$

The scattering process provides information about the internal proton structure, since the virtual boson interacts with the proton constituents on the most fundamental level. In deep inelastic scattering the photon virtuality Q^2 can be seen as a measure of the resolving power of the event, with higher momentum transfers achieving to resolve the proton structure at a more fundamental level.
In DIS the parton model of the proton can be most easily formulated in the infinite momentum frame where $p^\mu \approx (P, 0, 0, P)$ and $P \gg M_P$. In this frame the photon scatters off a point like parton that is moving parallel with the proton carrying a fraction ξ of its momentum, i.e. $p_q^\mu = \xi p^\mu$. The differential cross section for the lepton-hadron scattering can then be defined in terms of structure functions $F_i(x, Q^2)$ which parametrise the structure of the target as "seen" by the virtual boson [44]:

$$\frac{d^2\sigma}{dx\, dQ^2} = \frac{4\pi\alpha^2}{Q^4}\Big[[1 + (1 - y)^2]F_1 + \frac{(1 - y)}{x}(F_2 - 2xF_1)\Big]. \tag{2.22}$$

The spin-averaged matrix element for the process $e^- q \to e^- q$ can be calculated from first principles in perturbative quantum field theory and provides the following expression for the differential cross section:

$$\frac{d^2\hat{\sigma}}{dx\, dQ^2} = \frac{4\pi\alpha^2}{Q^4}[1 + (1 - y)^2]\,\frac{1}{2}\,e_q^2\,\delta(x - \xi), \tag{2.23}$$

which suggests that $F_2(x)$ probes a parton with momentum fraction $\xi = x$. However, one assumes that the structure function $F_2(x)$ is rather a distribution in x, which suggests that the quarks carry a range of momentum fractions. The naive parton model accounts for these ideas by assuming that the virtual photon scatters incoherently off the constituents of the proton and $q(\xi)\, d\xi$ represents the

probability that a quark q carries momentum fraction between ξ and $\xi+d\xi$, where $0 \leq \xi \leq 1$. The proton structure functions are therefore obtained by weighting the quark structure functions with the probability density $q(\xi)$:

$$F_2(x) = 2x\,F_1(x) = \sum_{q,\bar{q}} e_q^2\, x\, q(x), \tag{2.24}$$

where the relation between $F_1(x)$ and $F_2(x)$ (Callan-Gross) is a direct consequence of the spin-$\frac{1}{2}$ property of the quarks.
In the naive parton model the structure functions $F_i(x)$ scale in the asymptotic limit $Q^2 \to \infty$ at fixed x [43, 45]. In reality this scaling is broken in QCD [46], since the partons can emit a gluon with a probability proportional to dk_T^2/k_T^2 acquiring transverse momentum. The integral extends up to large values of $k_T^2 \sim Q^2$ giving rise to contributions proportional to $\alpha_s \log Q^2$ which break the scaling. The structure function in the quark parton model corrected to the order $O(\alpha_s)$ is given by:

$$\hat{F}_2(x,Q^2) = e_q^2 x\Big[\delta(1-x) + \frac{\alpha_s}{2\pi}\Big(P(x)\ln\left(\frac{Q^2}{\kappa^2}\right) + C(x)\Big)\Big], \tag{2.25}$$

where $P(x)$ is the splitting function of the qqg vertex, $C(x)$ is a calculable function and κ is a small cut-off parameter. The corresponding quark distribution is given by:

$$q(x,Q^2) = \delta(1-x) + \frac{\alpha_s}{2\pi}\left(P(x)\ln\left(\frac{Q^2}{\kappa^2}\right) + C(x)\right). \tag{2.26}$$

This means that the structure function is Q^2 dependent beyond leading order and Bjorken scaling is broken. Furthermore, singularities arise when the gluon is emitted parallel to the quark axis ($k_T = 0$), which is the reason why these singularities are called collinear divergences. However, the limit $k_T \to 0$ corresponds to a long range, soft part of the strong interaction that is not calculable in perturbative theory. In order to obtain a proton structure function one has to convolute the structure function $\hat{F}_2$ with a bare distribution q_0 of quarks and sum over the quark flavours in the proton. This gives the result:

$$F_2(x,Q^2) = x\sum_{q\bar{q}} e_q^2\left[q_0(x) + \frac{\alpha_s}{2\pi}\int_x^1 \frac{d\xi}{\xi} q_0(\xi)\Big\{P\left(\frac{x}{\xi}\right)\ln\frac{Q^2}{\kappa^2} + C\left(\frac{x}{\xi}\right)\Big\} + ...\right]. \tag{2.27}$$

The quantity $q_0(x)$ is regarded as an unmeasurable, bare distribution, and the collinear singularities are absorbed into this bare distribution at a factorisation scale μ_F which plays a similar role to the renormalisation scale. This means one defines a renormalised distribution $q(x,Q^2)$

$$q(x,\mu^2) = q_0(x) + \frac{\alpha_s}{2\pi}\int_x^1 \frac{d\xi}{\xi} q_0(\xi)\Big\{P\left(\frac{x}{\xi}\right)\ln\left(\frac{\mu^2}{\kappa^2}\right) + C\left(\frac{x}{\xi}\right)\Big\} + ... \tag{2.28}$$

that leads to the structure function $F_2(x, Q^2)$ in terms of the renormalised parton distribution:

$$F_2(x,Q^2) = x\sum_{q\bar{q}} e_q^2 \int_x^1 \frac{d\xi}{\xi} q(\xi,\mu^2) \times \left\{ \delta\left(1-\frac{x}{\xi}\right) + \frac{\alpha_s}{2\pi} P\left(\frac{x}{\xi}\right) \ln\left(\frac{Q^2}{\mu^2}\right) + ... \right\}. \tag{2.29}$$

The distribution $q(x, Q^2)$ cannot be calculated from first principles as it receives contributions from the non-perturbative part of the strong interaction. Instead the parton density $q(x, Q^2)$ needs to be extracted from measurements of the structure function $F_2(x, Q^2) = x\sum e_q^2 q(x, Q^2)$ at a particular scale. The ability to separate long- and short-distance contributions to the structure function is known as factorisation and constitutes a fundamental property of the theory. The factorisation theorem states that the cross section for DIS may be written as the convolution of the non-perturbative parton density and the Wilson coefficients which are calculable from first principles in perturbative QCD:

$$F_i(x,Q^2) = q_a(x) \otimes \hat{\sigma_i^a} = \int_x^1 \frac{d\xi}{\xi} q_a\left(\xi,\mu^2\right) \sigma_i^a\left(\frac{x}{\xi}, Q^2, \mu^2\right), \tag{2.30}$$

where $q(\xi, \mu^2)$ is the parton density function, and $\hat{\sigma}_i^a$ is the cross section for $\gamma^\star q$ scattering. In order to obtain the evolution equation of the parton densities with the scale Q^2, one defines $t = \mu^2$ and takes the partial derivative of equation 2.28:

$$t\frac{\partial}{\partial t} q(x,t) = \frac{\alpha_s(t)}{2\pi} \int_x^1 \frac{d\xi}{\xi} P\left(\frac{x}{\xi}\right) q(\xi,t). \tag{2.31}$$

Equation 2.31 is known as the DGLAP equation [18] and can be derived more rigorously using the operator product expansion and renormalisation group equation [14, 15]. The result of this expansion is given by

$$t\frac{\partial}{\partial t} q(x,t) = \frac{\alpha_s}{2\pi} \int_x^1 \frac{d\xi}{\xi} P_{qq}\left(\frac{x}{\xi}, \alpha_s\right) q(\xi,t), \tag{2.32}$$

where the splitting function P_{qq} has a perturbative expansion in running coupling constant, α_s, given by

$$P_{qq}(z,\alpha_s) = P_{qq}^{(0)} + \frac{\alpha_s}{2\pi} P_{qq}^{(1)}(z) + ... \tag{2.33}$$

Applying the perturbative expansion of the splitting functions to first order to equation 2.32 retrieves equation 2.31. Strictly speaking equation 2.31 is only applicable for non-singlet distributions. More generally the DGLAP evolution equation is a $(2n_f{+}1)$-dimensional matrix equation in the space of quarks, anti-quarks and gluons:

$$t\frac{1}{\partial t}\begin{pmatrix} q_i(x,t) \\ g_i(x,t) \end{pmatrix} = \frac{\alpha_s}{2\pi} \sum_{q_i,\bar{q}_j} \int_x^1 \frac{d\xi}{\xi} \tag{2.34}$$

$$\times \begin{pmatrix} P_{q_iq_j}(\frac{x}{\xi},\alpha_s(t)) & P_{q_ig}(\frac{x}{\xi},\alpha_s(t)) \\ P_{gq_j}(\frac{x}{\xi},\alpha_s(t)) & P_{gg}(\frac{x}{\xi},\alpha_s(t)) \end{pmatrix} \begin{pmatrix} q_j(\xi,t) \\ q(\xi,t) \end{pmatrix}, \tag{2.35}$$

where each splitting function is calculable as a power series in α_s,

$$P_{q_i q_j}(z, \alpha_s) = \delta_{ij} P_{qq}^{(0)}(z) + \frac{\alpha_s}{2\pi} P_{q_i q_j}^{(1)}(z) + ... \tag{2.36}$$

$$P_{qg}(z, \alpha_s) = P_{qg}^{(0)}(z) + \frac{\alpha_s}{2\pi} P_{qg}^{(1)}(z) + ... \tag{2.37}$$

$$P_{gq}(z, \alpha_s) = P_{gq}^{(0)}(z) + \frac{\alpha_s}{2\pi} P_{gq}^{(1)}(z) + ... \tag{2.38}$$

$$P_{gg}(z, \alpha_s) = P_{gg}^{(0)}(z) + \frac{\alpha_s}{2\pi} P_{gg}^{(1)}(z) + ... \tag{2.39}$$

$$\tag{2.40}$$

At leading order the splitting functions $P_{p_i,p_j}^{(0)}(z)$ can be interpreted as the probability of finding a parton p_i in parton p_j with a fraction z of the longitudinal momentum of its parent.

2.3 Heavy Flavour Production at HERA

This section will give an overview over the different schemes that allow heavy quarks to be incorporated in the framework of perturbative QCD. The fixed-flavour number scheme [24–27], the zero-mass variable flavour number scheme [23] and the variable flavour number scheme [28–40] will be presented in subsection 2.3.1. Subsection 2.3.2 illustrates the problems that arise upon the inclusion of heavy quark masses within the different schemes in perturbative QCD, while subsection 2.3.3 reviews recent results from HERA.

2.3.1 Heavy Flavour Schemes

At Q^2 and x values accessible at HERA, heavy quarks constitute up to 30 % of the structure function F_2 of the proton. However, the inclusion of massive quarks requires an extension of the DGLAP formalism to treat heavy flavour production and the running coupling constant α_s consistently at the heavy quark mass threshold and for large momentum transfer. The most common approaches to incorporate heavy flavours into the DGLAP formalism are given by the fixed-flavour number scheme (FFNS) [24–27], the zero-mass variable flavour number scheme (ZM-VFNS) [23] and the variable flavour number scheme (VFNS) [28–40].

In the FFNS [24–27] the intrinsic charm quark density is neglected, and the charmed quarks are generated by the mechanism of boson-gluon fusion (BGF), illustrated in figure 2.2. The advantage of the FFNS scheme is that the heavy quark mass threshold is handled correctly in the perturbative calculations of differential cross sections. In this approach large $\ln(Q^2/m_c^2)$ terms appear in the structure function F_2, which have to be treated separately for each hard scattering process.

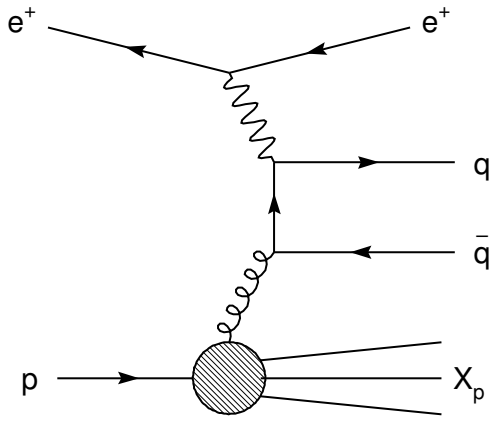

Figure 2.2: Feynman diagram of boson - gluon fusion.

In the ZM-VFNS [23] one defines the total number of quarks inside the proton as $n_f = 3 + \theta(Q^2 - \mu_c^2)$. The charm quark density satisfies $c(x, Q^2) = 0$ for $Q^2 \leq \mu_c^2$, and the threshold μ_c is chosen in the range $m_c^2 < \mu_c^2 < 4m_c^2$ such that $F_2^c(x, Q^2) = 2e_c^2 x\, c(x, Q^2)$ gives a satisfactory description of the data. For the transition, α_s is matched using a well-defined prescription that will be explained in the following section. In this approach the simplicity of the DGLAP equations is maintained, but the threshold of heavy flavour production is not treated correctly.
In the VFNS [28–40] the heavy quark contribution to the structure function F_2 of the proton is calculated by interpolation between the FFNS scheme at low Q^2 and the ZM-VFNS scheme at large Q^2. The combination of the different schemes yields the correct properties of the FFNS at the threshold and a charm quark density at large Q^2.

2.3.2 Implementation in QCD

The problems that arise due to the inclusion of heavy flavours in the DGLAP framework can be illustrated by studying the full expression for $F_2^{c\bar{c}}$ in the fixed-flavour number scheme [24–27] at order α_s:

$$F_2^{c\bar{c}} = 2\int_x^1 \frac{dz}{z} x g_3(x/z, \mu^2) C_g^{FF}(z, m_c^2/Q^2, \mu^2), \tag{2.41}$$

where $g_3(x/z, \mu^2)$ is the gluon density for three light quark flavours. For the choice of scale $\mu = \sqrt{Q^2 + 4m_c^2}$ one can expand the massive fixed flavour coefficient function:

$$C_g^{FF}(z, m_c^2/Q^2, \mu^2) = \frac{\alpha_s(\mu^2)}{2\pi} e_c^2 C_g^{1,FF}(z, m_c^2/Q^2) + ... \tag{2.42}$$

with

$$C_g^{1,FF}(z,m_c^2/Q^2) = \frac{1}{2}\Bigg\{\left[z^2+(1-z)^2+\frac{4m_c^2}{Q^2}z(1-3z)-8z^2\left(\frac{m_c^2}{Q^2}\right)^2\right]\ln\left(\frac{1+\beta}{1-\beta}\right) + \left[8z(1-z)-1-\frac{4m_c^2}{Q^2}z(1-z)\right]\beta\Bigg\}\theta(\hat{W}-4m_c^2), \tag{2.43}$$

where β is the velocity of the charm quark, and the θ function guarantees the correct threshold behaviour. For $Q^2 \gg m_c^2$ one obtains the expression:

$$C_g^{1,FF}(z,m_c^2/Q^2) \to \frac{1}{2}\Bigg\{\left[z^2+(1-z)^2\right]\ln\left(\frac{1-z}{z}\right) + 8z(1-z)-1+\left[z^2+(1-z)^2\ln\left(\frac{Q^2}{m_c^2}\right)\right]\Bigg\}. \tag{2.44}$$

The first two terms in this expression form the gluon coefficient functions C_g^1 of the massless DGLAP formalism. The third term appears for the first time in the massive fixed flavour number scheme and gives a non-zero contribution for heavy quark production. The problems arising from logarithmic terms have already been resolved in the zero-mass variable flavour number scheme [23]. In the DGLAP formalism for massless quarks the large infrared logs have been absorbed by the renormalisation of the parton densities at the factorisation scale μ_F and the large Q^2 logs have been resummed in the formalism introduced by the renormalisation group equation. However, in the massive fixed flavour number scheme the coefficient functions for boson-gluon fusion are not available for a resummation to all orders, such that the massive scheme is expected to describe heavy flavour production at threshold, but is not applicable otherwise.
In order to obtain a scheme that interpolates between the ZM-VFNS and the FFNS certain conditions must be fulfilled. First of all, one assumes that the heavy quark contribution $F_2^{c\bar{c}}$ to the proton structure function can be written in the following way:

$$F_2^{c\bar{c}} = 2e_c^2\int_x^1 dz\frac{x}{z}\left[c(x/z,\mu^2)\,C_q^{VF}(z,Q^2/\mu^2)+g_4(x/z,\mu^2)\,C_g^{VF}(z,Q^2/\mu^2)\right], \tag{2.45}$$

where $c(x/z,\mu^2)$ is the charm quark and g^4 is the gluon density for four flavours and the coefficient functions can be expanded as a perturbative series in α_s:

$$C_q^{VF} = C_q^{0,VF} + \frac{\alpha_s}{2\pi}\,C_q^{1,VF} + ... \tag{2.46}$$

$$C_g^{VF} = \frac{\alpha_s}{2\pi}\,C_g^{VF} + ... \tag{2.47}$$

One requires that the parton densities and coefficient functions are identical to those defined in the FFNS for $Q^2 < m_c^2$, while they converge to the coefficient

functions in the massless DGLAP formalism in the limit $Q^2 \gg m_c^2$. At a scale in the vicinity of m_c^2 the expressions in the FFNS and VFNS are matched with elements of a 5×4 coefficients matrix that matches the three and four flavour parton densities. At first order in α_s these equations take the following form:

$$c(x, Q^2) = \frac{\alpha_s}{2\pi} \ln\left(\frac{Q^2}{m_c^2}\right) P_{qg}^{(0)} \otimes g_3(x, Q^2), \tag{2.48}$$

$$g_4(x, Q^2) = \left(1 - \frac{\alpha_s}{6\pi} \ln\left(\frac{Q^2}{m_c^2}\right)\right) g_3(x, Q^2), \tag{2.49}$$

which allows the coefficient functions of the variable and fixed-flavour number scheme to be matched:

$$C_g^{1,FF}(z, Q^2/m_c^2) = C_g^{1,VF}(z, Q^2/m_c^2) + C_q^{0,VF}(z, Q^2/m_c^2) \otimes P_{qg}^{(0)} \ln\left(\frac{Q^2}{m_c^2}\right). \tag{2.50}$$

Additionally, α_s needs to be matched for three and four massless flavours. In perturbative QCD, equation 2.50 gives the definition of $C_g^{1,VF}$, provided that the coefficient functions, $C_q^{0,VF}$, can be calculated at first order. Various suggestions to satisfy the conditions formulated in equation 2.50 have been made. Roberts and Thorne [34, 35] have proposed to remove some of the arbitrariness in the choice of $C_q^{0,VF}$ by requiring that the derivative $dF_2^{c\bar{c}}/d\ln Q^2$ also matches smoothly for the three and four flavour number scheme. Matching the right-hand and the left-hand side at m_c^2 simplifies the conditions such that one obtains the following simplified expression:

$$C_q^{0,VF}(Q^2/m_c^2) \otimes P_{qg}^{(0)} = \frac{\partial C_g^{1,FF}(z, Q^2/m_c^2)}{\partial \ln Q^2}. \tag{2.51}$$

The right-hand side of this equation can be found by direct differentiation, such that equation 2.50 becomes:

$$C_g^{1,VF}(z, Q^2/m_c^2) = C_g^{1,FF}(z, Q^2/m_c^2) - \frac{\partial C_g^{1,FF}(z, Q^2/m_c^2)}{\partial \ln Q^2} \ln\left(\frac{Q^2}{m_c^2}\right). \tag{2.52}$$

This equation resolves the problem of interpolation between the zero-mass variable flavour number scheme and the fixed flavour number scheme. One can observe that $C_g^{1,VF}$ has the same threshold behaviour as $C_g^{1,FF}$, and the second term in equation 2.52 removes the $P_{qg}^{(0)} \ln(Q^2/m_c^2)$ term leaving the coefficient function $C_g^{1,ZMVF}$ in the zero-mass variable flavour number scheme at large Q^2. The general solution of equation 2.52 requires the convolution $C^{0,VF} \otimes c(x, Q^2)$ and produces a smooth interpolation between the FFNS near threshold and the ZM-VFNS at large Q^2.

2.3.3 Results from HERA

At HERA different techniques have been used to measure charm production cross sections in DIS. The full reconstruction of D or D^* meson [47–56], the lifetime information [57–60] or the semileptonic decays [61] of heavy flavoured hadrons have been used to extract the charm content of the data sample. Among these techniques, the best signal-to-background ratio is obtained in the analyses of fully reconstructed D^* mesons, although the precision of the technique is limited. The branching ratios are small, and the phase space of charm production accessible with D^* meson decays is restricted, because all decay products need to be reconstructed.

The analysis of semileptonic decays benefits from larger branching fractions and a better coverage in the polar angle, whilst suffering from a worse signal-to-background ratio. The measurement exploits information from three distinguishing variables sensitive to different aspects of heavy quark decays: the muon impact parameter, the muon momentum component transverse to the associated jet axis, and the missing transverse momentum sensitive to the neutrino from semileptonic decays. The fractions of beauty, charm and light flavour events are extracted by fitting a combination of MC distributions to the measured three-dimensional distribution of the discriminating variables.

In contrast to analyses using the full reconstruction of charmed mesons or semileptonic decays of heavy flavoured hadrons, fully inclusive analyses based on lifetime information are not limited by branching fractions. At ZEUS inclusive measurements are usually based on the decay length significance and the secondary vertex mass to distinguish heavy flavoured decays from the light flavoured background. The H1 collaboration, on the other hand, exploits the impact parameter significance of reconstructed tracks and a combination of various variables that are fed into a neural network. The fractions of charm, beauty and light flavour events is determined by a binned, least χ^2 fit of a combination of MC templates to the considered distinguishing variables in the data sample. Inclusive measurements are sensitive to low transverse momenta, and provide the largest phase space coverage, although they suffer from a worse signal-to-background ratio than other analyses.

In a recent publication [62] all data sets of the H1 and ZEUS collaborations, for which the necessary information on the systematic uncertainties needed for the combination were available, have been combined. The combination of the different data sets is based on the χ^2 minimisation method developed for the combination of inclusive DIS cross sections described in [63–65]. In order to perform the combination the published cross sections in the restricted phase space regions of the individual measurements have been extrapolated to the full phase space in a coherent manner by the use of fixed-flavour-number calculations in next-to-leading order in perturbative QCD. A consistent data set was obtained by accounting for correlated systematic uncertainties and the normalisation of

the different measurements.
The results of the combination of charm production cross sections in neutral-current deep inelastic scattering are presented in terms of reduced cross sections, $\sigma_{red}^{c\bar{c}}$, defined in the following way:

$$\sigma_{red}^{c\bar{c}} = \frac{d^2\sigma^{c\bar{c}}}{dxdQ^2} \cdot \frac{xQ^4}{2\pi\alpha^2(Q^2)(1+(1-y)^2)} \tag{2.53}$$

$$= F_2^{c\bar{c}} - \frac{y^2}{1+(1-y)^2} F_L^{c\bar{c}}. \tag{2.54}$$

The longitudinal structure function, $F_L^{c\bar{c}}$, originates from the exchange of longitudinally polarised photons. In general, the influence of the $F_L^{c\bar{c}}$ term is small in the kinematic range of the measurement, and reaches up to a few per cent at high values of Bjorken y.
The combination led to a significant reduction of statistical and systematic uncertainties, as different methods of reconstruction, different detectors and experimental techniques have been employed in the individual measurements. The uncertainty in the combined results is 10 % on average and reaches 6 % in the region of small x and medium Q^2. This represents an improvement of the total relative error of 50 % with respect to the most precise data sets in the combination. Figure 2.3 shows a comparison of the results of the combination with predictions of the ABM group [66–68] at NLO and NNLO in the fixed-flavour-number scheme using the $\overline{\text{MS}}$ definition of the charm quark mass. After the combination of the different data sets the reduced charm production cross sections are in good agreement with the theoretical predictions in the whole kinematic region. This is particularly remarkable in the low Q^2 region, which is sensitive to the heavy quark mass threshold.
The combined charm data were subsequently used together with the combined inclusive DIS cross sections to perform a QCD analysis based on different schemes of heavy flavour production in DIS. In all schemes, the onset of the heavy quark PDFs is controlled by the heavy quark mass parameter, M_c, in addition to the kinematic constraints. The role of the parameter M_c in the fixed- and variable-flavour-number schemes was studied, and the optimal value was evaluated for each of the QCD calculations that were considered. In figure 2.4, the χ^2-values as a function of the charm quark mass parameter, M_c, obtained from PDF fits to the inclusive HERA-I data and the combined charm data are shown for the schemes that were considered. The minimal χ^2 values that were observed for the different schemes are similar, although they are realised at different values of the heavy quark mass parameter M_c.
In figure 2.5, NLO QCD predictions for the reduced cross sections, $\sigma_{red}^{c\bar{c}}$, in different versions of the variable-flavour-number scheme based on the PDFs evaluated using the optimal charm quark mass parameter $M_c = M_c^{opt}$ of the corresponding scheme are compared to the data. The differences in the description originate predominantly from different matching schemes of the massive and massless parts of

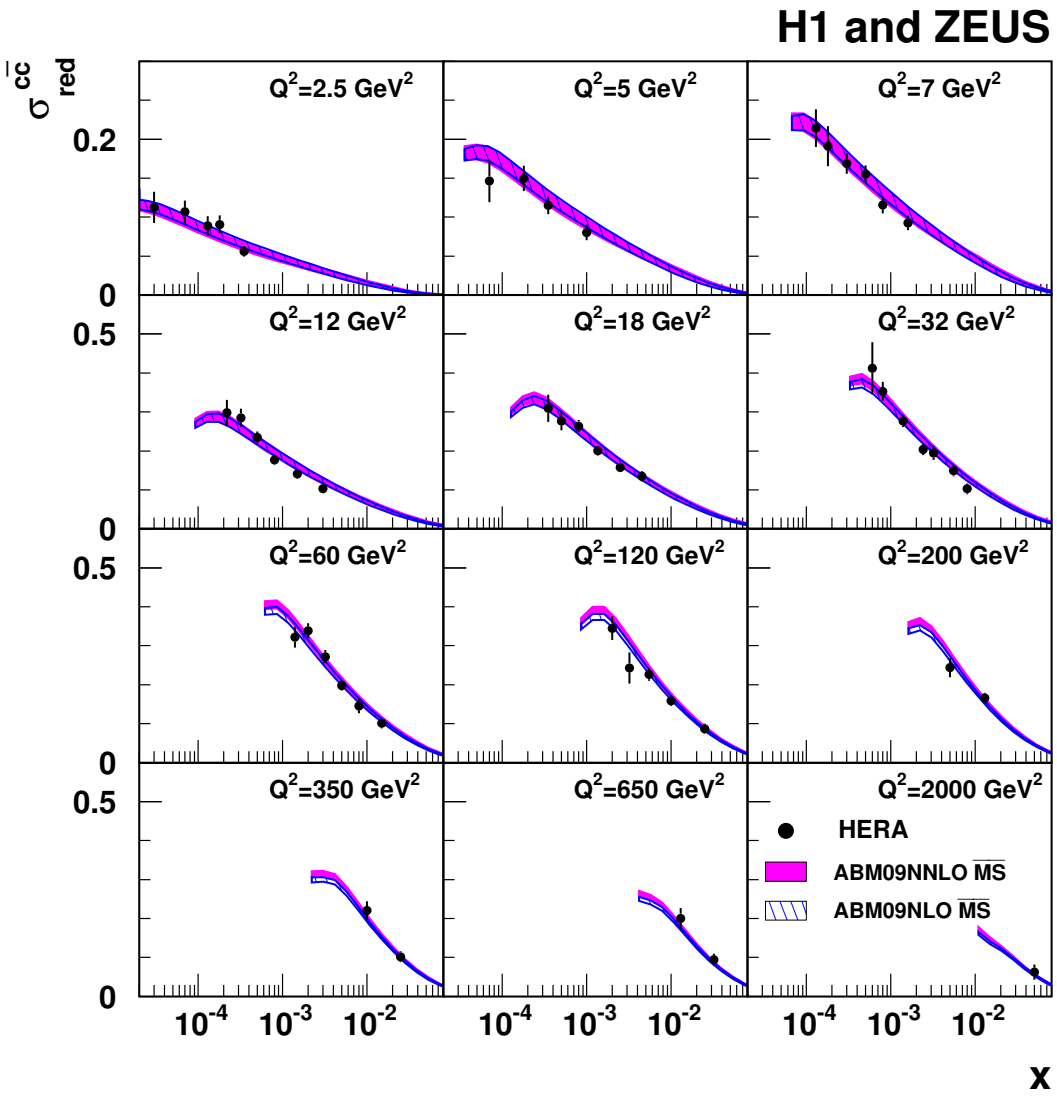

Figure 2.3: Combined reduced charm cross section $\sigma_{red}^{c\bar{c}}$ as a function of x for fixed values of Q^2 [62]. The error bars represent the total uncertainty including uncorrelated, correlated and procedural uncertainties added in quadrature. The data are compared to predictions of the ABM group at NLO (hatched band) and NNLO (shaded band) in the fixed-flavour-number scheme using the $\overline{\text{MS}}$ definition for the charm quark mass.

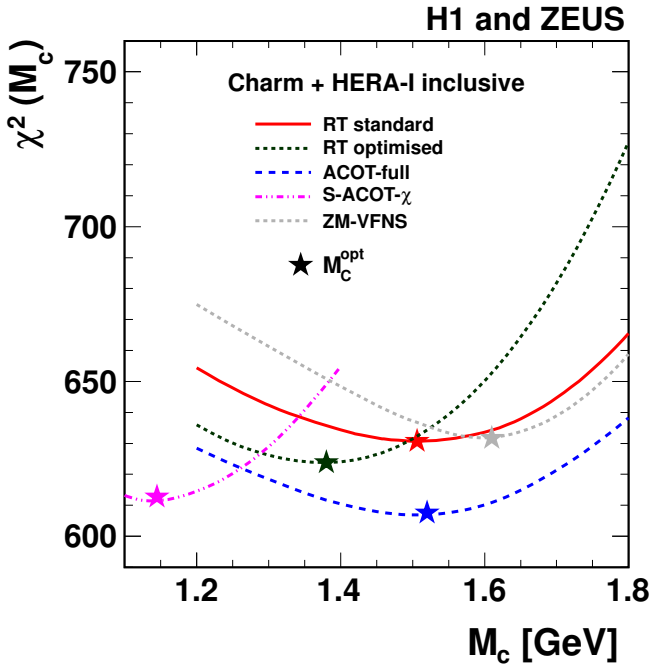

Figure 2.4: The values of χ^2 for the PDF fit of the combined HERA inclusive DIS and charm measurements [62]. Different heavy flavour schemes are used in the fit and presented by lines with different styles. The value of M_c^{opt} for each scheme is indicated by the stars.

the corresponding variable-flavour-number scheme. The data are generally better described than with the default values of M_c, although the predictions become similar in the kinematic region of $Q^2 \geq 5$ GeV^2.
Finally, the PDFs from a 13 parameter fit using the inclusive HERA-I data only were compared with the corresponding PDFs when the combined charm data was included [62]. The comparison of the PDF uncertainties shows that the uncertainty on the gluon distribution function has reduced due to the inclusion of the combined charm data, since the charm data constrains the parametrisation uncertainty through the process of boson-gluon fusion. Furthermore, the combined charm data constrains the valence quark distribution.
The different PDF sets obtained from fits of the HERA data in different variable-flavour-number schemes with the corresponding optimal charm mass parameter M_c^{opt} were then used to calculate cross sections predictions for $W^{\pm}$ and Z production cross sections at the LHC. The predicted $W^{\pm}$ and Z production cross sections as a function of the charm mass parameter M_c for the different versions of the variable-flavour-number scheme are shown in figure 2.6. The spread between the predictions of the different variable-flavour-number schemes considered for a fixed value of M_c is about 6 %, similar to the spread from the variation of the charm mass parameter in a given variable-flavour-number scheme alone. However, when using the optimal parameter M_c^{opt} for each scheme the spread of predictions is reduced to below 2 %. This demonstrates that the precise measurement of the charm contribution to the structure function of the proton constrains Standard Model predictions at the LHC, and therefore facilitates the searches for physics beyond the Standard Model.
Eventually, the constrained Standard Model predictions generated with the optimal charm mass parameter M_c^{opt} for each variable-flavour-number scheme have been confirmed by measurements of the ATLAS and CMS collaborations [69–73]. In the cited publications the results for the inclusive cross sections for $W^{\pm}/Z$ production have been multiplied with the branching fractions of the specific decay under investigation. This means that one needs to divide the measured cross sections by the respective branching ratios in order to obtain results that can be compared to the theoretical predictions presented in this thesis. E.g. for the electron decay mode one obtains:

$$W^+ : \ 6.16 \text{ nb} \,/\, 0.1075 \ = \ 57.30 \text{ nb}, \tag{2.55}$$

$$W^- : \ 4.30 \text{ nb} \,/\, 0.1075 \ = \ 40.00 \text{ nb}, \tag{2.56}$$

$$Z \ : \ 0.99 \text{ nb} \,/\, 0.03366 \ = \ 29.41 \text{ nb}. \tag{2.57}$$

This means that the values of the inclusive cross sections for $W^{\pm}/Z$ production measured with the ATLAS and CMS detectors are in perfect agreement with the theoretical predictions for the inclusive cross sections shown in figure 2.6, and hence confirm the Standard Model.

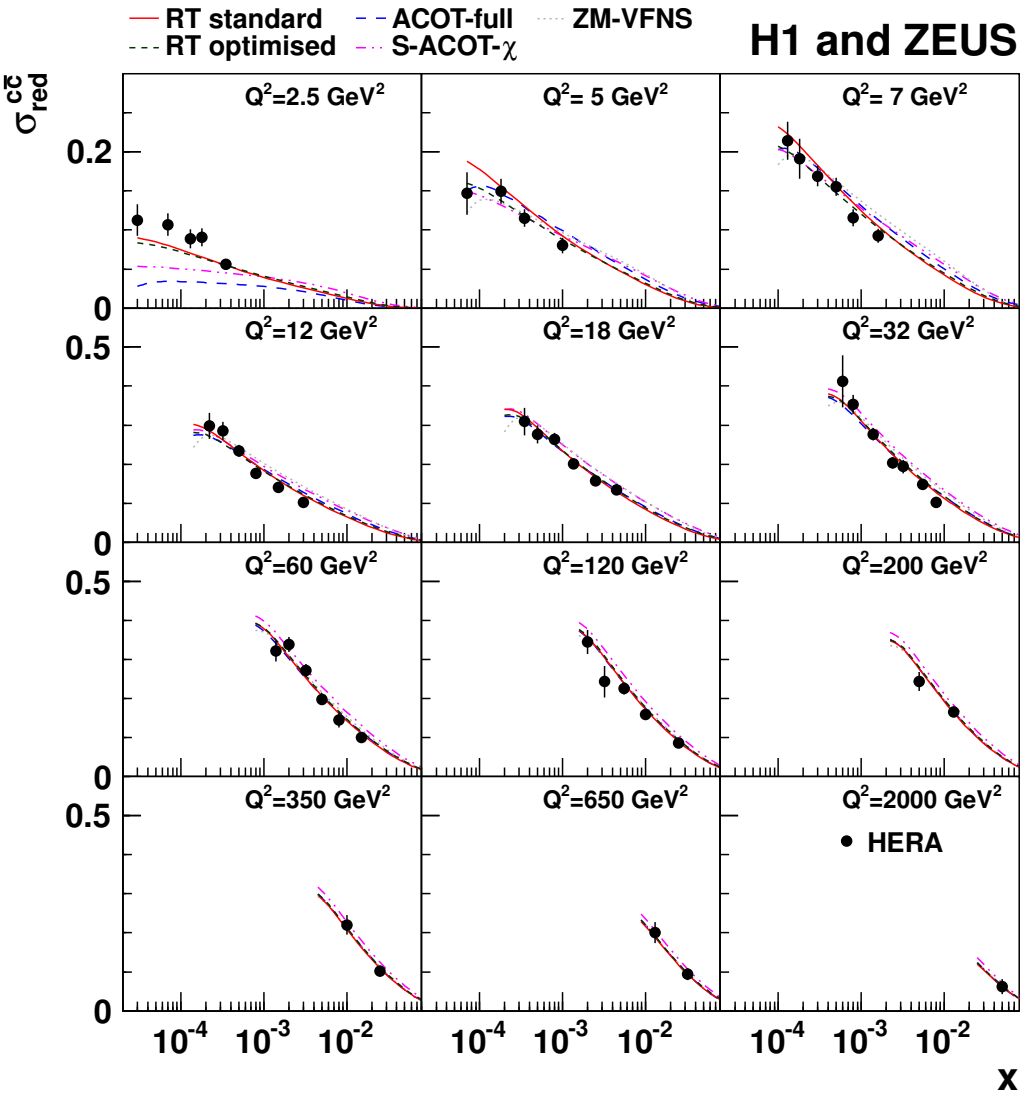

Figure 2.5: Combined reduced charm cross section $\sigma_{red}^{c\bar{c}}$ as a function of x for fixed values of Q^2. The error bars represent the total uncertainty including uncorrelated, correlated and procedural uncertainties added in quadrature. The data are compared to the results of the fit using different variants of the variable-flavour-number scheme (shown by lines of different style) choosing $M_c = M_c^{opt}$. The cross section prediction for the ZM-VFNS vanishes for $Q^2 = 2.5$ GeV^2.

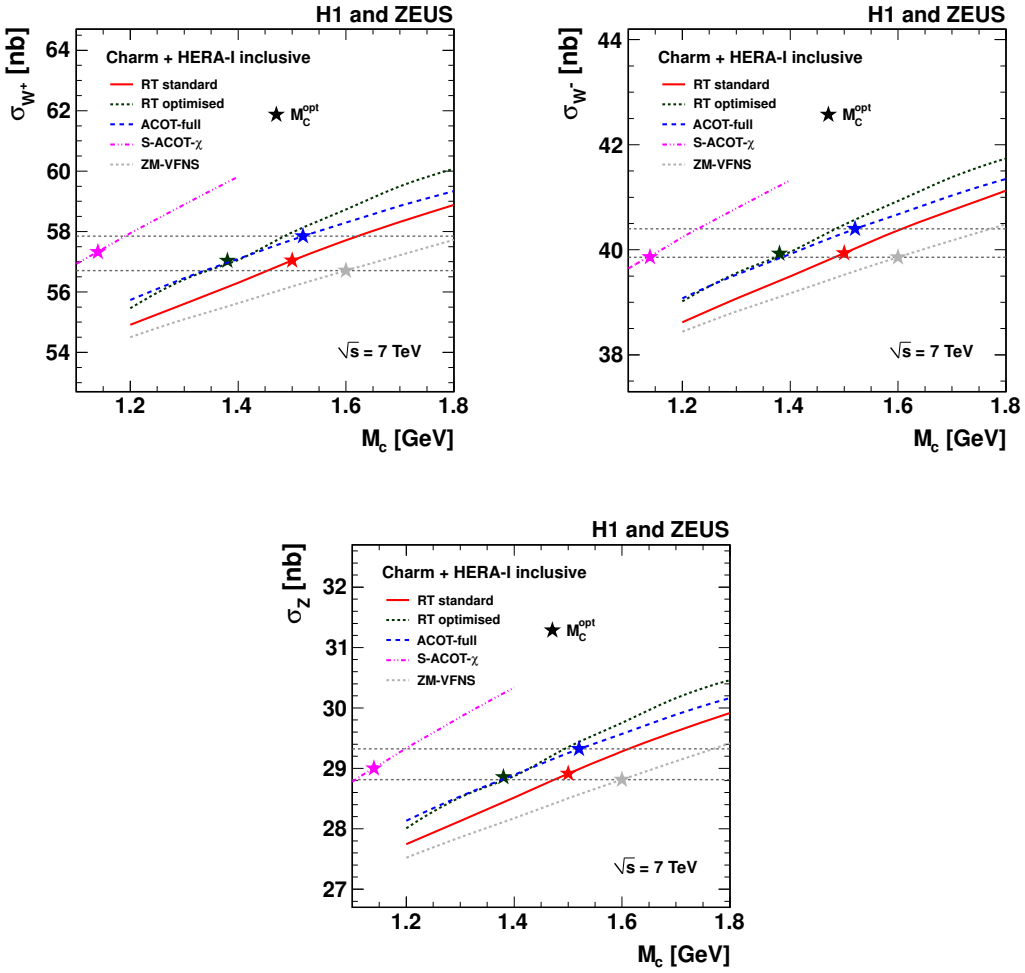

Figure 2.6: NLO predictions for (a) W^+, (b) W^- and (c) Z production cross sections at the LHC for $\sqrt{s} = 7$ TeV as a function of M_c used in the corresponding PDF fit. The different lines represent predictions for different implementations of the VFNS. The predictions obtained with PDFs evaluated with the M_c^{opt} values for each scheme are indicated by the stars. The horizontal dashed lines show the resulting spread of the predictions when choosing $M_c = M_c^{opt}$.

Chapter 3

Experimental Setup

In this chapter the experimental setup for the inclusive measurement of the charm contribution to the proton structure function will be explained. Section 3.1 will provide an introduction to the HERA accelerator [74], and explain the proton and electron acceleration chain. Section 3.2 will give an overview of the ZEUS detector [75] describing the detector components most relevant for this analysis. Of particular relevance for this analysis will be the reconstruction of secondary vertices with the microvertex detector (MVD) [76] and the straw tube tracker (STT) [77] that were installed during the upgrade 2000−2002. A detailed description will be given of the central tracking detector (CTD) [78–80], the uranium calorimeter (CAL) [81–84], the luminosity measurement [85–87], and the trigger and data acquisition systems [88].

3.1 The HERA Accelerator

The Hadron-Elektron Ring Anlage (HERA) [74] was located at the particle physics research centre Deutsches Elektronen Synchrotron (DESY) in Hamburg. At HERA electrons and protons were brought to collision at a centre-of-mass energy of $\sqrt{s} = 320$ GeV, and the physical products of these collisions were measured with the ZEUS detector, located in the south hall, and the H1 detector, located in the north hall. As the world's first, and to date only, electron−proton collider, HERA had a circumference of 6.3 km and was located 15−30 m beneath the Volkspark area. The accelerator operated between 1992 and 2007, and provided a facility for precision measurements of the proton structure and a unique testing ground for perturbative QCD.
The HERA accelerator consisted of two independent storage rings for electrons and protons, which were grouped in bunches of 10^{10} particles and brought to collision every 96 ns. However, the particles had to pass through several stages

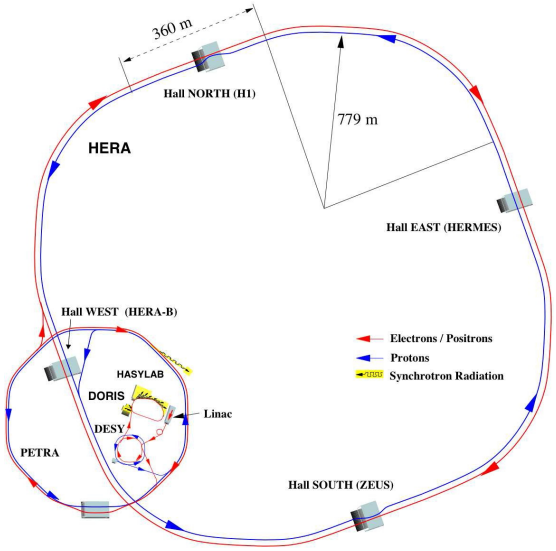

Figure 3.1: Schematic of HERA and pre-accelerators.

of pre-acceleration before being injected into HERA, where they were brought to their final energies. A schematic of HERA and its pre-accelerators is given in figure 3.1. The electrons were initially accelerated to 200 MeV in a linear pre-accelerator, before they were passed to the DESY II synchrotron, where they achieved an energy of 7.5 GeV. Subsequently they were transferred to PETRA, where they were accelerated to 14 GeV, before being injected into HERA to achieve their final energy of primarily 27.5 GeV.
The proton injection chain began with the acceleration of H^- ions to 50 MeV in the linear accelerator. The H^- ions were subsequently injected into the DESY III synchrotron to be accelerated to 7.5 GeV. The electrons were then stripped off, and the resulting protons transferred to PETRA II, where they were accelerated to 40 GeV. Finally, the protons were injected into HERA, where they were brought to their final beam energy of primarily 920 GeV. During the last three months of operation, data were taken at reduced beam energies of 460 and 575 GeV in order to facilitate the measurement of the longitudinal structure function, F_{L}.
At HERA, data-taking was divided into two different periods, HERA I from 1992 to 2000 and HERA II from 2002 to 2007. The purpose of the shutdown from 2000 to 2002 was to perform several machine and detector upgrades. The machine upgrades included the installation of additional components, in particular focusing magnets closer to the interaction point, which increased the integrated luminosity by a factor three [89]. The luminosity delivered by HERA is illustrated in figure 3.2. After the upgrade, the leptons were longitudinally polarised in both experiments. The polarisation was changed using spin rotators [90], which were placed at each side of the H1 and ZEUS experiments and rotated the transverse polarisation of the electron beam into longitudinal polarisation and back to transverse

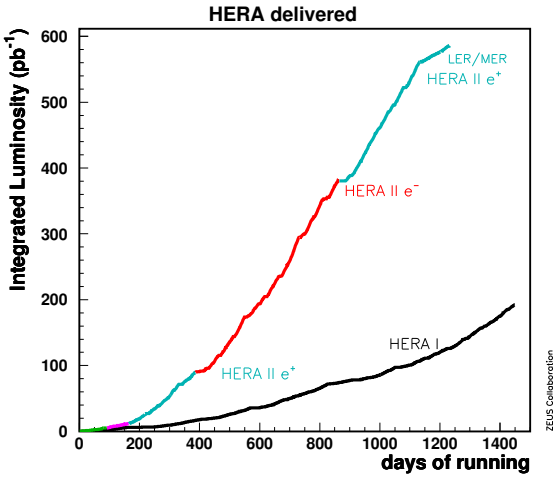

Figure 3.2: HERA delivered luminosity for the whole data-taking period.

polarisation. The lepton polarisation was relevant to high Q^2 physics [91], but did not have an impact on the present analysis.

3.2 The ZEUS Detector

The ZEUS detector [75] was one of two multi-purpose particle detectors designed to measure final states from electron–proton collisions at HERA, the other being H1. Figure 3.3 shows a cutaway of the ZEUS detector showing its main components. The detector was constructed onion-like and covered almost the complete 4π range around the interaction region allowing a precise measurement of the position, momentum and energy of the detected final states. In order to account for the difference in beam energies between electrons and protons, which resulted in a boosted centre-of-mass system, the detector had more instrumentation in the direction of the outgoing proton beam, also called the forward direction.
During the HERA shutdown, the silicon micro vertex detector (MVD) [76] was installed to improve the measurement of the impact parameter and secondary vertices in the immediate vicinity of the interaction region. Furthermore, it supported the measurement of charged tracks, which was performed by the central tracking detector (CTD) [78–80], a cylindrical drift chamber surrounding the MVD. The tracking detectors were further surrounded by a superconducting solenoid providing a magnetic field of 1.43 T which was needed to allow the measurement of the momentum of charged particles. In the forward direction, the forward detector (FDET) consisted of three planar drift chambers and two modules of the straw-tube tracker (STT) [77]. The tracking detectors and the magnet were further surrounded by an uranium–scintillator calorimeter (CAL) [81–84], the main device to measure the energy deposits of final state parti-

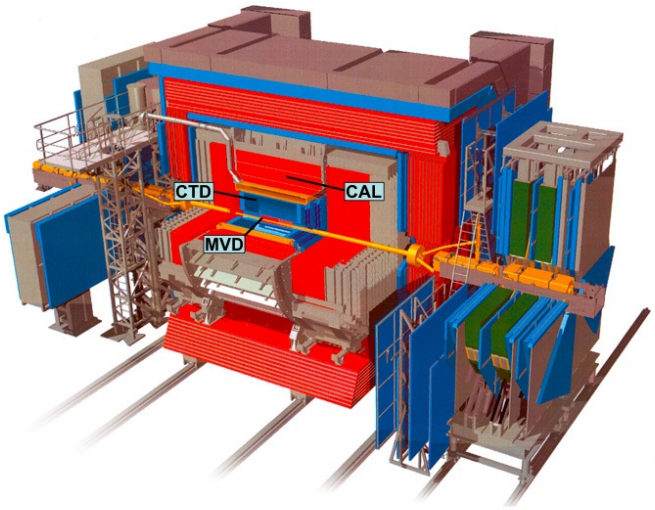

Figure 3.3: Cutaway of the ZEUS detector showing its main components.

cles. The calorimeter was divided into forward (FCAL), barrel (BCAL) and rear (RCAL) segments, and each of these segments consisted of an inner electromagnetic (EMC) and an outer hadronic section (HAC). Particles passing the hadronic section had to be identified by applying more sophisticated techniques which usually involved different detector components, e.g. the muon detectors.

3.2.1 The Micro Vertex Detector (MVD)

The silicon micro vertex detector (MVD) [76] was installed in order to improve the spatial resolution of the tracking system in the immediate vicinity of the interaction region. The MVD allowed the reconstruction of the impact parameter and secondary vertices of weakly decaying heavy flavoured hadrons, both of which were used in the present analysis for the measurement of differential cross sections. The MVD was a silicon strip detector consisting of two parts, the barrel (BMVD) and the forward (FMVD) section. The BMVD was composed of three layers of silicon strip detectors, which were mounted cylindrically around the beampipe on 30 ladders. Each ladder consisted of five modules composed of two half-modules. Each of these half-modules was made of two silicon sensors, which were mounted perpendicular to each other. The construction assured that one sensor would measure the position in the z-direction, while the other provided the $r-\phi$ information of the hit [1]. Overall, there were 512 strips per sensor that were read

[1]The ZEUS coordinate system is a right-handed Cartesinan system, with coordinate origin at the nominal interaction point. The z-axis is pointing in the proton beam direction, defined

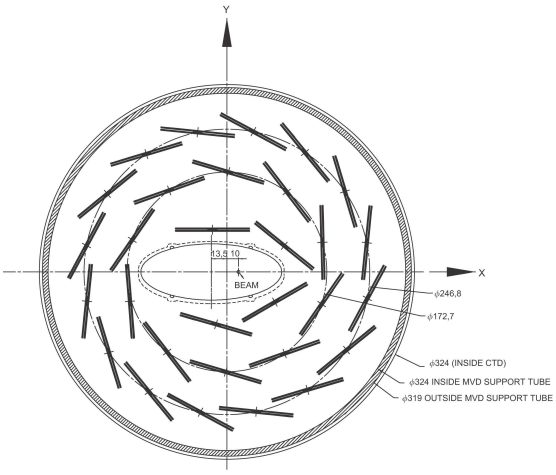

Figure 3.4: Cross section of the BMVD.

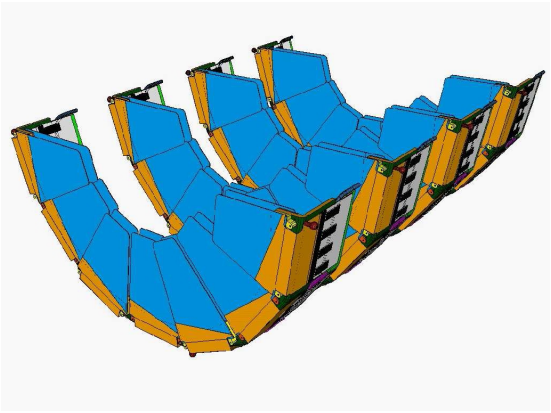

Figure 3.5: Lower half of the FMVD.

out with a distance of 120 μm between them.
A cross section of the barrel section of the micro vertex detector perpendicular to the beampipe is shown in figure 3.4. The beampipe is not completely surrounded by three layers due to its elliptical shape. For tracks with at least three hits, polar angles in the range $30° < \theta < 150°$ were covered. In order to increase the coverage from 30° to 7°, silicon sensors were installed in four vertical planes in the forward region. The FMVD is shown in figure 3.5. It was composed of four wheels that were mounted perpendicular to the beampipe consisting of 14 sectors. Each sector contained an inner and an outer sensor, which were mounted back to back. The sensors in the FMVD were wedge-shaped forming an angle of 180°/14 between the inner and the outer sensor.

3.2.2 The Central Tracking Detector (CTD)

The central tracking detector (CTD) [78–80] provided information about the position and momentum of charged particles, and was used together with the MVD for the track reconstruction. The CTD consisted of 72 cylindrical drift chamber layers, which were grouped in 9 superlayers and covered the polar angle region $15° < \theta < 164°$. Each superlayer consisted of 32 – 96 cells with the first superlayer having 32 cells and each further superlayer having 8 more cells. Odd-numbered superlayers had drift wires running parallel to the z-axis, while the even-numbered superlayers consisted of wires running at an angle of ±5° with respect to the z-axis. This orientation was chosen to allow for the measurement of the $r - \phi$ and z coordinates of tracks hitting the wires. An octant of the CTD in $x - y$ view is shown in figure 3.6. The position resolution of the CTD for

as the “forward direction”, and the x-axis towards the centre of HERA.

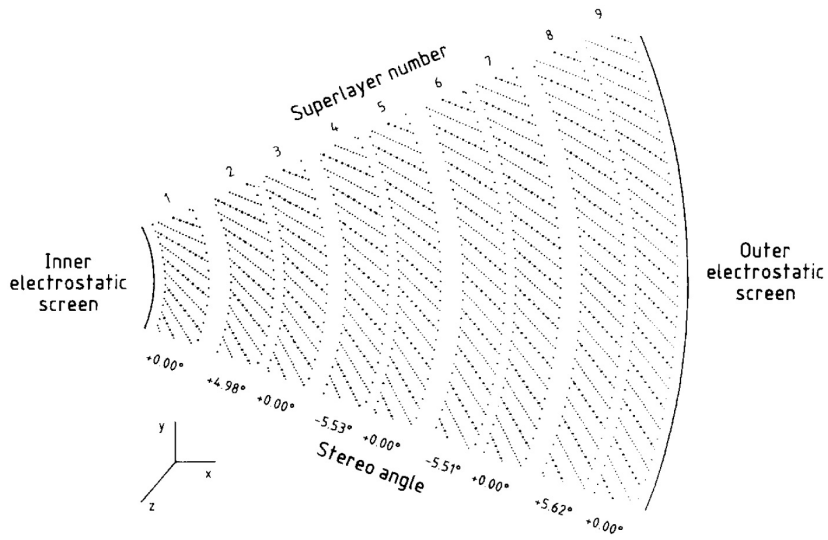

Figure 3.6: An octant of the CTD in $x - y$ view.

tracks passing through 3 or more superlayers was $\approx 300\mu$m in the $r - \phi$ plane and $\approx 1 - 5$ mm in the z-direction. The drift chamber was filled with a mixture of argon, CO_2 and ethane bubbled through ethanol, and the identification of particles was possible due to the measurement of the mean energy loss of charged particles in the active volume.

3.2.3 The Straw Tube Tracker (STT)

The Straw Tube Tracker (STT) [77] was installed during the upgrade to improve the track reconstruction in the forward region. The composition of the STT is illustrated in figure 3.7. It consisted of two modules, each made of 24 sectors that were grouped into four superlayers which contained six sectors. A superlayer covered the whole azimuthal angle, and consisted of a combination of two layers that were rotated by 60°. The four STT superlayers were again rotated with respect to each other, the angular difference between superlayers 1 and 2 as well as 3 and 4 being 30°, while the angular difference between superlayers 2 and 4 was only 15°.
Every sector of the STT consisted of three layers of straws with a diameter of 7.5 mm acting as an independent drift chamber. The straws consisted of a cover made of capton foil coated with aluminium and carbon that served as the cathode and a signal wire in the middle of the straw serving as the anode. A charged particle passing through a straw would ionise the Ar/CO_2 gas inside, and the electrons drifting to the anode would subsequently produce a signal. Since the positions of the wires in the straw tubes were known, these hits allowed the reconstruction of the particle's trajectory through the detector. The STT consisted of 10944 straws, and allowed detection of tracks in the angular range $6° < \theta < 25°$.

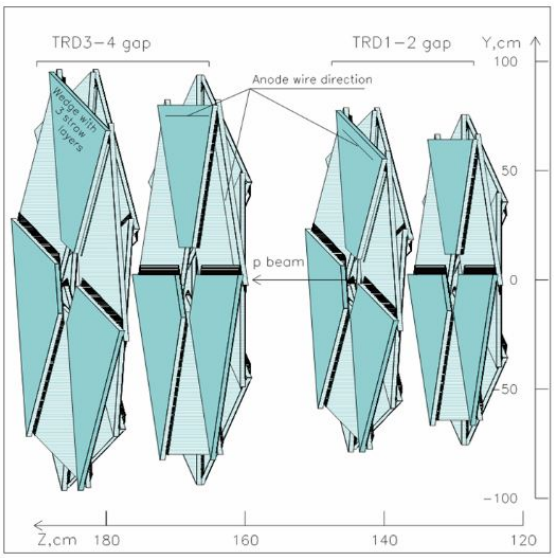

Figure 3.7: Composition of the Straw Tube Tracker (STT).

3.2.4 The Uranium Calorimeter (CAL)

The measurement of the energy deposits of particles was performed using the uranium–scintillator calorimeter (CAL) [81–84], which was divided into the forward (FCAL), barrel (BCAL) and rear (RCAL) sections, and nearly covered the full solid angle. As the centre-of-mass system was boosted at HERA due to the difference between the proton and electron energy, the forward section was constructed thicker than the rear section. The corresponding design resulted in interaction lengths of 6, 4 and 3 λ for the FCAL, BCAL and RCAL respectively. A schematic of the CAL is shown in figure 3.8 portraying the three sections.
The calorimeter sections were further subdivided into electromagnetic and hadronic towers (20 mm $\times$ 20 mm) made of alternating layers of depleted uranium (3.3 mm) used as absorber and plastic scintillator (2.6 mm) used as active material. Generally calorimeters respond differently to electromagnetic than to hadronic showers, because hadrons suffer from energy loss in nuclear interactions, which do not produce a measurable signal. In this context uranium produces a high yield of spallation neutrons, which can be detected using plastic scintillators. The neutrons create recoil protons upon scattering on hydrogen nuclei and photons from neutron capture, which can be detected compensating for the energy loss of hadronic showers. The uranium calorimeter was a compensating calorimeter, because an equal response to electromagnetic and hadronic showers was obtained by tuning the ratio between absorber and active material. The energy resolution of the calorimeter for electromagnetic, $\sigma_{el}(E)/E$, and hadronic showers, $\sigma_{had}(E)/E$, as measured under test beam conditions was found to be:

$$\frac{\sigma_{el}(E)}{E} = \frac{18\%}{\sqrt{E}}; \qquad \frac{\sigma_{had}(E)}{E} = \frac{35\%}{\sqrt{E}}, \tag{3.1}$$

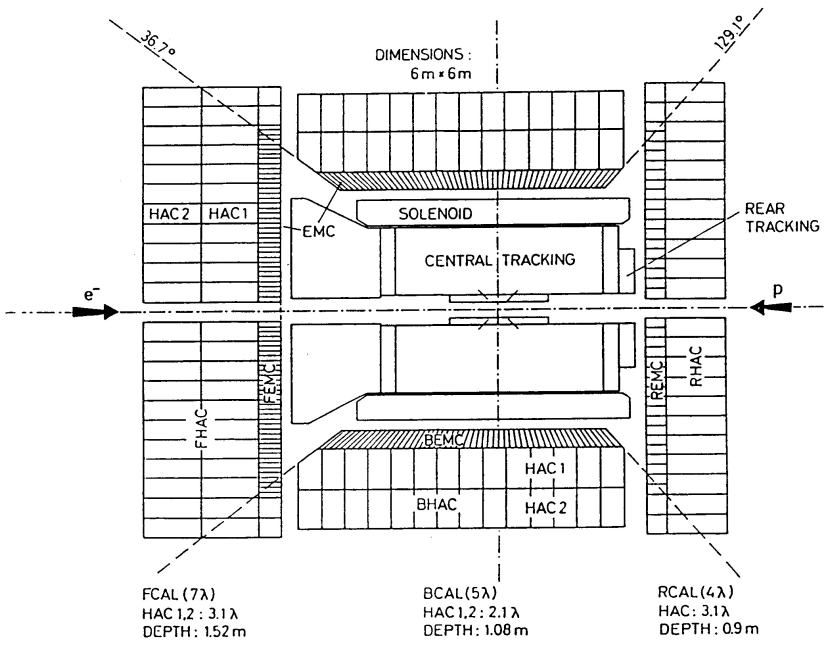

Figure 3.8: Schematic of the ZEUS uranium calorimeter in $x - y$ plane.

with E in GeV.
The calorimeter contained in total 5918 cells that were read out on both sides using photomultiplier tubes (PMT). Photons emitted in the active material of a module were channelled via light guides and wavelength shifters positioned at each side of the module. The differing signals from each PMT gave positional information of an electromagnetic or hadronic shower. Also, the timing resolution of the calorimeter allowed rejection of non ep background with characteristic timing patterns, and the activity coming from the U^{238} was used for calibrations.

3.2.5 The Luminosity Measurement

The luminosity $\mathcal{L}$ is defined as the number of particles colliding per unit time and unit area. At HERA the luminosity is defined in the following way:

$$\mathcal{L} = \frac{N_e \cdot N_p \cdot n_b \cdot f}{4\pi \cdot \sigma_x \cdot \sigma_y}, \tag{3.2}$$

where N_e and N_p denote the numbers of electron and protons per bunch, n_b is the number of bunches, f is the bunch-crossing frequency and σ_x and σ_y are the standard deviations of the beam cross section in x- and y-direction at the interaction point.
The total integrated luminosity recorded with the ZEUS detector during both data-taking periods was $\mathcal{L} = 0.5\,\mathrm{fb}^{-1}$ with a relative error of $\Delta\mathcal{L}/\mathcal{L} \approx 2$ %. The luminosity at HERA was measured using two lead−scintillator calorimeters [85–87] that detected photons from the Bethe–Heitler process $ep \to e'p\gamma$. The cross

section for this process is well known at fixed photon scattering angle and energy, which allows extraction of the integrated luminosity $\mathcal{L}$ using the relation

$$\mathcal{L} = \frac{N}{\sigma_{BH}}, \tag{3.3}$$

where N is the number of detected events and σ_{BH} is the Bethe–Heitler cross section.

3.2.6 The Trigger and Data Acquisition System

As the storage space is limited it is not possible to store the complete amount of data generated in high-energy physics collider experiments. At HERA bunches of particles collided every 96 ns at the interaction points, which corresponded to a bunch crossing rate of 10.4 MHz. Only a small fraction of these interactions contained interesting physics events, while the majority of the background events constituted beam gas interactions. These occur when the electrons or protons interact with nuclei of the residual gas or the beampipe.

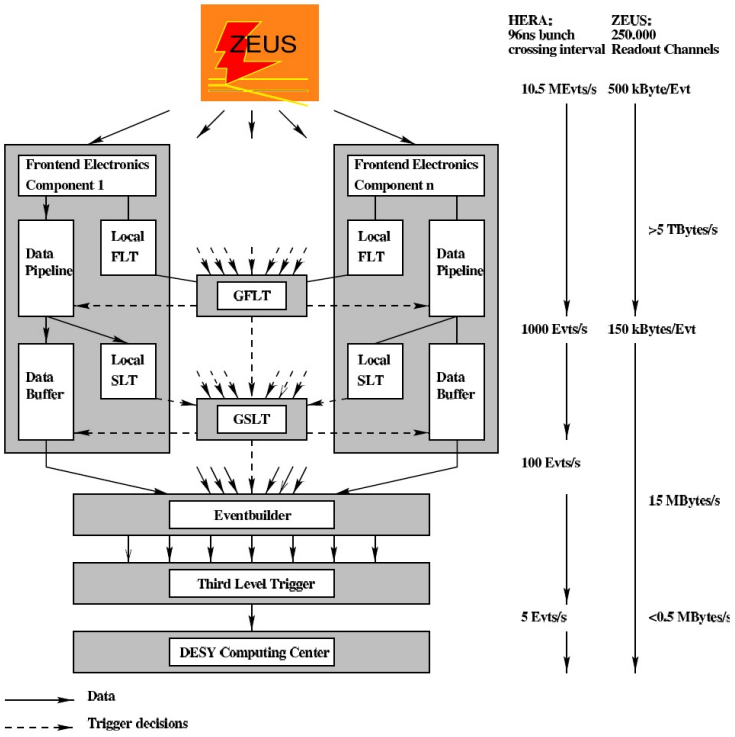

Figure 3.9: The ZEUS Trigger and Data Acquisition System.

At ZEUS a three-level trigger system [88] was developed which distinguished potentially interesting physics events from non-*ep* background reducing the amount

of data that had to be stored and subsequently processed. A schematic of the trigger and data acquisition system is shown in figure 3.9. At the first level, a hardware trigger was used to reduce the event rate to below 1 kHz. The information about an event was initially stored in pipelines and prepared for the trigger decision within 2 μs after the bunch crossing. Each detector component had individual first level trigger electronics [92, 93], which passed the information to the global first level trigger (GFLT). The GFLT performed the decision within a time interval of 4.4 μs and returned the relevant information to the readout systems of the detector components.
The global second level trigger (GSLT) [94] was software-based and processed information received from the second level triggers of the individual detector components providing a decision within a few milliseconds. In comparison with the first level trigger more time was available to take the decision whether to accept or reject the event, and therefore more complex information could be processed leading to more sophisticated algorithms for the event selection, depending on the event topology. Information processed by the global second level trigger included timing and global energy sums from the calorimeter as well as information about preliminary track and vertex reconstruction, reducing the event rate to below 100 Hz.
In case an event had not been rejected by the FLT or SLT, the individual detector components transmitted their information to the so-called event-builder [95]. The event-builder collected the available data and performed a first reconstruction of the event. The third level trigger (TLT) [96] then used variables from this reconstruction and decided whether or not the event should be stored for further analysis. After passing all three stages of trigger selection the event rate had reduced to a few Hz. The data for the selected events was then stored on ADAMO tables, which could be processed using the offline reconstruction program ZEPHYR.

Chapter 4

Event Reconstruction

Events accepted by the ZEUS trigger system were stored on tape for further analysis. This chapter illustrates the reconstruction of physical quantities from measurements performed with the individual detector components. In sections 4.1 and 4.2 the track [97–99] and vertex reconstruction [100] for the HERA II data taking period, which involved the MVD, will be reviewed. Energy flow objects (EFO) [101], combining information from the calorimeter and the tracking systems, are defined in section 4.3. Section 4.4 reviews the reconstruction of the scattered electron [102, 103], the primary signature for DIS events. The k_T clustering algorithm [104–106] that was applied in the present analysis to reconstruct jets of final state particles is defined in section 4.5. Finally, section 4.6 reviews the reconstruction of the kinematic variables describing a DIS event.

4.1 Track Reconstruction

For the present analysis it was crucial to achieve a precise track reconstruction for the HERA II dataset. The trajectory of a charged particle in a uniform magnetic field parallel to the beampipe can be described by a five parameter helix. The parametrisation is based on the definition of the point of closest approach (pca), i.e. the point on the helix in the $x-y$ plane closest to the chosen reference point. The five track parameters $\varphi_H, D_0, Z_H, W, \cot\theta$ needed to define the track helix illustrated in figure 4.1 are given by:

- φ_H: the azimuthal angle of the direction vector of the helix at the point of closest approach to the reference point,
- $D_0 = Q \cdot D_H$: product of the charge Q and the distance from the reference point to the point of closest approach in the $x-y$ plane,
- $W = Q/R$: the quotient of the charge Q to the radius R of curvature,

- Z_H: the distance from the reference point to the point of closest approach projected onto the z axis,
- cot θ, where θ denotes the polar angle of the track.

The first three parameters parametrise a circle in the $x-y$ plane, while the latter two parameters describe the location and pitch of the trajectory in z-direction. The transverse momentum p_T of the charged particle can be determined from the curvature of the reconstructed track helix using the relation $p_T = 0.3\,Q\,R\,B$, where B describes the magnetic field. The momentum of the particle is then extracted exploiting the relation $p = p_T / \sin\theta$.
Provided the track helix can be described in terms of these parameters the point of closest approach is given by

$$\vec{D_H} = \begin{pmatrix} x_0 \\ y_0 \\ z_0 \end{pmatrix} = \begin{pmatrix} D_H \sin\varphi_H \\ -D_H \cos\varphi_H \\ Z_H \end{pmatrix}. \tag{4.1}$$

On the other hand, the trajectory of the track is parametrised in the following way:

$$\begin{pmatrix} x \\ y \\ z \end{pmatrix} = \begin{pmatrix} D_H \sin\varphi_H + \frac{1}{W}\cos\varphi_H \sin(W s_\perp) + \frac{1}{W}\sin\varphi_H\,[1-\cos(W s_\perp)] \\ D_H \cos\varphi_H + \frac{1}{W}\sin\varphi_H \sin(W s_\perp) + \frac{1}{W}\cos\varphi_H\,[1-\cos(W s_\perp)] \\ Z_H + \tan\theta\, s_\perp \end{pmatrix}, \tag{4.2}$$

where $s_\perp = s\sin\theta$, and s is defined as the distance along the trajectory from the point of closest approach to the reference point.

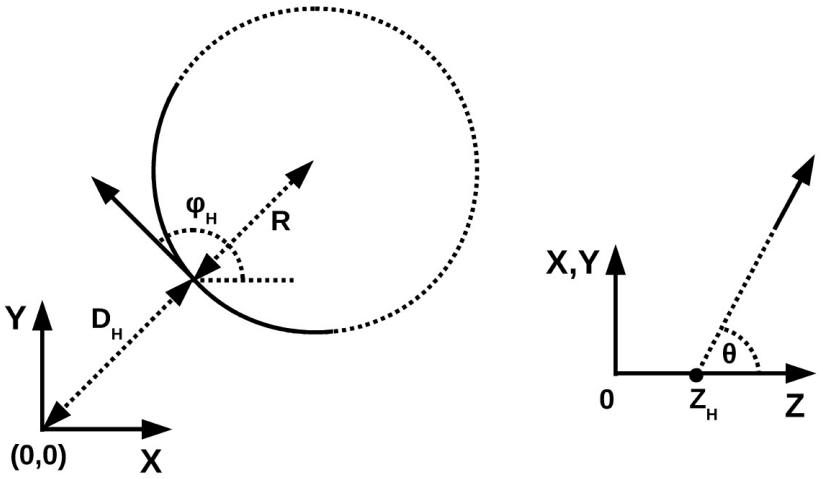

Figure 4.1: Parameterisation of track helix in $x-y$ plane and $y-z$ plane

After the detector upgrade, 2000 – 2002, the global tracking combined information from the MVD and the CTD to reconstruct tracks originating from charged

particles. In a first step the hit positions of the individual subdetectors were reconstructed using detector specific software. In a second step a combined pattern recognition was performed based on reconstructed hits from the individual detector components [97, 98].
The track seed was defined as a group of hits in the most outward component of the tracking detector. Seeds in the forward region were required to have at least eight hits in the STT, otherwise the central tracking detector was used for the track finding. Track candidates in the CTD started from seeds consisting of three hits in an axial superlayer, and were then extrapolated inwards acquiring additional hits. Once the trajectory spanned several superlayers, information from the three innermost superlayers was used for the extrapolation.
The seeds served as the starting point for the extraction of track parameters and were connected to the interaction point using an estimation of the momentum and charge of the track candidate. This connection established the direction in which one expected to find further hits for the matching. The connection of hits in the outer part of the detector with the interaction point picked up hits produced in the inner parts of the detector forming a road of hits from the STT, CTD and MVD. The hits found in this pattern recognition were used as input parameters for the rigorous track fit [99], which used the Kalman filter technique [107] accounting for inhomogeneities of the magnetic field and the energy loss due to multiple scattering to determine the track helix parameters.

4.2 Vertex Reconstruction

Originally the primary vertex was reconstructed by choosing a set of well-reconstructed tracks, calculating the centre-of-gravity for these tracks, and iteratively minimising the χ^2 of the fitting procedure. Tracks contributing to an increased χ^2 were systematically discarded until the remaining tracks contributed to a fit that fulfilled the criterion $\chi^2 < \chi^2_{cut}$. In this way a well-reconstructed primary vertex with the corresponding set of tracks that contributed to the vertex reconstruction could be found.
The described procedure was extended by a Deterministic Annealing Filter (DAF) [100] which replaced the fixed χ^2 cut applied to the tracks by a weight function:

$$w(\chi^2, T) = \frac{1}{1 + \exp\left(\frac{\chi^2 - \chi^2_{cut}}{2T}\right)}, \tag{4.3}$$

where T is a temperature and χ^2_{cut} is a cut parameter.
In a first step the initial procedure was applied to select an appropriate set of tracks and reconstruct the corresponding primary vertex. In a second step the weight function with a high temperature T was applied to the same set of well-reconstructed tracks in order to refine the vertexing and track finding procedure.

The weighted fit was then repeated using a smaller temperature T, which allowed refinement of the vertex reconstruction and selection of another subset of tracks. This procedure was repeated until a certain temperature T of convergence was found.
Furthermore, tracks that were far away from the primary vertex and could not be fitted to it properly were removed by requiring the vertex to be close to the interaction point. The beam spot was defined as the 3 dimensional distribution of collisions where the electron and proton beams overlap. The centre of the beam spot was determined every 2000 events [108] by fitting Gaussian curves to the x, y and z distributions of the primary vertex. The RMS of the beam spot was found to be 80 μm/88 μm in the x and 22 μm/20 μm in the y direction for the e^-p/e^+p data [109]. The beam spot in the z-direction was found to be approximately 8 cm wide.
The beam tilt consisted of a slope of the incoming beams in the x- and y-directions with respect to the z-axis. This slope could be determined by dividing the x and y vertex distribution into z-intervals and fitting the resulting distributions with a Gaussian. The mean values of these Gaussians were then fitted with straight lines allowing extraction of the slopes in x and y. The beam spot position was used as an additional constraint in the fitting procedure of the primary vertex. Subsequently, the DAF extended for the beamspot constraint became the standard technique for primary vertex finding in ZEUS leading to an improvement in the precision and resolution.

4.3 Energy Flow Objects (EFO)

The energy resolution of the CAL develops for high energies as $\sigma(E)/E \sim 1/\sqrt{E}$ providing an improved resolution with increasing energy. On the other hand, the momentum resolution of reconstructed tracks is parametrised by

$$\sigma(p_T)/p_T = a \cdot p_T \oplus b \oplus c/p_T.$$

In comparison with the calorimeter it provides a better resolution at low transverse energy. Therefore a combination of information from the calorimeter and the tracking system could improve the reconstruction of hadronic final states. The resulting objects are called Energy Flow Objects (EFOs) [101], which were reconstructed in the four steps illustrated in figure 4.2:

1. Particles traversing the CAL deposited at least parts of their energy in the calorimeter cells. Adjacent cells were merged into cell islands using a clustering algorithm that associated each cell to the neighbour with the highest energy deposit. This procedure defined a unique prescription to assign each calorimeter cell to a cell island that contained the energy deposit of showers caused by the incident particles.

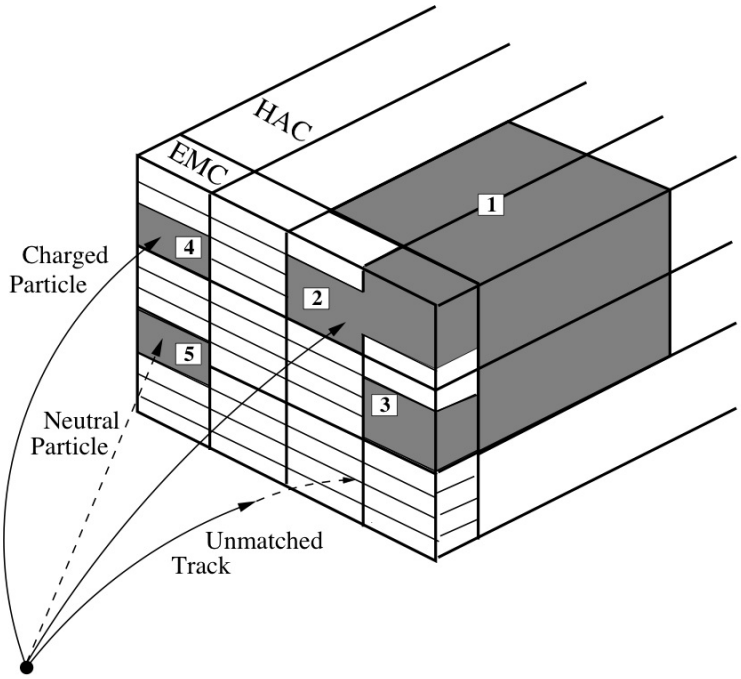

Figure 4.2: Illustration of the clustering algorithm. Initially there are four EMC cell islands and one HAC cell island. EMC cell islands 1 and 2 are then merged with the HAC cell island forming a single cone island. The cone islands are then matched to reconstructed tracks.

2. The cell islands were then clustered in the $\theta - \phi$ plane obtaining three dimensional objects called cone islands. The position of the cone islands was determined using the logarithmic centre-of-gravity of the electromagnetic or hadronic shower.

3. In the third step, tracks satisfying certain criteria were extrapolated to the calorimeter and matched to the cone islands. For the matching only tracks in the transverse momentum range $0.1 < p_T < 20$ GeV passing at least 4 CTD superlayers and tracks in the momentum range $20 < p_T < 25$ GeV passing at least 7 CTD superlayers were considered. The matching was only performed if the distance of closest approach between the tracks and the cone island was less than 20 cm or the tracks were lying within the area of the island. The object resulting from the matching of the tracks and cone islands was called a ZEUS Unidentified Flow Object (ZUFO).

4. In the final step, the energy and momentum of the ZUFOs were extracted from the available calorimeter and tracking information. When one track was matched to one cone island, the energy was taken either from the calorimeter or the track momentum depending on the resolution of the corresponding measurement. The same algorithm was applied for tracks

matching multiple islands or two tracks matching one or two islands, while considering the sum of energies and momenta for these cases. When more than three tracks were matched to a cone island the object was defined to be a jet and the energy was taken from the calorimeter. For well-reconstructed tracks that do not have a matching cone island the energy was taken from the track momentum assuming the pion mass m_π. For cone islands without a matching track the calorimeter information was used assuming that the energy deposit originates from a neutral particle.

Additional corrections had to be applied to account for the material budget of the detector, inefficiencies in the region between the calorimeter sections and other effects. In the present analysis ZUFOs were used to reconstruct jets defined with the k_T cluster algorithm and calculate kinematic variables and $E - p_z$.

4.4 Electron Reconstruction

The primary signature characterising neutral current DIS events was the presence of a scattered electron in the calorimeter. Electron candidates were identified using the SINISTRA algorithm [102, 103] that was based on a neural network.

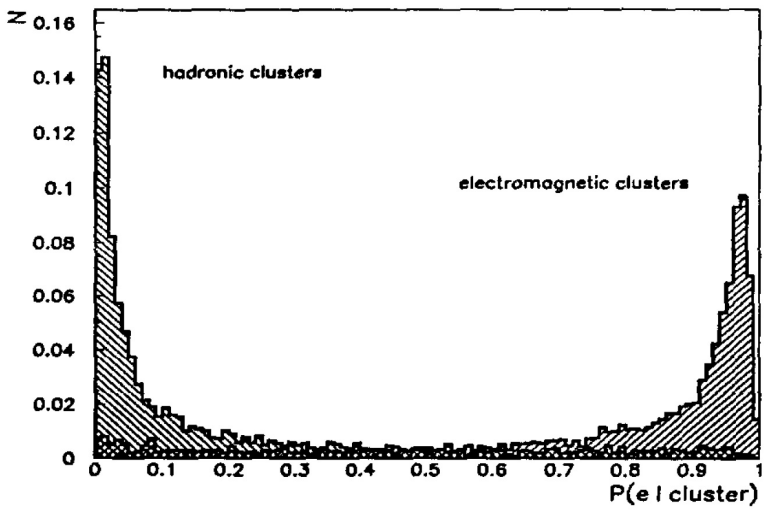

Figure 4.3: Probability for a calorimeter cluster to be an electromagnetic cluster as determined by the SINISTRA algorithm.

In section 3.2.4 it was explained that electromagnetic and hadronic showers were caused by particles passing through the detector depositing energy in the CAL. In order to identify an electron candidate neighbouring cells were initially grouped into islands. The islands from different calorimeter sections were then merged, and the corresponding energy deposit was used to calculate the longitudinal and

transverse energy distributions of the shower. The resulting information was passed to the neural network, that was trained on simulated electromagnetic and hadronic clusters in the RCAL. The primary criterion for electron identification used by the neutral network was the shower shape as hadronic showers were typically transversely broader and longitudinally deeper than electromagnetic showers.
The output of the SINISTRA algorithm represents the probability that the particle causing the shower in the calorimeter is the scattered electron. The characteristic output of the electron finder is shown in figure 4.3. In this context, candidates with a probability greater than 0.9 were considered as electron candidates. In case there were several such candidates, the candidate with the highest probability was identified as the scattered electron. The energy from the corresponding island represented the electron energy, E_e, and was corrected for energy losses in the inactive material. In the present analysis only electrons above a threshold of $E_e = 10\,\text{GeV}$ were considered.

4.5 Jet Reconstruction

Since quarks and gluons are confined inside the proton, they cannot be observed directly in DIS, but need to be detected indirectly by exploiting the correlation between the partons and the final state particles that can be measured with the detector. Heavy quarks are produced in the hard subprocess of DIS and subsequently fragment into hadrons constituting a collimated cluster of particles referred to as jet. An appropriate definition of jets is therefore crucial to compare experimental results with theoretical predictions and probe perturbative QCD at a hard scale.
Several algorithms are available to reconstruct jets from calorimeter cells, objects combining calorimeter and tracking information, hadrons or partons in theoretical codes or simulations. Generally, jet finding algorithms are required to be infrared and collinear safe meaning that the reconstructed jets need to be insensitive to the emission of low energy particles and collinear splittings [110]. From an experimental point of view a collinear safe algorithm is unaffected by the resolution of two collinear particles hitting the same calorimeter cell. On the other hand, infrared safety corresponds to the statement that the jet algorithm is independent of the exact energy threshold and the eventual noise in the calorimeter cells.
For the present analysis the k_T cluster algorithm [104–106] was used for the jet reconstruction, which is based on the successive combination of close object pairs into clusters. The algorithm consisted of the following steps:

1. A list of all measured objects and a list of all reconstructed jets is made.

2. For every object i the distance $d_i = E_{T,i}^2$ to the beam axis is calculated.

3. For every pair of objects i and j the distance $d_{ij} = \min(E_{T,i}, E_{T,j})^2 \Delta R_{ij}^2$ between the two objects is calculated, where the quantity ΔR_{ij} is the distance between the objects in the $\eta - \phi$ plane.

4. The minimum of all available distances $\{d_i, d_{ij}\}$ is calculated.

5. If $\min(d_{ij}) < \min(d_i)$ objects i and j are combined into a new object k:

$$E_{T,k} = E_{T,i} + E_{T,j},\ \eta_k = \frac{E_{T,i} \cdot \eta_i + E_{T,j} \cdot \eta_j}{E_{T,i} + E_{T,j}},\ \phi_k = \frac{E_{T,i} \cdot \phi_i + E_{T,j} \cdot \phi_j}{E_{T,i} + E_{T,j}}.$$

6. If $\min(d_i) < \min(d_{ij})$ the object i is removed from the list of objects and added to the list of reconstructed jets.

7. These steps are iterated until the smallest quantity in the list $\{d_i, d_{ij}\}$ is above a certain threshold, d_{cut}. The value of d_{cut} was set to 1 GeV^2 for the present analysis.

Note that for small angles, φ, between the objects i and j in the $\eta - \varphi$ plane the distance d_{ij} becomes:

$$d_{ij} = \min(E_{T,i}, E_{T,j})^2 \Delta R^2 \approx \min(E_i, E_j)^2 \Delta\varphi^2 \approx k_T^2,$$

which gives the algorithm its name. The advantage of the k_T cluster algorithm is that it naturally avoids the problem of overlapping jets. For the present analysis only those jets were considered that did not contain the DIS electron.

4.6 Kinematic Variables

A DIS event at HERA is completely described by any two of the Lorentz scalars Q^2, x and y. There are various methods to reconstruct these variables using a combination of the energy, E'_e, and polar angle, θ_e, of the scattered electron as well as the longitudinal and transverse momentum of the hadronic final state. The choice of an appropriate reconstruction method depends on the detector and kinematic region. In the present analysis the electron and Jacquet-Blondel method have been used to determine the upper and lower boundaries of the Bjorken y variable. The double-angle method has been used to determine the photon virtuality Q^2 and Bjorken x in the whole region of the phase space.

Electron Method

The electron method [111] is based on the measurement of the energy, E'_e, and polar angle, θ_e, of the scattered electron. As only one particle needs to be reconstructed, the electron method is the simplest method for the reconstruction

of the kinematic variables. In this formalism the DIS variables are given by:

$$Q_e^2 = 2E_e E'_e(1 + \cos\theta_e), \tag{4.4}$$

$$y_e = 1 - \frac{E'_e}{2E_e}(1 - \cos\theta_e), \tag{4.5}$$

$$x_e = \frac{Q_e^2}{s y_e}, \tag{4.6}$$

where E_e is the energy of the incoming electron. The electron method is sensitive to initial and final state radiation, which leads to a poor resolution in the kinematic region of low x and y.

Jacquet-Blondel Method

The Jacquet-Blondel method [112] is based on the reconstruction of the energy and momentum of the hadronic final state. The method is sensitive to the hadronic energy scale, and requires that the hadronic activity is contained and well-measured. In this context, one assumes that hadrons which are not detected escape through the beampipe and their transverse momentum is consequently neglected. One defines the variable δ_h in the following way:

$$\delta_h = \sum_i (E_i - p_{z,i}), \tag{4.7}$$

where the sum runs over all reconstructed particles. In this method the DIS variables are given by:

$$y_{\mathrm{JB}} = \frac{\delta_h}{2E_e}, \tag{4.8}$$

$$Q^2_{\mathrm{JB}} = \frac{p^2_{T,h}}{1 - y_{\mathrm{JB}}}, \tag{4.9}$$

$$x_{\mathrm{JB}} = \frac{Q^2_{\mathrm{JB}}}{s \cdot y_{\mathrm{JB}}}, \tag{4.10}$$

where $p_{T,h} = \sqrt{(\sum_i p_{x,i})^2 + (\sum_i p_{y,i})^2}$ is the transverse momentum of the hadronic system and the sum runs over all reconstructed EFOs. Although the photon virtuality Q^2 is not well-reconstructed with the hadronic system, the Jacquet-Blondel method is more precise than the electron method in the kinematic region of low y.

Double-angle Method

The double-angle method [111] uses the polar angle of the electron, θ_e, and the hadronic final state, γ_h, which is used as an estimator for the scattering angle of

the struck quark. In the naive quark parton model the angle γ_h can be reconstructed using the following equation:

$$\cos\gamma_h = \frac{p_{T,h}^2 - \delta_h^2}{p_{T,h}^2 + \delta_h^2}. \tag{4.11}$$

The DIS variables are then determined in the following way:

$$Q_{\mathrm{DA}}^2 = 4E_e^2 \frac{\sin\gamma_h(1+\cos\theta_e)}{\sin\gamma_h + \sin\theta_e - \sin(\theta_e+\gamma_h)}, \tag{4.12}$$

$$y_{\mathrm{DA}} = \frac{\sin\theta_e + (1-\cos\theta_e)}{\sin\gamma_h + \sin\theta_e - \sin(\theta_e+\gamma_h)}, \tag{4.13}$$

$$x_{\mathrm{DA}} = \frac{E_e}{E_p} \frac{\sin\gamma_h + \sin\theta_e + \sin(\theta_e+\gamma_h)}{\sin\gamma_h + \sin\theta_e - \sin(\theta_e+\gamma_h)}. \tag{4.14}$$

The double-angle method provides the most precise results over a large fraction of the phase space, since it is less sensitive to energy scales and radiative corrections. In particular, compared with the electron method the double-angle method, it provides a better resolution at $Q^2 > 100$ GeV^2 [111].

Chapter 5

Data Sample and Signal Extraction

The subjects of the present chapter are the data sample and the technique of signal extraction used for the measurement of the charm contribution to the structure function of the proton. An overview of the data and MC samples used in the present analysis will be given in section 5.1. The event selection will be explained in section 5.2, giving a detailed explanation of the trigger configuration, and the DIS and jet selection. The subject of section 5.3 will be the technique of signal extraction that has been developed to make a fully inclusive measurement of charm-jet cross sections in DIS events. In a first step the standard technique of inclusive measurements with the ZEUS detector based on the decay length significance and secondary vertex mass will be explained. In a second step an alternative technique based on the impact parameter of jet-associated tracks will be illustrated. Finally, the combined algorithm that exploits the available information from secondary vertices and jet-associated tracks in DIS events, whilst avoiding correlations between the variables, will be presented.

5.1 Data Samples and Monte Carlo Sets

Data Samples

The data sample used for the inclusive analysis of the charm contribution to the structure function of the proton was collected in the period 2005−2007 and corresponds to an integrated luminosity of 331 pb^{-1}. The energy of the proton beam in the considered run periods was 920 GeV, while the energy of the electron beam was 27.5 GeV. An overview of the characteristics of the data sample is given in table 5.1.

Run period	Interaction	$\sqrt{s}$ [GeV]	$\mathcal{L}$[pb^{-1}]	σ_{sys}(%)
2005	e^-p	318	134.16	1.8
2006	e^-p	318	54.79	1.8
2006/07	e^+p	318	142.38	1.8

Table 5.1: Data samples collected with the ZEUS detector in the period 2005−2007. $\sqrt{s}$ represents the centre-of-mass energy of the electron−proton system, $\mathcal{L}$ the luminosity for the corresponding run period and σ_{sys} the relative systematic error of the measured luminosity value.

As the inclusive analysis required a combination of tracking and vertexing information, only data from the HERA II run periods was considered for the present analysis. Furthermore, events were preselected by requiring the EVTAKE and MVDTAKE routines: EVTAKE required that the calorimeter, central tracking detector, trigger chain and luminosity measurement were functioning properly. The MVDTAKE routine required the MVD to be in a good state during the data taking.

Monte Carlo Simulations

Final states from *ep* collisions in DIS at HERA were reconstructed after the previously described trigger and event selection. In order to simulate the underlying physics processes and evaluate the performance of the individual detector components, Monte Carlo (MC) generator techniques [113, 114] were applied. The MC simulation proceeds in four stages:

1. In a first step the initial state of an electron and a proton is simulated including the relevant initial state radiation.

2. In the second step the hard scattering process between the exchanged vector boson and the partons inside the proton is simulated on the basis of fixed-order perturbative QCD calculations.

3. In the third step the parton showering is simulated using MC techniques involving Sudakov factors to calculate the probability of quark and gluon emissions.

4. In the fourth step the fragmentation and hadronisation processes are simulated using phenomenological models that were tuned such that the MC simulation matched an array of data from different collider experiments.

Monte Carlo event generators simulate all stable final state particles of a given event. In order to compare the simulation with the data one needs to make sure that the corresponding final states are reconstructed in the same way. After the

event simulation the final state particles are therefore passed through a simulation of the ZEUS detector produced using the GEANT package [115–117]. The detector simulation provides information about signals originating from particles passing through the individual detector components. After a simulation of the trigger chain, the reconstruction used for the real data can be applied to the MC events. As a result the simulated events are analysed in the same way as the data. In the present analysis MC techniques are used to calculate hadronisation corrections to theoretical predictions and simulate the detector acceptance required to calculate the differential cross sections in the relevant kinematic regions.

Rapgap

Heavy quark production at HERA was simulated with the Rapgap MC generator [118] based on leading-order perturbative QCD calculations. In Rapgap the dominant production mechanism for charm and beauty quarks, BGF, is calculated using massive matrix elements, which allows predictions to be made in the threshold region of the heavy quark masses. On the other hand, computations of resolved processes, where the photon fluctuates into a quark – antiquark pair, are performed using massless matrix elements.
In order to account for the fact that quarks and gluons can radiate in the initial and final state and gluons can split into quark−antiquark pairs, higher order processes are simulated using parton showers. Parton showers are simulated as a sequence of particle branchings in the leading log (LL) approximation with the probabilities for the splittings given by the Sudakov form factors. This iterative procedure of quark and gluon splittings results in a particle cascade composed of complex multi-particle states.
The fragmentation and hadronisation processes cannot be described in perturbative QCD and therefore phenomenological models are required. In the Rapgap MC simulation the Lund string model [119–121] was applied to simulate the hadronisation. In this model the fraction, z, of the momentum of the struck parton that is transferred to the hadron is described by the Bowler [122] fragmentation function $D(z)$:

$$D(z) \propto \frac{1}{z^{1+r_Q b m_Q^2}}(1-z)^a \exp\left(\frac{-b m_\perp^2}{z}\right), \tag{5.1}$$

where the parameters a and b are determined from experiment. The variable m_Q is the mass of the heavy quark, $m_\perp$ is the transverse mass of the hadron, $m_\perp^2 = m^2 + (p_T^{rel})^2$, where m is the mass of the hadron and p_T^{rel} is the transverse momentum relative to the direction of the quark. For massive quarks, $r_Q = 1$ was predicted, and the parameter allows a smooth interpolation between the Bowler function and the symmetric Lund form [123] ($r_Q = 0$) that is applicable for light quarks.

For the present analysis, beauty events were generated for the photon virtuality $Q^2 > 1\,\mathrm{GeV}^2$ which covers the whole kinematic region including the beauty quark mass threshold. The standard Rapgap MC sample for charm quark events was generated for the photon virtuality $Q^2 > 4\,\mathrm{GeV}^2$ which covers the middle Q^2 region of high statistical significance. In order to cover the charm quark mass threshold and account for migrations into the kinematic region of the measurement, another Rapgap MC sample for the photon virtuality $Q^2 > 1.5\,\mathrm{GeV}$ was generated. An overview of the Rapgap Monte Carlo samples used for charm and beauty is given in tables 5.2 and 5.3. The CTEQ5L parametrisation of the parton densities in the proton was chosen, and the heavy quark masses were set to $m_c = 1.5\,\mathrm{GeV}$ and $m_b = 4.75\,\mathrm{GeV}$.

Run period	Interaction	$Q^2_{\mathrm{min}}\,[\mathrm{GeV}^2]$	$\mathcal{L}(\mathrm{pb}^{-1})$	$Q^2_{\mathrm{min}}\,[\mathrm{GeV}^2]$	$\mathcal{L}(\mathrm{pb}^{-1})$
2005	e^-p	1.5	147.5	4	282.95
2006	e^-p	1.5	43.07	4	168.60
2006/07	e^+p	1.5	141.95	4	496.91

Table 5.2: Overview of Rapgap MC samples used to simulate charm quark production in DIS events at HERA. $\mathcal{L}$ represents the luminosity of the corresponding run period, Q^2_{min} is the cut applied to the photon virtuality to generate the MC sample.

Run period	Interaction	$Q^2_{\mathrm{min}}\,[\mathrm{GeV}^2]$	$\mathcal{L}(\mathrm{pb}^{-1})$
2005	e^-p	1	2114.6
2006	e^-p	1	924.93
2006/07	e^+p	1	2577.93

Table 5.3: Overview of Rapgap MC samples used to simulate beauty quark production in DIS events at HERA. $\mathcal{L}$ represents the luminosity of the corresponding run period, Q^2_{min} is the cut applied to the photon virtuality to generate the MC sample.

Ariadne

The Ariadne program [124, 125] is one of the most successful QCD parton shower simulations to model hadronic final states at HERA. It is based on the colour dipole model [126–128], in which the parton showering is simulated by gluon emissions from colour dipoles formed by the final state particles in the hard interaction. The gluons can form further colour−dipoles which can radiate further

gluons or split into quark−antiquark pairs. The showering process proceeds until the dipoles have reached a certain minimum energy.
The Ariadne program has to be interfaced to other programs that generate the hard scattering process and model the hadronisation and decay of particles. For this analysis, Ariadne was interfaced to the DJANGOH [129, 130] event generator, which is an interface between the LEPTO [131] and HERACLES [132] programs. LEPTO provides leading-order QCD matrix elements for the hard interaction, while HERACLES accounts for initial and final state QED radiation, vertex and propagator terms and two-boson exchange.
The Ariadne MC generator simulated inclusive neutral current DIS events using massless matrix elements from the interface to LEPTO. As a consequence heavy flavour production could not be simulated properly at the mass threshold. Ariadne was therefore only used for studies of the light flavour background. The sample was generated for photon virtuality $Q^2 > 4\,\mathrm{GeV}^2$ with an integrated luminosity similar to that of the data. As for the Rapgap sample, the hadronisation was simulated using the JETSET program [133], which is based upon the Lund string model and uses a table of properties of well-known particle decays as reference.

5.2 Event Selection

In order to measure the charm contribution to the structure function of the proton, criteria need to be applied to select DIS events at HERA. In the first part of this section the first, second and third level trigger selection that was applied online will be given. The trigger efficiency is taken to be 100 % and possible inefficiencies are dealt with in the systematics. Finally, the neutral current DIS selection criteria and the jet selection criteria which were applied offline will be explained.

First Level Trigger (FLT)

Only events passing one or more FLT slots, which usually require a reconstructed track or energy deposit in the calorimeter [134, 135], were considered. The selection criteria of the trigger slots are as follows:

- **FLT28** At least one well-reconstructed track, an isolated EMC energy deposit in the BCAL or FCAL, and a total transverse energy in the calorimeter greater than 18 GeV.
- **FLT30** An isolated EMC energy deposit and an EMC energy deposit greater than 4 GeV in the RCAL.

- **FLT40** An EMC energy deposit in the calorimeter greater than 20 GeV.
- **FLT41** An energy deposit in the calorimeter with transverse energy greater than 30 GeV.
- **FLT43** At least one well-reconstructed track and an energy deposit in the calorimeter with transverse energy greater than 15 GeV.
- **FLT44** At least one well-reconstructed track, an isolated EMC energy deposit in the BCAL greater than 4.8 GeV and in the RCAL greater than 3.4 GeV.
- **FLT46** At least one well-reconstructed track and an isolated EMC energy deposit in the RCAL greater than 2 GeV.
- **FLT47** A total energy deposit in the calorimeter greater than 4 GeV, an isolated EMC energy deposit in the RCAL greater than 2 GeV.
- **FLT62** Multiple isolated EMC energy deposits in the calorimeter.

Second Level Trigger (SLT)

Events passing the FLT were required to pass the SPP01 slot of the SLT [134, 135]. The selection criteria of the SPP01 trigger slot were as follows:

- The event had to pass at least one of the FLT slots FLT28, FLT30, FLT40, FLT41, FLT43, FLT44, FLT46, FLT47, FLT62.
- $\sum_i (E - p_z)_i > 30\,\text{GeV}$, where the sum runs of all ZUFOs, which reduces photoproduction and non *ep* background.
- The event had to fulfill at least one of the following requirements:
  - EMC energy deposit in RCAL greater than 2.5 GeV
  - EMC energy deposit in BCAL greater than 2.5 GeV
  - EMC energy deposit in FCAL greater than 10 GeV
  - HAC energy deposit in FCAL greater than 10 GeV
- The reconstruction of a scattered electron in the RCAL with an electron energy greater than 5 GeV.

The SPP01 slot used did not impose tracking requirements.

Third Level Trigger (TLT)

The third level trigger applied trigger slots selecting neutral current deep inelastic scattering events [134, 135]. For the 2005 e^+p run periods the SPP02 trigger slots were used with the following requirements:

- The event had to pass the SPP01 slot of the second level trigger.
- The reconstruction of a scattered electron in the RCAL with electron energy greater than 4 GeV.
- The electron is detected outside a box of 24 $\times$ 24 cm^2 centered around the beam pipe.
- $30 < \sum_i (E - p_z)_i < 100$ GeV, where the sum runs over all ZUFOs.

For the 2006 e^-p and the 2006/2007 e^+p run periods the SPP02 trigger slot was replaced by SPP09, and the HPP31 and HFL17 triggers were additionally required [134, 135]. Apart from two modifications the SPP09 and HFL17 trigger slots imposed the same selection criteria as the SPP02 trigger. The HFL17 required additionally the reconstruction of at least two tracks in the CTD and the SPP09 contained a slightly larger box cut of 30 $\times$ 30 cm^2. The HPP31 imposed the following requirements:

- The event had to pass the SPP01 slot of the SLT.
- The reconstruction of a scattered electron candidate in the RCAL with electron energy greater than 7 GeV.
- The electron had to be detected outside a box of 24 $\times$ 24 cm^2 centered around the beam pipe.
- $\sum_i (E - p_z)_i > 34$ GeV, where the sum runs over all ZUFOs, which reduces photoproduction and non ep background.
- Reconstruction of the photon virtuality $Q^2 > 6\,\mathrm{GeV}^2$.
- The reconstruction of at least one track in the CTD with transverse momentum $p_T > 200$ MeV.

Neutral Current DIS Selection

After the trigger selection the following selection criteria were applied offline in order to select neutral current DIS events:

- The reconstruction of a scattered electron candidate outside a box of 26 × 26 cm^2 centered around the beampipe.
- An electron probability greater than 0.9 for the reconstructed candidate, determined with the electron finder SINISTRA, and electron energy $E'_e > 10\,\text{GeV}$.
- $44 < \sum_i (E - p_z) < 65$ GeV, where the sum runs over all ZUFOs, which reduces photoproduction and non ep background.
- The primary vertex reconstructed in the range $|Z_{\text{prm}}| < 30\,\text{cm}$.
- The photon virtuality reconstructed with the double-angle method in the range $5 < Q^2_{\text{DA}} < 1000\,\text{GeV}^2$.
- The reconstruction of the inelasticity with the Jacquet−Blondel and the electron methods with the following respective cuts: $y_{\text{JB}} > 0.02$ and $y_{\text{el}} < 0.7$.

The lower Q^2 cut is applied, since the electron candidate cannot be reconstructed reliably close to the beam pipe. On the other hand the upper Q^2 cut accounts for the inability of the SINISTRA algorithm to reconstruct electrons at high virtuality. The lower y cut assures the presence of hadronic activity, and uses the Jacquet-Blondel method, because it has the best resolution at low values of the inelasticity y. The higher y cut reduces background from photoproduction, and uses the electron method.

Jet Selection

Jets were reconstructed in deep inelastic scattering events using the k_T clustering algorithm in the longitudinally invariant mode [105] with the E_T recombination scheme [106]. As input to the k_T clustering algorithm all reconstructed EFOs were utilised, and jets containing the scattered electron were rejected. In contrast to previous analyses of heavy flavour production with the ZEUS detector the following cuts were applied for the jet selection:

- $E_T^{\text{jet}} > 2.5\,\text{GeV}$,
- $-1.6 < \eta^{\text{jet}} < 2.2$,

These jet selection cuts extend the kinematic region towards lower values of the transverse jet energy than previous analyses. The extension of the phase space towards lower values of E_T^{jet} gives increased statistics and reduces the extrapolation uncertainties when extracting $F_2^{c\bar{c}}$ at low values of the photon virtuality Q^2 and the scaling variable x.

5.3 Signal Extraction

The inclusive measurement of the charm contribution to the structure function of the proton was performed using a combination of tracking and vertexing information. In this section the inclusive techniques of heavy quark tagging based upon the decay length significance and secondary vertex mass of heavy flavoured hadrons and the impact parameter of jet-associated tracks will be detailed. In section 5.3.1 the reconstruction of secondary vertices and the method of mirroring and subtracting the signed decay length significance distribution in order to obtain a charm and beauty enriched sample will be explained. In section 5.3.2 an alternative technique based on the categorisation of deep inelastic scattering events according to the absolute value of the impact parameter of jet-associated tracks and the subsequent mirroring and subtracting of the signed impact parameter distribution will be illustrated. Subsequently, the technical details of the combination of secondary vertex and tracking information used for the final measurement will be explained in section 5.3.3.

5.3.1 Secondary Vertexing Technique

In inclusive measurements at ZEUS the heavy quark content is usually extracted using the decay length significance and the secondary vertex mass [134–137]. The 2D decay length is calculated as the distance between the beam spot and the secondary vertex in the $x - y$ plane, and subsequently projected onto the axis of the associated jet. The negative part of the significance distribution is then projected onto and subtracted from the positive part, leaving a mirrored significance distribution. The mirrored decay length significance distribution is plotted in bins of the secondary vertex mass to increase the distinguishing power between charm and beauty quarks. Finally, a binned least χ^2 fit of the MC template to the data sample is performed in order to extract the heavy quark content of the data sample.

Secondary Vertex Reconstruction

After the event selection an algorithm was applied in order to search for secondary vertices associated to jets that were reconstructed with the k_T clustering algorithm [105] and passed the jet selection criteria given in section 5.2. A track was associated to the closest jet if the track was within a cone of radius 1 in the $\eta - \phi$ plane:

$$\Delta\mathrm{R} = \sqrt{\Delta\eta^2 + \Delta\phi^2} < 1, \tag{5.2}$$

where $\Delta\eta = \Delta\eta_{\mathrm{trk}} - \Delta\eta_{\mathrm{jet}}$ and $\Delta\phi = \Delta\phi_{\mathrm{trk}} - \Delta\phi_{\mathrm{jet}}$ are defined as the distance between the track and the jet axis. Furthermore, only tracks passing the following selection cuts were considered:

- $p_{\mathrm{T}} > 0.5$ GeV,
- # hits in MVD ≥ 4.

In the case when at least two tracks passed these selection criteria a secondary vertex was fitted using a DAF [100] without beamspot constraint. The imposed track selection cuts provide an impact parameter resolution of jet-associated tracks:

$$\frac{\sigma_\delta}{\delta} = 46\,\mu\mathrm{m} + \frac{122\,\mu\mathrm{m}}{\mathrm{p_T\,[GeV]}}. \tag{5.3}$$

The cut on the transverse momentum reduced the amount of multiple scattering. The requirement of at least four hits in the MVD assured that there was enough spatial information close to the interaction point.
The secondary vertex fit returned the position of the vertex and its covariance matrix. For the calculation of the invariant mass m_{vtx} of the secondary vertices the charged pion mass was assumed for all tracks. After all secondary vertices in an event were reconstructed the remaining tracks in an event were utilised as input for the fit of a reduced primary vertex with beamspot constraint.
In order to optimise the selection of secondary vertices related to heavy flavoured hadron decays [134] the following selection criteria were applied:

- $\mathrm{d_{xy}} < 1\,\mathrm{cm}$, a distance between the beamspot and the secondary vertex smaller than 1 cm in the $x-y$ plane was required to suppress background from long-lived light flavour events, photon conversions and hadronic interactions in the beam pipe and detector material.
- $\chi^2/n_{\mathrm{dof}} < 6$, assuring that a vertex has been reconstructed from jet-associated tracks. Here n_{dof} denotes the number of degrees of freedom in the vertex fit.
- a secondary vertex mass in the range 1 GeV $< m_{\mathrm{vtx}} <$ 6 GeV. This requirement rejects background from long-lived light flavoured hadrons, in particular from K^0_S decays.
- $|Z_{\mathrm{secvtx}}| < 30$ cm, a condition assuring a reasonable MVD and CTD acceptance for tracks belonging to the vertex.

The secondary vertex mass, m_{vtx}, the number of tracks, $\mathrm{N_{vtx}}$, associated to the vertex and the fit quality, χ^2/n_{dof}, of the vertices after the DIS and secondary vertex selection are shown in figure 5.1. Generally, there is a reasonable agreement between data and MC, albeit with some differences for low values of χ^2/n_{dof}. On the other hand, this difference does not affect the present analysis, since the cut on the quality of the secondary vertex fit has been chosen well away from this region. In figure 5.2 the transverse energy, E_T^{jet}, pseudorapidity, η^{jet}, and the azimuthal angle, ϕ^{jet}, of the reconstructed jets after DIS, secondary vertex and

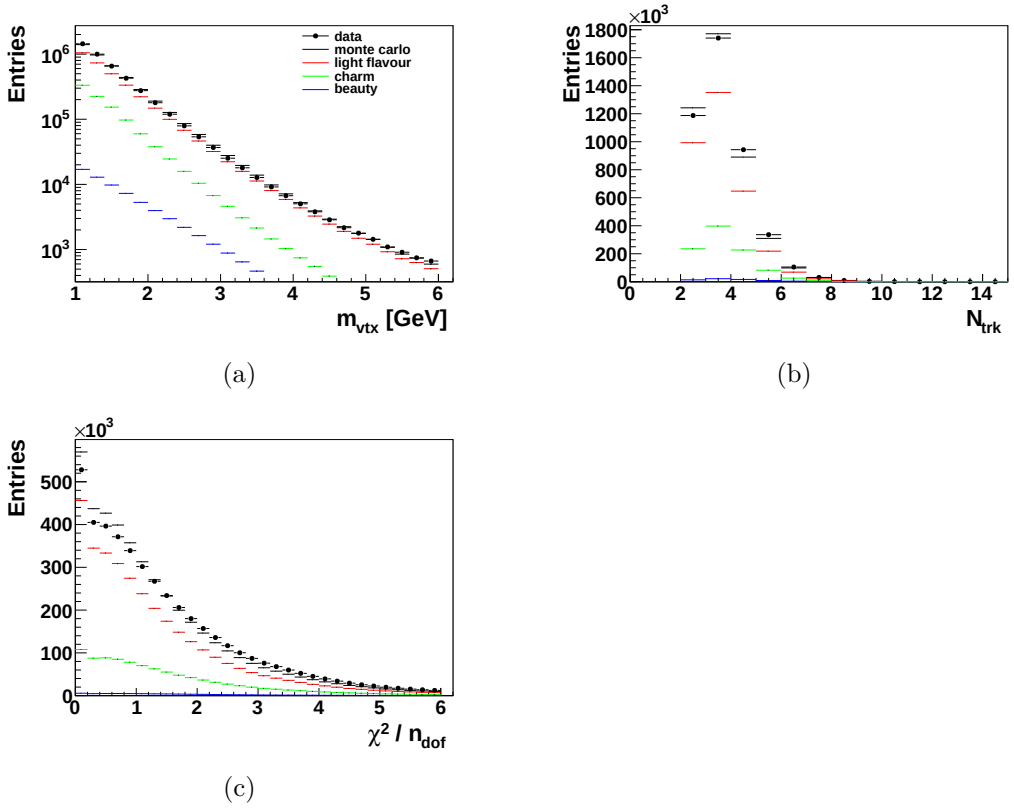

Figure 5.1: The secondary vertex variables (a) m_{vtx} , (b) $\mathrm{N_{trk}}$ and (c) χ^2/n_{dof} after the DIS and secondary vertex selection. The MC samples were normalised to the luminosity of the data and scaled with the k-factors from the binned least χ^2 fit using equation 5.7. The data (black dots) are compared to the sum of the Monte Carlo samples, as well as the light flavour, charm and beauty contributions.

jet selection are shown. The comparison between data and MC is particularly good for the transverse energy distribution. The discrepancy between data and MC simulation in the forward region of the pseudorapidity distribution can be explained due to the intersection between BCAL and FCAL, which affects the reconstruction of EFOs in this kinematic region.

Signal Extraction

For the secondary vertexing analysis, the heavy quark content of the data sample was extracted using the decay length of heavy flavoured hadrons [134, 135]. The decay length was calculated as the distance between the secondary vertex and the beamspot in the $x-y$ plane. The beamspot was used instead of the reduced primary vertex, since it was less biased with secondary vertex tracks, originating from additional heavy quark decays [137].

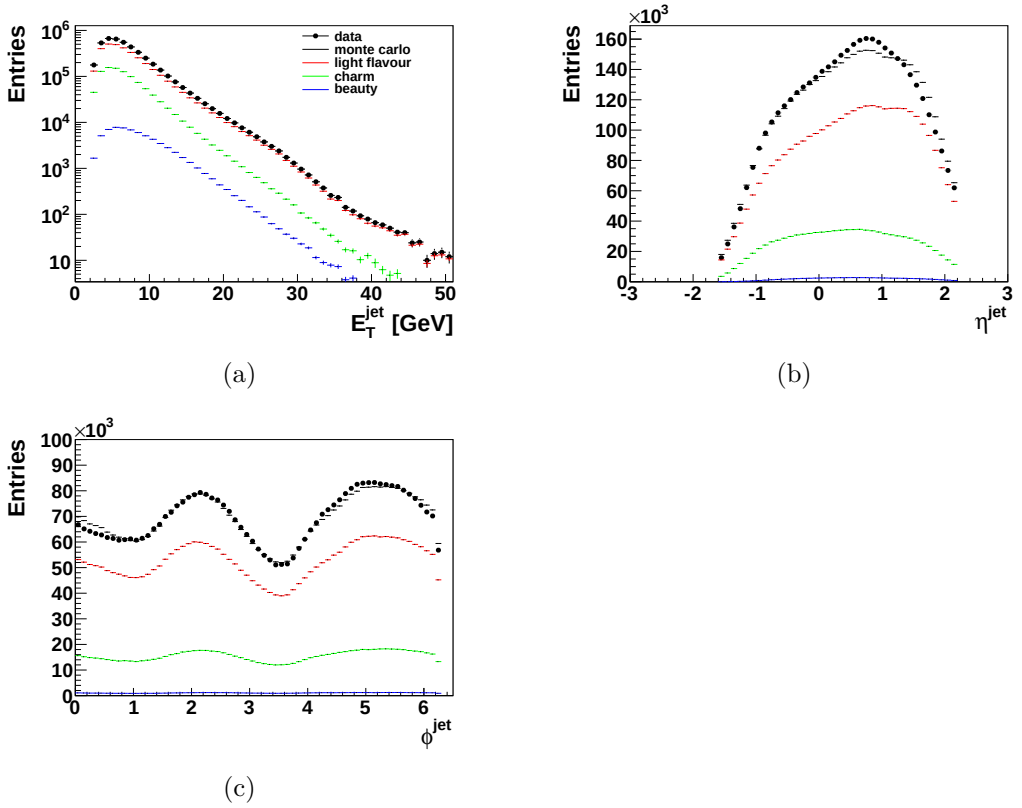

Figure 5.2: The jet variables (a) E_T^{jet}, (b) η^{jet} and (c) ϕ^{jet} after the DIS, secondary vertex and jet selection. The MC samples were normalised to the luminosity of the data and scaled with the k-factors from the binned least χ^2 fit using equation 5.7. The data (black dots) are compared to the sum of all Monte Carlo samples, as well as the light flavour, charm and beauty contributions.

The sign of the decay length was assigned using the axis of the associated jet. If the decay length, $\vec{d}$, was in the same hemisphere as the jet, $\vec{j}$, i.e. $\vec{j} \cdot \vec{d} > 0$, a positive sign was assigned; otherwise the sign was negative. The two-dimensional decay length was then projected onto the jet axis:

$$d_{xy} = \vec{d} \cdot \frac{\vec{j}}{|\vec{j}|} = \begin{pmatrix} X_{\text{vtx}} - X_{\text{bspt}} \\ Y_{\text{vtx}} - Y_{\text{bspt}} \end{pmatrix} \cdot \frac{\vec{j}}{|\vec{j}|}. \tag{5.4}$$

The 2D signed and projected decay length, d_{xy}, in the secondary vertex mass range, $1 < m_{\text{vtx}} < 6$ GeV, is shown in figure 5.3. In a detector with perfect track reconstruction the sign convention would result in a strictly positive decay length distribution for the heavy flavoured hadrons, while half of the combinatorial background would have a negative sign. In a real detector with finite resolution the heavy flavoured decays are partly smeared into the negative region.
The error on the decay length, $\sigma(d_{xy})$, contains information about the detector resolution and depends on the uncertainties of the secondary vertex position and

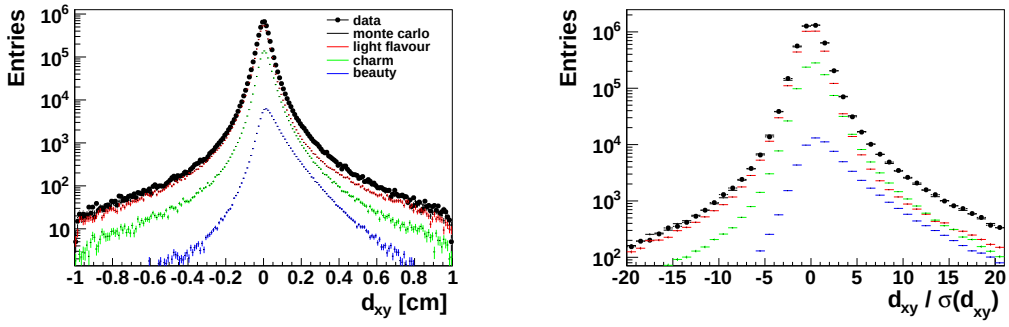

(a) (b)

Figure 5.3: The 2D signed and projected decay length, d_{xy}, and decay length significance, $S_{\text{vtx}} = \sigma(d_{xy})/d_{xy}$, within the secondary vertex mass range $1 < m_{\text{vtx}} < 6$ GeV. The MC samples were normalised to the luminosity of the data and scaled with the k-factors from the binned least χ^2 fit using equation 5.7.

the beamspot width:

$$\sigma(d_{xy}) = \sqrt{\hat{j} \cdot (C_{\text{vtx}} + C_{\text{bspt}}) \cdot \hat{j}}, \tag{5.5}$$

where $\hat{j} = \vec{j}/|\vec{j}|$ denotes the normalised jet momentum vector and C_{vtx} and C_{bspt} are the covariance matrices of the secondary vertex and the beamspot, respectively. The covariance matrix C_{vtx} of the secondary vertex was obtained from the fit and provided information on the uncertainty on the coordinates of the secondary vertex position and their correlations. The diagonal elements of the covariance matrix C_{bspt} of the beamspot are given by the squared beamspot widths in the x and y directions, while the non-diagonal elements were set to zero.

In order to enhance the separation power between the heavy flavoured hadron decays and the light flavoured background the decay length significance is defined as:

$$S_{\text{vtx}} = \frac{d_{xy}}{\sigma(d_{xy})}. \tag{5.6}$$

The signed decay length significance distribution in the secondary vertex mass range, $1 < m_{\text{vtx}} < 6$ GeV, is shown is figure 5.3. The distribution comprises a large asymmetry towards positive significance values for heavy flavoured hadron decays, while it behaves predominantly symmetric for light flavours.

In order to utilise the decay length significance, S, as the distinguishing variable between light and heavy flavour decays the negative part of the significance distribution ($S_{\text{vtx}} < 0$) is mirrored onto and subtracted from the positive part ($S_{\text{vtx}} > 0$). Provided that the decay length distribution for light flavoured decays behaves mostly symmetrically, the light flavour contribution is minimised in the subtraction procedure, while the heavy quark contribution is enriched. In order

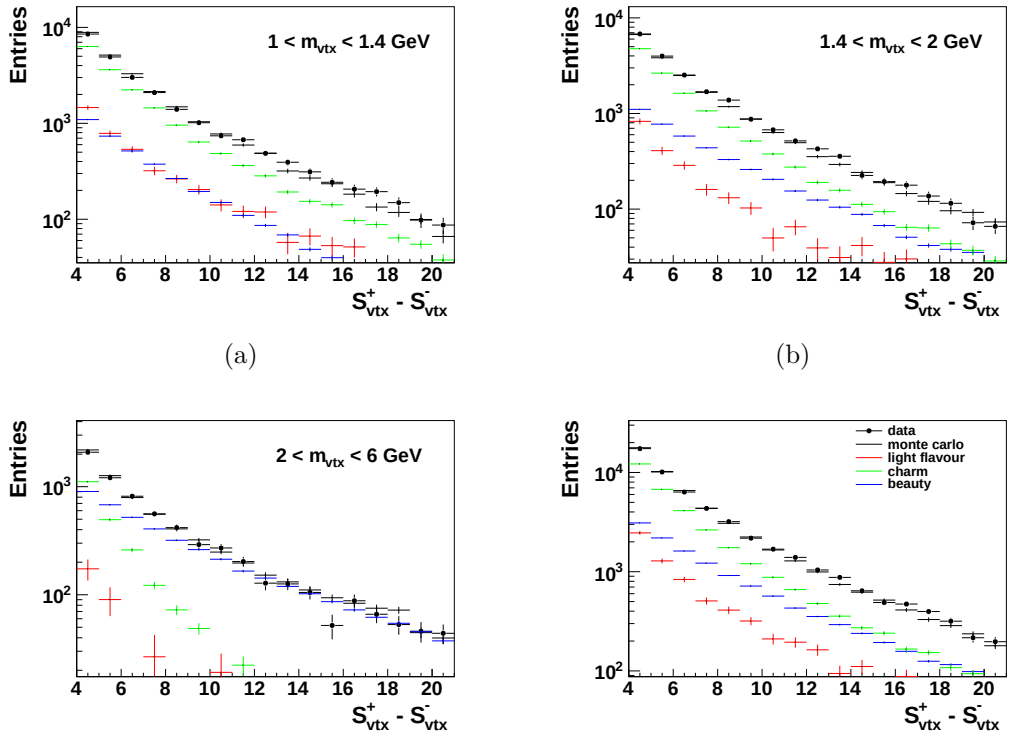

Figure 5.4: The mirrored and subtracted decay length significance distribution, $S^{+}_{\mathrm{vtx}} - S^{-}_{\mathrm{vtx}}$, in three different bins of the secondary vertex mass, m_{vtx}, (a) $1 < m_{\mathrm{vtx}} < 1.4$ GeV, (b) $1.4 < m_{\mathrm{vtx}} < 2$ GeV, (c) $2 < m_{\mathrm{vtx}} < 6$ GeV, and (d) the inclusive bin for the considered secondary vertex mass range $1 < m_{\mathrm{vtx}} < 6$ GeV. The MC samples were normalised to the luminosity of the data and scaled with the k-factors from the binned least χ^2 fit using equation 5.7.

to further enhance the distinguishing power between charm and beauty decays the mirrored significance distributions were analysed in terms of three different secondary vertex mass bins:

$$\begin{aligned} 1\ \mathrm{GeV} < m_{\mathrm{vtx}} < 1.4\ \mathrm{GeV}, \\ 1.4\ \mathrm{GeV} < m_{\mathrm{vtx}} < 2\ \mathrm{GeV}, \\ 2\ \mathrm{GeV} < m_{\mathrm{vtx}} < 6\ \mathrm{GeV}. \end{aligned}$$

The mirrored decay length significance distribution, S_{vtx}, plotted in three different bins of the secondary vertex mass is shown in figure 5.4. The analysis yields a charm enriched sample for the secondary vertex mass range, $1 < m_{\mathrm{vtx}} < 1.4$ GeV, a charm and beauty enriched sample for $1.4 < m_{\mathrm{vtx}} < 2$ GeV, and a beauty enriched sample for $2 < m_{\mathrm{vtx}} < 6$ GeV. These charm and beauty enriched significance distributions have subsequently been used to extract the heavy quark

content of the data sample.
In order to extract the signal, a binned, least χ^2 fit of the mirrored and subtracted significance distributions of the MC templates was performed to the data sample simultaneously for all three secondary vertex mass bins. The following fit function was minimised:

$$\chi^2 = \sum_i \frac{(N_i^d - k_b\, N_i^b - k_c\, N_i^c - k_{lf}\, N_i^{lf})^2}{(\sigma_i^d)^2 + (k_b\, \sigma_i^b)^2 + (k_c\, \sigma_i^c)^2 + (k_{lf}\, \sigma_i^{lf})^2} + \frac{(N_{tot}^d - k_b\, N_{tot}^b - k_c\, N_{tot}^c - k_{lf}\, N_{tot}^{lf})^2}{(\sigma_{tot}^d)^2 + (k_b\, \sigma_{tot}^b)^2 + (k_c\, \sigma_{tot}^c)^2 + (k_{lf}\, \sigma_{tot}^{lf})^2}, \tag{5.7}$$

where the sum runs over all bins i of the three fitted $S_{\mathrm{vtx}}^+ - S_{\mathrm{vtx}}^-$ distributions, and the requirement $|S| > 4$ was imposed to avoid unphysical effects in the signal extraction [134, 135]. N_i^d, N_i^b, N_i^c and N_i^{lf} denote the entries and σ_i^d, σ_i^b, σ_i^c and σ_i^{lf} the statistical uncertainties in a given bin i of the mirrored and subtracted significance distributions. N_{tot}^d, N_{tot}^b, N_{tot}^c and N_{tot}^{lf} denote the total number of entries and σ_{tot}^d, σ_{tot}^b, σ_{tot}^c and σ_{tot}^{lf} the statistical uncertainties in the unmirrored decay length significance distributions. All MC samples were normalised to the luminosity of the data before the least χ^2 fit was performed and the normalisation of the MC templates in the fit was constrained using the integral over the entries in the unmirrored decay length significance distributions.
The least χ^2 fit returned the k-factors k_b, k_c and k_{lf}, which represent scaling factors for the beauty, charm and light flavour templates in order to obtain an optimised description of the data. The following scaling factors were extracted for the full kinematic region of the measurement:

$$k_{lf} = 0.947 \pm 0.004 \tag{5.8}$$

$$k_b = 1.598 \pm 0.056 \tag{5.9}$$

$$k_c = 1.302 \pm 0.021 \tag{5.10}$$

The fit quality of $\chi^2/n_{dof} = 22.61/19 = 1.19$ was reasonable and the quoted uncertainties are the statistical errors yielded by the least χ^2 fit.

Corrections

In order to obtain a satisfactory description of the data by the MC several corrections had to be applied. These corrections include a smearing of the 2D decay length, d_{xy}, applied to all MC templates, a reweighting of the Ariadne MC in E_T^{jet} and a reweighting of the Rapgap MC in Q^2. The technical details of these corrections are explained in the following sections.

Decay Length Smearing

The decay length significance distribution from the latest version of the reconstruction is not fully described by the MC. In order to compensate for the difference between data and Monte Carlo, the following smearing functions have been applied to all MC templates [134, 135]:

- for 5 % of all vertices the projected decay length was smeared by a Gaussian of width $1.8 \cdot \sigma(d_{xy})$.
- for 1 % of all vertices the projected decay length was smeared by a Gaussian of width $2.3 \cdot \sigma(d_{xy})$.
- the decay length, d_{xy}, of a vertex fulfilling $0.1 \cdot \sigma(d_{xy}) < \mathrm{ran}_1$ was smeared with the following function to adjust the extreme tails:

$$d_{xy} = d_{xy} + \frac{\mathrm{ran}_2}{|\mathrm{ran}_2|} \cdot \frac{\ln(1 - |\mathrm{ran}_2|)}{-5.0}, \tag{5.11}$$

  where ran_1 is a random number, uniformly distributed in the range $[0, 1]$, and ran_2 is a random number in the range $[-1, 1]$.

Reweighting of the Ariadne MC in E_T^{jet}

In the kinematic region considered in the present analysis, the Ariadne MC overestimates the production of jets at high transverse energy, E_T^{jet}. This feature was corrected for by reweighting the Ariadne MC in E_T^{jet} [134, 135]. The impact of the smearing on the charm and beauty cross sections was negligible, since the reweighting affected exclusively the light flavour content.

Reweighting of the Rapgap MC in Q^2

The measured distributions in Q^2 fall more steeply than predicted by the Rapgap MC [134] for the heavy flavours. In order to ensure that the acceptance corrections were reasonable the Rapgap MC sample was reweighted for charm and beauty with the following functions [134, 135]:

$$w_b = e^{-0.599 - 0.00389 \cdot Q^2} + 0.631, \tag{5.12}$$

$$w_c = e^{-0.486 - 0.0158 \cdot Q^2} + 0.781. \tag{5.13}$$

The systematic uncertainty related to this reweighting procedure was estimated by varying the correction by $\pm 50\%$.

5.3.2 Impact Parameter Technique

An alternative approach to extract the heavy quark content of the data sample is based on the impact parameter of jet-associated tracks [58, 59]. The impact parameter is calculated as the distance between the point of closest approach (pca) and the beam spot in the $x - y$ plane. A positive or negative sign is assigned, as shown in figure 5.5, depending on the angle between the vector joining the point of closest approach and the beam spot and the axis of the associated jet. After the application of basic track selection criteria the impact parameter significance of jet-associated tracks is used to categorise DIS events. The signed impact parameter significance is plotted for each category of events, and the negative part of the distributions is projected onto and subtracted from the positive part, giving rise to mirrored track significance distributions. Finally, a binned least χ^2 fit of the MC templates to the data sample is performed in order to extract the heavy quark content of the data sample.

Impact Parameter Reconstruction

After the event selection as in section 5.3.1 a further track selection was applied in order to select well-reconstructed tracks in the immediate vicinity of the interaction region. The algorithm considered only tracks associated to jets that were reconstructed with the k_T clustering algorithm [105] and passed the jet selection criteria given in section 5.2. A track was associated to the closest jet if the track was within a cone of radius 1 in the $\eta - \phi$ plane:

$$\Delta\mathrm{R} = \sqrt{\Delta\eta^2 + \Delta\phi^2} < 1, \tag{5.14}$$

where $\Delta\eta = \Delta\eta_{\mathrm{trk}} - \Delta\eta_{\mathrm{jet}}$ and $\Delta\phi = \Delta\phi_{\mathrm{trk}} - \Delta\phi_{\mathrm{jet}}$ are defined as the distance between the track and the jet axis. Furthermore, only tracks passing the following selection cuts were considered:

- $p_{\mathrm{T}} > 0.5$ GeV,
- # hits in MVD ≥ 4,
- $|\delta| < 1\,\mathrm{mm}$.

The first two cuts assured a sufficient track quality in the immediate vicinity of the interaction region, i.e. a sufficient resolution of the combined CTD and MVD track reconstruction algorithm (see equation 5.3). The cut on the impact parameter δ of jet-associated tracks rejected decays from long-lived strange particles like Λ^0 and K_s^0 [60, 138].
The impact parameter δ of jet-associated tracks is calculated as the distance between the beam spot and the point of closest approach (pca) in the $x - y$ plane

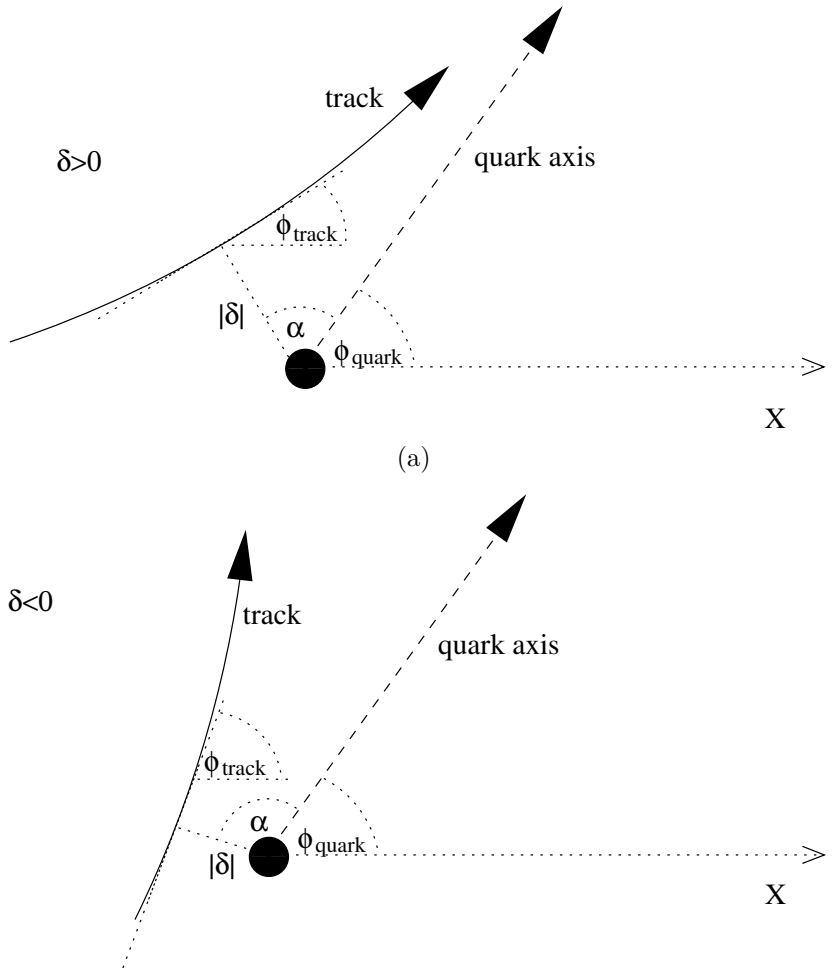

Figure 5.5: Diagram of a jet-associated track and illustration of the associated signed 2D track impact parameter.

[58, 59]. The direction of the struck quark is used to determine the sign of the impact parameter, as illustrated in figure 5.5. If the angle α between the line joining the beam spot to the point of closest approach and the axis of the associated jet is smaller than 90°, δ will be defined as positive. Otherwise the track impact parameter δ will be assigned a negative sign. Tracks with an azimuthal angle ϕ outside $\pm 90°$ from the jet axis are rejected, since they are not considered to be associated to the struck quark.
Figure 5.6 shows the (signed) 2D impact parameter of jet-associated tracks. The absolute value of the impact parameter is provided by the latest version of the reconstruction, and reveals a discrepancy in the data to MC comparison. The agreement is more satisfactory for the signed 2D impact parameter, which has been smeared with a phenomenological function as will be explained. In a detec-

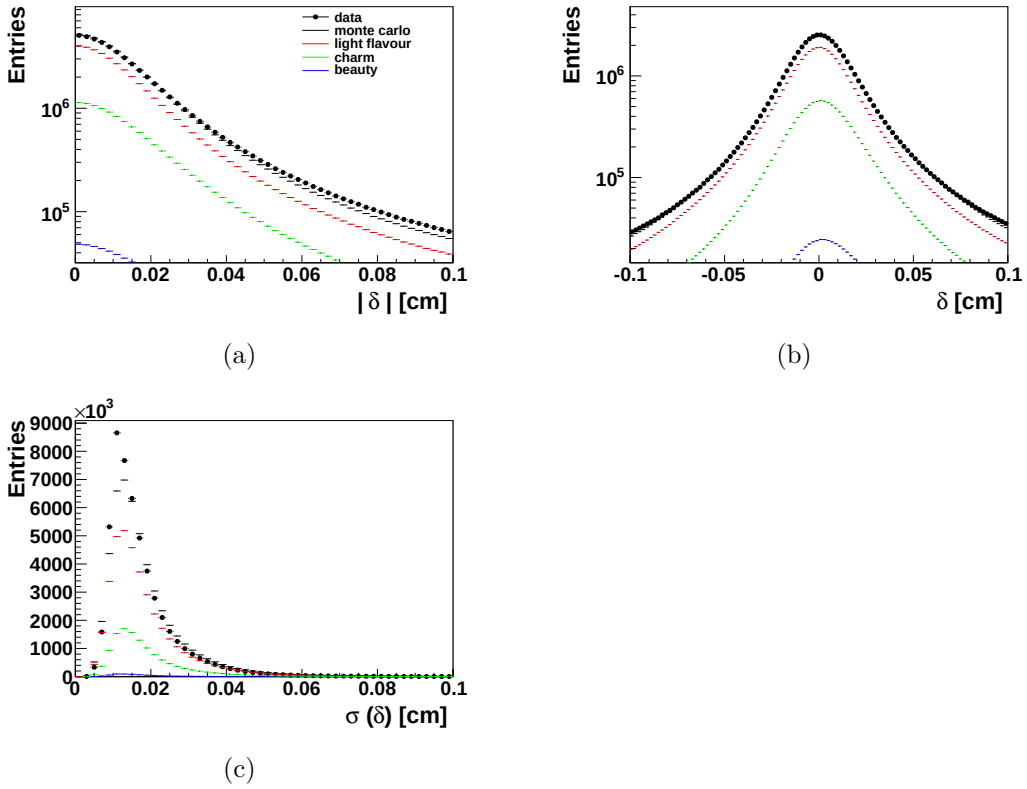

Figure 5.6: The tracking variables (a) 2D impact parameter, (b) signed 2D impact parameter and (c) impact parameter error of jet-associated tracks. The data are compared with the sum of the MC samples, and the individual contributions are shown as points. The MC templates were normalised to the luminosity of the data and scaled with the k-factors obtained from the inclusive tracking analysis.

tor with perfect resolution the impact parameter of tracks originating from heavy flavoured hadrons would be predominantly positive, while half of the tracks originating from the light flavoured background would be assigned a negative sign. However, due to finite detector resolution the light flavoured tracks exhibit an asymmetry towards positive values and the heavy flavoured tracks are partly smeared out into the negative region [58, 59]. As a consequence the heavy flavour content is not sufficiently enriched for the signal extraction after the negative part of the track impact parameter distribution has been projected onto and subtracted from the positive side.
As the detector resolution is limited one will therefore have to consider the signed track impact parameter significance for the signal extraction to enhance the heavy flavour asymmetry and develop a more sophisticated technique of track selection to obtain a sufficient charm and beauty enrichment and separation. In order to enhance the asymmetry for tracks originating from heavy flavoured hadrons one

defines the signed track impact parameter significance S_{trk}:

$$S_{\mathrm{trk}} = \frac{\delta}{\sigma_\delta}, \tag{5.15}$$

where δ is the signed track impact parameter and σ_δ is the error on the impact parameter δ. The error σ_δ is calculated using:

$$\sigma_\delta^2 = \begin{pmatrix} u_x & u_y \end{pmatrix} \Big(C_{\mathrm{pca}} + C_{\mathrm{bsp}} \Big) \begin{pmatrix} u_x \\ u_y \end{pmatrix}, \tag{5.16}$$

where $\begin{pmatrix} u_x & u_y \end{pmatrix}$ is a unit vector from the beam spot to the point of closest approach, C_{pca} is the covariance matrix of the point of closest approach and C_{bsp} is the covariance matrix of the beam spot.
The covariance matrix C_{pca} is calculated from the 5×5 covariance matrix C_{trk} of the track parameters, which are propagated to a 3×3 matrix C'_{pca} for the pca parameters. The propagation is performed using the following transformation:

$$C'_{\mathrm{pca}} = M^T C_{\mathrm{trk}} M, \tag{5.17}$$

where M is the transformation matrix:

$$M = \begin{pmatrix} \frac{\partial x}{\partial \phi_0} & \frac{\partial y}{\partial \phi_0} & \frac{\partial z}{\partial \phi_0} \\ \frac{\partial x}{\partial W} & \frac{\partial y}{\partial W} & \frac{\partial z}{\partial W} \\ \frac{\partial x}{\partial D_0} & \frac{\partial y}{\partial D_0} & \frac{\partial z}{\partial D_0} \\ \frac{\partial x}{\partial Z_0} & \frac{\partial y}{\partial Z_0} & \frac{\partial z}{\partial Z_0} \\ \frac{\partial x}{\partial T} & \frac{\partial y}{\partial T} & \frac{\partial z}{\partial T} \end{pmatrix}. \tag{5.18}$$

An explicit calculation of the partial derivatives shows that the matrix M can be written in block diagonal form:

$$M = \begin{pmatrix} M' & 0 \\ 0 & M'' \end{pmatrix}, \tag{5.19}$$

where the 3×2 matrix M' takes the following simplified form provided that the beam spot is used as reference point:

$$M' = \begin{pmatrix} D_0 \cos(\phi_0) & D_0 \sin(\phi_0) \\ 0 & 0 \\ \sin(\phi_0) & -\cos(\phi_0) \end{pmatrix}. \tag{5.20}$$

The 2×2 covariance matrix C_{pca} of the point of closest approach can then be obtained from the following relation:

$$C_{\mathrm{pca}} = M'^T \, C' \, M', \tag{5.21}$$

where the matrix C' is the upper left 3×3 part of the matrix C'_{pca} which we have obtained after propagating the 5×5 covariance matrix C_{trk} of the track helix

parameters to the parameters of the point of closest approach.
Figure 5.6 shows the impact parameter error of jet-associated tracks revealing a difference in the data to MC comparison. The difference originates from difficulties to simulate the beam slope corrections, which originate from slopes of the beams in the x- and y-directions with respect to the z-axis, in the MC simulation. However, it does not affect the present analysis, since the signal extraction is based on the impact parameter significance, and a conservative cut has been applied to exclude events that have been shifted towards lower significance values.

Signal Extraction

The signed track impact parameter significance, S_{trk}, as defined in equation 5.15 is subsequently used to categorise DIS events [60, 138]. After the track selection criteria have been applied the impact parameter significance of all remaining jet-associated tracks is calculated, and the tracks are ordered according to the absolute value of the track significance. The jet-associated tracks are then stored according to the following categorisation:

- In events with one remaining jet-associated track the signed impact parameter significance is stored in one histogram.
- In events with two remaining jet-associated tracks the signed impact parameter significance of the track with the second highest absolute significance is stored in a separate histogram.
- In events with three or more remaining jet-associated tracks the track significance of the three tracks with the highest absolute impact parameter significance are stored in three separate histograms.

In events, in which more than one track has passed the track selection criteria, only tracks having the same sign as the track with the highest absolute track significance have been considered.
One can observe that the signed impact parameter significance distributions for tracks originating from heavy flavoured hadron decays, as shown in figures 5.7 and 5.8, display a larger asymmetry than the signed impact parameter distribution shown in figure 5.6. At the same time the signed impact parameter significance distributions remain fairly symmetric for tracks originating from light flavoured hadrons, which minimises the light flavour background using the technique of mirroring and subtraction. The negative part, S^{-}_{trk}, of the signed impact parameter significance distributions is subsequently projected onto and subtracted from the positive part, S^{+}_{trk}, giving rise to mirrored track significance distributions. One observes that the technique of mirroring and subtracting the signed impact parameter significance distributions, as shown in figures 5.7 and 5.8, yields charm

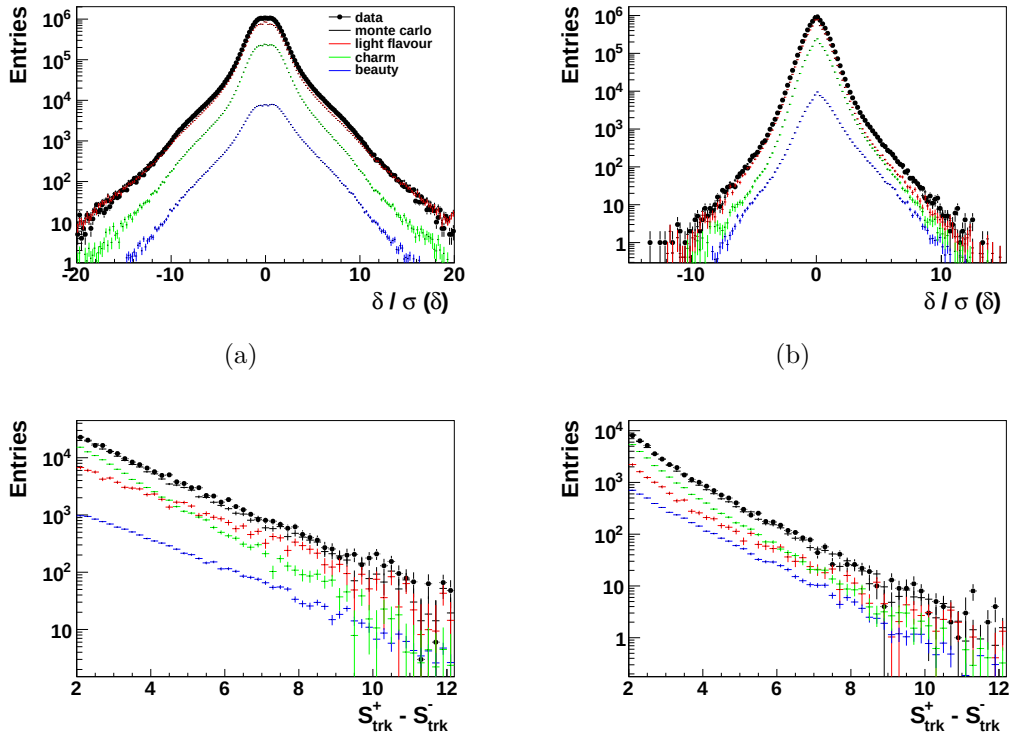

Figure 5.7: The signed impact parameter significance for (a) the one-track scenario, (b) the two-track scenario and the mirrored and subtracted impact parameter significance for (c) the one-track scenario, (d) the two-track scenario of jet-associated tracks. The data are compared with the sum of the MC samples, as well as the light flavour, charm and beauty contributions. The MC templates were normalised to the luminosity of the data and scaled with the k-factors obtained from the inclusive tracking analysis.

enriched samples for the one and two track scenarios, while one obtains (a) and (b) charm enriched and (c) beauty enriched samples, as shown in figure 5.9, for the three or more track scenario.
In order to extract the heavy quark content a binned least χ^2 fit of the MC templates to the data sample is performed for all five mirrored and subtracted impact parameter significance distributions. In analogy to the secondary vertexing technique, the fit function from equation 5.7 needs to be minimised, where the sum runs over all bins i of the five mirrored and subtracted track significance distributions. The requirement $|S_{trk}| > 2$ was imposed for the mirrored track significance distributions of the one and two track scenario, while the condition $|S_{trk}| > 3$ was imposed for the three or more track scenario [58–60, 138]. In the context of the impact parameter based technique N_i^d, N_i^b, N_i^c and N_i^{lf} denote the entries and σ_i^d, σ_i^b, σ_i^c and σ_i^{lf} the statistical uncertainties in a given bin i of the mirrored and subtracted impact parameter significance distributions. On the

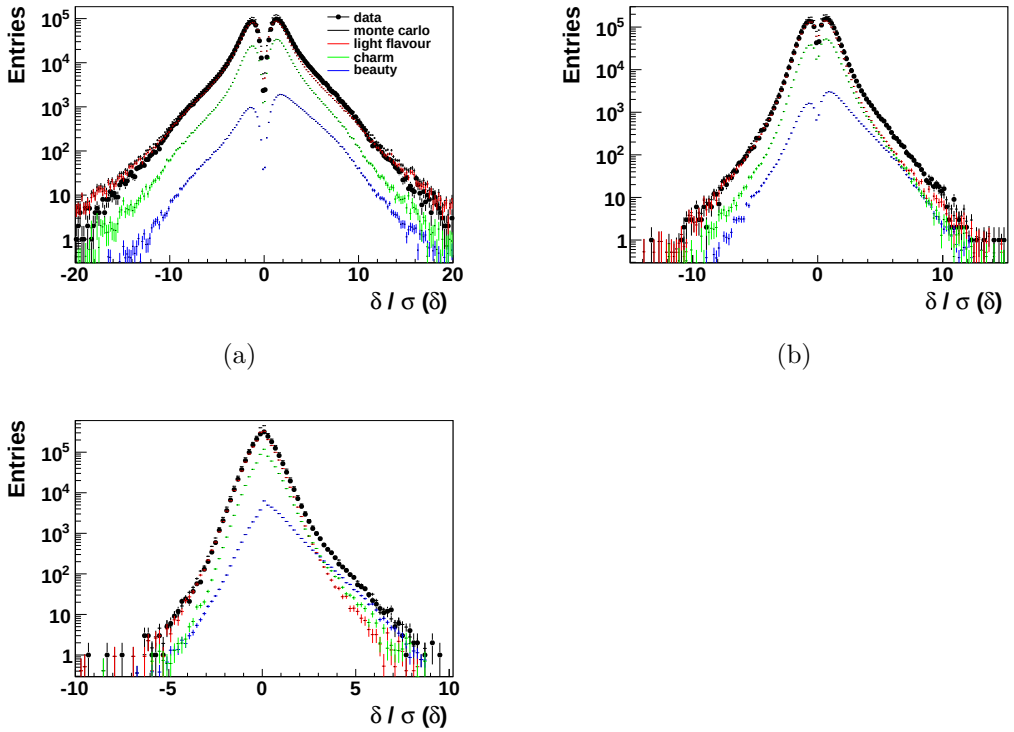

Figure 5.8: The signed impact parameter significance of the track with the (a) highest (b) second highest and (c) third highest absolute track significance value of jet-associated tracks for the three or more tracks scenario. The data are compared with the sum of the MC samples, as well as the light flavour, charm and beauty contributions. The MC templates were normalised to the luminosity of the data and scaled with the k-factors obtained from the inclusive tracking analysis.

other hand, N^d_{tot}, N^b_{tot}, N^c_{tot} and N^{lf}_{tot} denote the total number of entries and σ^d_{tot}, σ^b_{tot}, σ^c_{tot} and σ^{lf}_{tot} the statistical uncertainties in the unmirrored signed impact parameter significance distributions. All MC samples were normalised to the luminosity of the data before the least χ^2 fit was performed and the normalisation of the MC templates in the fit was constrained using the integral over the entries in the signed impact parameter significance distributions.
In analogy to the secondary vertexing analysis, the least χ^2 fit returns the k-factors k_b, k_c and k_{lf}, which represent scaling factors for the beauty, charm and light flavour templates appropriate for an optimised description of the data. The following scaling factors were extracted for the full kinematic region of the mea-

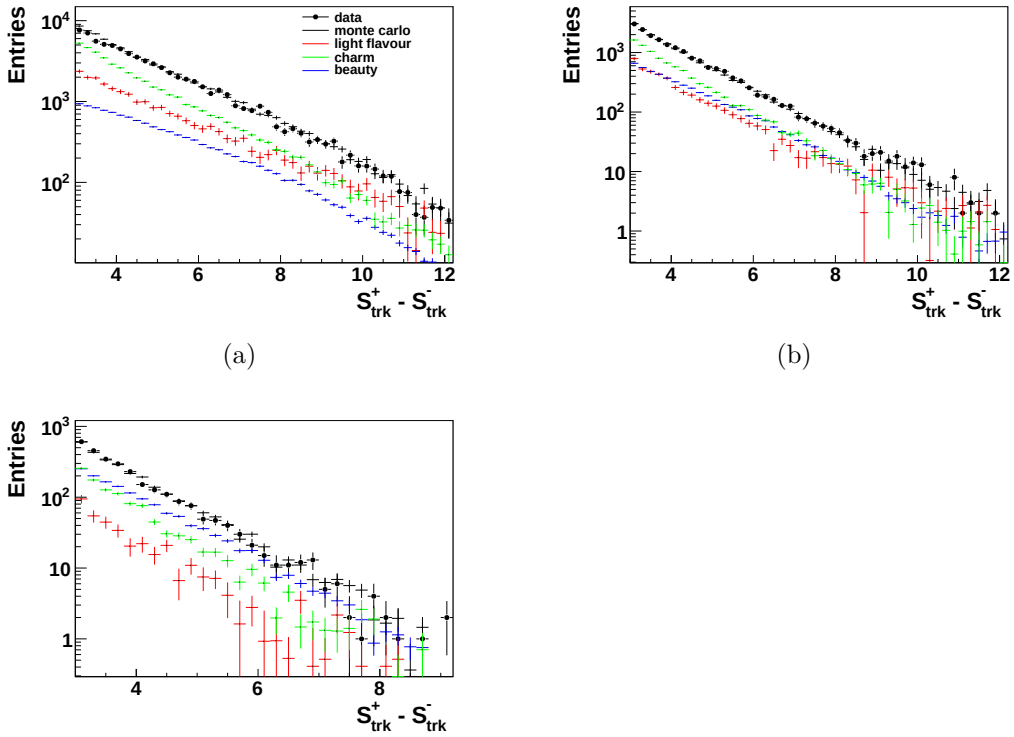

Figure 5.9: The mirrored and subtracted impact parameter significance of the track with the (a) highest (b) second highest and (c) third highest absolute track significance value of jet-associated tracks for the three or more track scenario. The data are compared with the sum of the MC samples, as well as the light flavour, charm and beauty contributions. The MC templates were normalised to the luminosity of the data and scaled with the k-factors obtained from the inclusive tracking analysis.

surement:

$$k_{lf} = 1.050 \pm 0.004 \tag{5.22}$$

$$k_b = 1.629 \pm 0.064 \tag{5.23}$$

$$k_c = 1.314 \pm 0.019 \tag{5.24}$$

The obtained heavy flavour k-factors are compatible with the values obtained from the secondary vertexing analysis and comprise comparable errors, whilst the light flavour k-factor changes by many sigma. The fit quality of $\chi^2/n_{dof} = 26.60/19 = 1.40$ was reasonable, and the quoted uncertainties are the statistical errors provided by the least χ^2 fit. The error of the scaling factor for the light flavour sample appears to be small compared to the relative errors of the heavy flavour samples. This characteristic is a feature of the normalisation of the light flavour sample to the total number of entries in the unmirrored track significance distribution. At the same time the scaling factor of the light flavour sample

is significantly above the value obtained from the secondary vertexing analysis. This is not a physical effect though, since the cut on the secondary vertex mass applied in the secondary vertex analysis rejects light flavour background, which is subsequently accumulated in the tracking analysis.

Corrections

In order to obtain a satisfactory description of the data by the MC simulation several corrections had to be applied. The corrections consisted of the smearing of the signed impact parameter of jet-associated tracks with a Gaussian to account for the discrepancy in the core of the distribution and an exponential function to adjust the tails.

Impact Parameter Smearing

The impact parameter distribution shown in figure 5.6 (a) is not fully described by the MC simulation. In order to compensate for the difference between data and Monte Carlo, the light flavour content simulated by the Ariadne MC, was smeared with the following distributions:

- for 4 % of all reconstructed tracks the signed impact parameter of jet-associated tracks was smeared by a Gaussian function of the width 1.5 $\cdot\sigma_\delta$ to compensate for the difference in the core of the distribution.

- for 4 % of all reconstructed tracks the signed impact parameter of jet-associated tracks was smeared with the following function to adjust the tails:

$$\delta = \delta + \frac{\text{ran}}{|\text{ran}|} \cdot \frac{\ln(1-\text{ran})}{-50}, \tag{5.25}$$

  where ran is a random number uniformly distributed in $[-1, 1]$.

The results of the smearing are shown in figure 5.6 (b), and yield a satisfactory description of the data. The impact on the measured heavy quark cross sections is evaluated by switching the smearing functions on and off.

5.3.3 Combined Vertexing and Tracking Technique

In the previous sections techniques of heavy flavour tagging based upon the secondary vertex of decaying hadrons [134–137] and the impact parameter of jet-associated tracks [58–60, 138] have been detailed. However, in order to make a

fully inclusive measurement the present analysis applies an algorithm that combines tracking and vertexing information, using independent variables. The combined tracking and vertexing algorithm proceeds in three consecutive steps:

- In the first case when a well-reconstructed secondary vertex is found in a DIS event, the combined algorithm will rely on the decay length significance and secondary vertex mass.
- In the second case when a secondary vertex could not be reconstructed, the signed impact parameter of jet-associated tracks will be used as the basis for the signal extraction.
- In events containing well-reconstructed secondary vertices and jets associated to vertices, which did not pass the secondary vertex selection, the impact parameter of tracks associated to these jets will be used in addition to the vertexing information.

The algorithm is designed to search for secondary vertices in events with at least one well-reconstructed vertex, for jet-associated tracks in events without a well-reconstructed vertex, and to utilise impact parameter and vertexing information in events, in which both, well-reconstructed vertices and jets, are available. The signal extraction is performed in analogy to the previously explained inclusive techniques. The decay length significance is plotted in bins of the secondary vertex mass for each event, while the impact parameter significance of jet-associated tracks is plotted according to the previously defined categorisation. The negative part of the significance distributions is then projected onto and subtracted from the positive part, giving rise to mirrored significance distributions. Finally, a binned least χ^2 fit of the MC templates to the data sample is performed in order to extract the heavy quark content of the data sample.

Signal Extraction

The algorithm that combines secondary vertexing and tracking information extracts the available information in three separate steps. After the event selection the combined algorithm was trained to search for secondary vertices associated to jets that were reconstructed with the k_T clustering algorithm [105] and passed the jet selection criteria given in section 5.2.
In the first step of the algorithm, events were considered if they contained at least one reconstructed secondary vertex that passed these selection criteria. As explained in section 5.3.1 the signed 2D decay length, d_{xy}, was calculated as the distance between the beam spot and the secondary vertex in the $x - y$ plane and subsequently projected onto the axis of the associated jet. To increase the distinguishing power between heavy flavour decays and light flavour background,

the secondary vertex significance, S_{vtx}, was calculated, as defined in equation 5.6. Again, the negative part of the decay length significance distribution was mirrored onto and subtracted from the positive part. The mirrored and subtracted significance distribution, $S^{+}_{\mathrm{vtx}} - S^{-}_{\mathrm{vtx}}$, was finally plotted in three different bins of the secondary vertex mass.
In the second step of the algorithm, events without a well-reconstructed secondary vertex were considered. In these events the signed 2D impact parameter, δ, of jet-associated tracks was calculated as the distance between the beam spot and the point of closest approach in the $x-y$ plane. In order to increase the distinguishing power between tracks originating from heavy flavour decays and those originating from light flavour decays the impact parameter significance, S_{trk}, was calculated, as defined in equation 5.15. The absolute value of the track significance of jet-associated tracks was calculated and the events were subsequently categorised, as explained in section 5.3.2. The negative part of the signed impact parameter significance distribution was subsequently mirrored onto and subtracted from the positive part for the three different scenarios, resulting in mirrored and subtracted, $S^{+}_{\mathrm{trk}} - S^{-}_{\mathrm{trk}}$, track significance distributions.
In the third step of the algorithm events containing a well-reconstructed secondary vertex and a jet associated to a vertex that did not pass the secondary vertex selection were considered. In this case the signed 2D decay length significance, S_{vtx}, of the selected secondary vertex was calculated and subsequently plotted in three different bins of the secondary vertex mass. The negative part of the secondary vertex significance distribution was then mirrored onto and subtracted from the positive part, giving rise to mirrored and subtracted, $S^{+}_{\mathrm{vtx}} - S^{-}_{\mathrm{vtx}}$, decay length significance distributions. Subsequently, the signed 2D impact parameter significance, S_{trk}, of tracks associated to the selected jet was calculated for tracks passing the track selection criteria of the impact parameter based technique. The events were then categorised according to the absolute value of the signed impact parameter significance, and the track significance was plotted for the three different scenarios. Finally, the negative part of the signed track significance distributions was mirrored onto and subtracted from the positive part for the three different scenarios, resulting in mirrored and subtracted, $S^{+}_{\mathrm{trk}} - S^{-}_{\mathrm{trk}}$, track significance distributions.
The algorithm exploits the available information from the impact parameter of jet associated tracks and the decay length of secondary vertices in DIS events whilst avoiding correlations. This allows a fully inclusive measurement of heavy-quark jet cross sections to be made using information that has not been considered previously. In order to extract the heavy quark content of the data sample one performs a binned least χ^2 fit of the MC templates to the data sample with the function to be minimised defined in equation 5.7. The sum runs over all bins i of the mirrored and subtracted impact parameter and secondary vertex significance distributions, whilst the same requirements as in sections 5.3.1 and 5.3.2 were imposed. All MC samples were normalised to the luminosity of the data before

the least χ^2 fit was performed and the normalisation of the MC templates in the fit was constrained using the integral over the entries in the signed impact parameter and decay length significance distributions.
In analogy to the secondary vertexing and impact parameter based techniques the least χ^2 fit returns the k-factors k_b, k_c and k_{lf}, which represent scaling factors for the beauty, charm and light flavour templates appropriate for an optimised description of the data. The following scaling factors were extracted for the full kinematic region of the measurement:

$$k_{lf} = 1.037 \pm 0.003 \tag{5.26}$$

$$k_b = 1.561 \pm 0.050 \tag{5.27}$$

$$k_c = 1.314 \pm 0.015 \tag{5.28}$$

The obtained heavy flavour k-factors are compatible with the values obtained from the inclusive measurements based on the decay length and impact parameter significance of jet-associated tracks. The fit quality of $\chi^2/n_{\mathrm{dof}} = 43.7/38 = 1.15$ was reasonable, and the quoted uncertainties are the statistical errors provided by the least χ^2 fit. In comparison with the previously described techniques the combination of tracking and vertexing information returns a significantly reduced error for the k-factors of the heavy flavours. The statistical error for the scaling factor for charm has reduced from 0.021 to 0.015, yielding a reduction of the relative error of 41 %. The statistical precision of the k-factors for the beauty sample has improved as well, as the statistical uncertainty has reduced from 0.056 to 0.050, representing a reduction of the relative error of 9.4 %.
In the signal region, the fraction of jets tagged using secondary vertexing information and jets tagged using the impact parameter of jet-associated tracks has been found to be 13 % and 87 % respectively. The novel algorithm has consequently increased the tagging efficiency, ϵ, from 12 % to 60 %, the efficiency being defined as

$$\epsilon = \frac{T \cap R}{T}, \tag{5.29}$$

where T is the number of charm events at hadron level, and R is the number of reconstructed charm events. At the same time, the purity, defined as

$$p = \frac{T \cap R}{R}, \tag{5.30}$$

was found to be 91 % for the combined vertexing and tracking analysis, which is comparable with the value of 95 % found for the secondary vertexing analysis alone.

Control Plots

In order to validate the MC samples, predictions from the simulations need to be compared to the data. In this section results from the Rapgap and Ariadne MC

simulations are compared with the data for the most important variables that characterise an event. Figure 5.10 shows control plots after the MC samples were normalised to the luminosity of the data and scaled with the k-factors obtained from the combined tracking and vertexing analysis. In general the agreement between data and MC is reasonable for all event variables.

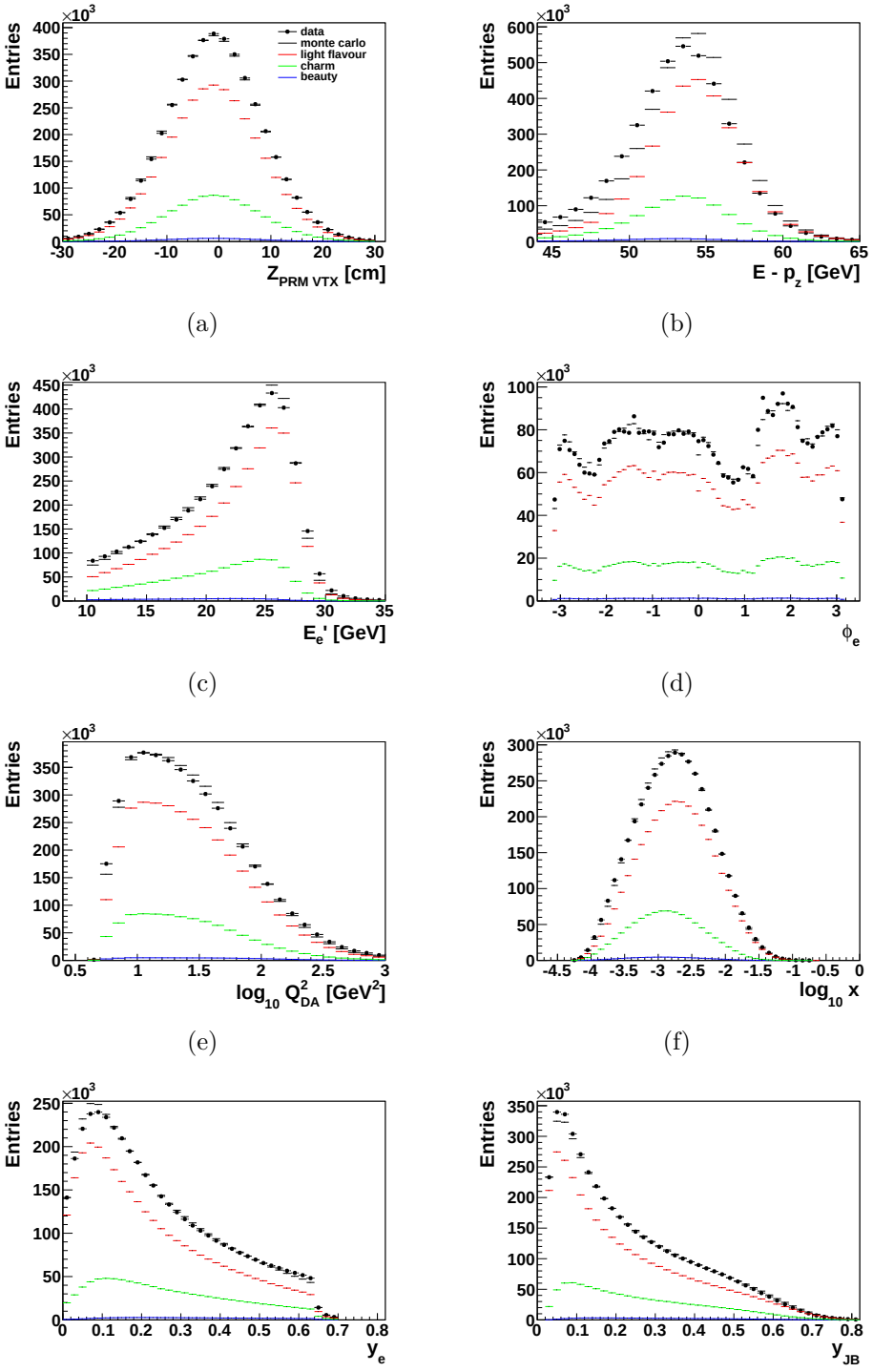

Figure 5.10: The event variables (a) Z_{prm}, (b) $E-p_z$, (c) E'_e, (d) ϕ_e, (e) $\log_{10} Q^2_{DA}$, (f) $\log_{10} x$, (g) y_e, (h) y_{JB} are shown. The data sample (dots) is compared to the Monte Carlo samples which were normalised to the luminosity of the data and scaled with the k-factors from the combined vertexing and tracking analysis.

Chapter 6

Measurement of Differential Cross Sections

In this chapter the differential cross sections derived from the combination of secondary vertexing and tracking information will be presented. Initially, details of the QCD calculations used to compare to the data are described. This is followed by a discussion of the systematic uncertainties on the measurement. Finally, single and double differential charm jet cross sections are presented. In order to illustrate the consistency and improvement of the combination the measurement will be compared to cross sections extracted using secondary vertexing information only.

6.1 NLO QCD Predictions

The theoretical predictions were generated with the HVQDIS [139] program, which provides next-to-leading order QCD calculations for heavy quark production in DIS in the FFNS (see chapter 2.1). The program simulates the hard interaction and provides information about the final state particles at the parton level, i.e. the 4-momenta of the two quarks and, when radiated, a gluon. In order to compare the theoretical predictions with the measurement, the corresponding cross sections need to be defined in a consistent way. The k_T clustering algorithm [105] needs to be run in the same mode as for the cross section measurement of the final state particles. Then the obtained parton level cross sections, σ_{part}, need to be translated to the hadron level. This is achieved by multiplying the parton level cross sections, σ_{part}, with the correction factor C_{had} which is obtained from the Rapgap simulation [118] in the following way:

$$C_{\text{had}} = \frac{\sigma_{\text{had, MC}}}{\sigma_{\text{part, MC}}}. \tag{6.1}$$

Here $\sigma_{\text{had, MC}}$ is the cross section obtained by running the k_T clustering algorithm [105] on the hadron level jets and $\sigma_{\text{part, MC}}$ is the cross section obtained by running the same algorithm on parton level jets, i.e. before the hadronisation.
The HVQDIS program generates NLO QCD predictions on Born level without consideration of real photon emissions from the incoming or outgoing lepton. This means that correction factors, C_{rad}, need to be applied to account for radiative corrections. These are obtained from the MC simulation using the following relation:

$$C_{\text{rad}} = \frac{\sigma_{\text{rad, MC}}}{\sigma_{\text{no rad, MC}}}, \tag{6.2}$$

where the cross section, $\sigma_{\text{rad, MC}}$, is calculated at the hadron level from a Rapgap MC sample that includes full QED corrections and, $\sigma_{\text{no rad, MC}}$, is the cross section calculated at the hadron level from a dedicated Rapgap MC sample in which radiative corrections have been switched off.
The differential charm jet cross sections generated with the HVQDIS simulation were calculated in the same phase space and with the same binning as the measured cross sections. The correction factors were subsequently determined for each differential bin and by applying the theoretical cross sections, σ_{theo}, gave predictions that were directly comparable with the experiment:

$$\sigma_{\text{theo}} = C_{\text{had}} \times C_{\text{rad}} \times \sigma_{\text{part}}. \tag{6.3}$$

The parton densities were taken from the ABKM NLO PDF set [66] in the FFNS, with the number of flavours $n_f = 3$. The pole mass of the charm quark was set to $m_c = 1.5\,\text{GeV}$, while the value of the strong coupling constant, $\alpha_s^{n_f=3} = 0.1135 \pm 0.0014$, was provided by LHAPDF [140, 141] in order to ensure that the same function as in the PDF fit was used. The renormalisation and factorisation scales [134, 135] were set to $\mu_{\text{R}} = \mu_{\text{F}} = \sqrt{Q^2 + 4m_c^2}$.
The uncertainties on the theoretical predictions were evaluated by varying the renormalisation and factorisation scales independently by a factor of $\frac{1}{2}$ and 2. The charm mass was varied between $m_c = 1.3\,\text{GeV}$ and $m_c = 1.7\,\text{GeV}$ and the experimental uncertainties of the data used in the PDF fit were translated to the cross sections. For the variations of the quark mass and the factorisation scale the related PDF set was used, i.e. the PDF set obtained with the value of the respective parameter in the QCD fit. For each variation the deviation from the central value was calculated and the resulting relative errors were added in quadrature for positive and negative variations in order to obtain the total uncertainty for the theoretical predictions. The analysis showed that the uncertainties from the variation of the renormalisation scale, the factorisation scale and the charm mass were of the same order of magnitude.

6.2 Extraction of Cross Sections

The combination of secondary vertexing and tracking information was optimised to detect charm quarks in DIS. The technique of signal extraction returns scaling factors for the charm, beauty and light flavoured MC templates as explained in section 5.1. The total charm jet production cross section, σ, is defined as the number of events, N, containing a charm quark and a jet divided by the integrated luminosity, $\mathcal{L}$, of the data sample:

$$\sigma = \frac{N}{\mathcal{L}}. \tag{6.4}$$

Hence, the inclusive charm jet production cross section can be written as:

$$\sigma = \frac{N^{\text{rec,data}}}{\mathcal{A} \cdot \mathcal{L}_{\text{data}}}, \tag{6.5}$$

where $N^{\text{rec,data}}$ denotes the number of reconstructed charm quark jets in the data sample and $\mathcal{A}$ denotes the acceptance of the detector. On the other hand, the number of charm quark jets in the data sample can be derived using the relation:

$$N^{\text{rec,data}} = k_c \cdot N^{\text{rec,MC}}, \tag{6.6}$$

where k_c denotes the scaling factor from the fit of the MC template to the data sample, and $N^{\text{rec,MC}}$ denotes the number of charm quark jets reconstructed with the Rapgap MC simulation.
The detector acceptance, $\mathcal{A}$, for charm quark jets is obtained as the ratio of the reconstructed charm quark jets, $N^{\text{rec,MC}}$, in the Monte Carlo and the number of jets, $N^{\text{true,HL}}$, on hadron level:

$$\mathcal{A} = \frac{N^{\text{rec,MC}}}{N^{\text{true,HL}}}. \tag{6.7}$$

The combination of equations 6.5, 6.6 and 6.7 gives:

$$\sigma = \frac{k_c \cdot N^{\text{true,HL}}}{\mathcal{L}_{\text{data}}} \ . \tag{6.8}$$

As a consequence the differential cross section as a function of the physical observable Y in a given bin i can be written as:

$$\left(\frac{d\sigma}{dY}\right)_i = \frac{k_{c,i} \cdot N_i^{\text{true,HL}}}{\mathcal{L}_{\text{data}} \cdot \Delta Y_i}, \tag{6.9}$$

where ΔY_i represents the width of the given bin i, and $k_{c,i}$ is the charm scaling factor from the combined fit of the mirrored and subtracted secondary vertexing and impact parameter significance of the MC template to the data sample in the

given bin i.
The differential cross sections in the present analysis have been measured in the following kinematic region:

$$E_T^{\text{jet}} > 2.5 \text{ GeV},$$
$$-1.6 < \eta^{\text{jet}} < 2.2,$$
$$0.02 < y < 0.7,$$
$$5 < Q^2 < 1000\,\text{GeV}^2,$$

In contrast to previous ZEUS measurements [134, 135] of charm production in deep inelastic scattering the lower E_T^{jet} cut means that the measurement presented in this thesis is sensitive to the mass threshold region ($m_c^2 \approx 2.25$ GeV^2). The cut $\eta^{\text{jet}} < 2.2$ was imposed, in order to be in a region of well-understood MVD hit efficiency.

6.3 Systematic Uncertainties

In order to evaluate the systematic uncertainties the signal extraction procedure was changed and the cross sections were subsequently recalculated. The following systematic uncertainties were evaluated, and the impact on the total cross sections are given in parentheses:

- DIS and event selection ($^{+1\%}_{-2\%}$) [134, 135]. In order to evaluate the systematic uncertainty originating from the DIS and event selection, the following variations were applied to the data and the Monte Carlo sample:
  - the cut on y_{JB} was varied by ± 0.01,
  - the cut on E'_e was varied by $\pm$ 1 GeV,
  - the cut on $E - \text{p}_\text{z}$ was varied by $\pm$ 2 GeV.
- Tracking inefficiency ($< 1\%$). To estimate the uncertainty originating from the tracking inefficiency tracks were removed randomly from the Monte Carlo samples with a probability of 2 % according to [142]. The following algorithm [134] was applied to evaluate the systematics:
  - in case the removed track was associated to a secondary vertex fitted with two tracks, the vertex was dropped in the signal extraction procedure.
  - in case the removed track was associated to a secondary vertex fitted with more than two tracks, the secondary vertex significance was reduced by a factor $\sqrt{(N-1)N}$ and the secondary vertex multiplicity was reduced by a factor $(N-1)/N$.

- Smearing ($\pm 2\%$). In order to evaluate the uncertainty originating from the smearing of the decay length and the impact parameter, the cross sections were calculated before and after the smearing was applied.

- Q^2 reweighting ($\pm 2\%$). To estimate the impact of the Q^2 reweighting in the Rapgap MC, the reweighting was varied by $\pm 50\%$.

- Electromagnetic energy scale ($< 1\%$). In order to evaluate the effect of the uncerainty from the EM scale [143] the energy of the scattered electron was raised and lowered by 1%.

- Calorimeter energy scale $\binom{-3\%}{+2\%}$. To evaluate the uncertainty originating from the calorimeter energy scale [144], the transverse energy, E_T^{jet}, of the jets was varied by 3% in the MC samples. The value was adopted from the secondary vertexing analysis with a cut of $E_T^{\text{jet}} > 4.2$ GeV, given that the contribution of jets at lowest transverse energy, $E_T^{\text{jet}} < 4.2$ GeV, is small for the present analysis.

- FLT efficiency (+1%) [134, 135]. The efficiency of the track condition was underestimated by the Monte Carlo by 5%. Consequently, all events in the MC were reweighted with the weight 0.95 as long as they were not accepted by the slot FLT30 which did not make use of the track condition.

- Signal extraction $\binom{-2\%}{+3\%}$. To evalute the systematic uncertainty originating from the signal extraction the interval used in the fit was varied separately by ± 1 in the mirrored and subtracted decay length significance, $S^+_{vtx} - S^-_{vtx}$ of the secondary vertexing analysis and by ± 1 in the mirrored and subtracted impact parameter significance, $S^+_{trk} - S^-_{trk}$ of the tracking analysis. The resulting uncertainties were added in quadrature to obtain the final uncertainty on the signal extraction of the combined secondary vertexing and tracking analysis.

- Light flavour asymmetry ($\pm 2\%$). To estimate the impact of uncertainties in the simulation originating from secondary interactions in the detector material the asymmetry of the light flavour samples was varied by $\pm 30\%$ according to [60].

- Charm fragmentation function (+1%) [135]. The Peterson fragmentation function with parameter $\epsilon = 0.062$ was used to evaluate the sensitivity of the results to the longitudinal momentum transfer. The fraction of longitudinal momentum transferred from the charm quark to the charmed hadrons is represented by the variable $z_{had} = (E + p_{||})_{had}/E_{string}$, where E_{had} is the energy of the charmed hadron, $p_{||}$ the longitudinal momentum projected onto the struck quark and E_{string} is the energy of the string. The variable z_{had} was reweighted with a continuous function up to a factor $\pm$ 2.5, and the

results were subsequently compared to the measurement using the Bowler fragmentation function.

- Charm fragmentation fractions $\binom{+3.3\%}{-2.4\%}$. Given that the charm fragmentation fractions were not up to date in the MC simulation, a reweighting procedure was developed to use the world average values [135]. The systematic uncertainty was evaluated by varying the fragmentation fractions within their uncertainties, and subsequently repeating the reweighting and the fits.

- Branching ratios $\binom{+1.0\%}{-1.1\%}$. As the branching ratios for charm were not up to date in the MC simulation, a reweighting procedure was developed to use the world average values [135]. The systematic uncertainty was evaluated by varying the branching ratios within their uncertainties, and subsequently repeating the reweighting and the fits.

- Luminosity (2%). The uncertainty on the luminosity measurement at ZEUS was determined to be 2 %. The uncertainty was not included in the measurements of the differential cross sections.

The individual contributions from the systematic uncertainties were calculated separately for each differential bin of the measurement and added in quadrature for positive and negative variations. The results of the evaluation of the systematics are summarised as relative uncertainties in Appendix C. In this context the same assumptions were made for each bin of the measured differential cross section.

6.4 Results

In this section differential cross sections of jet production in charm events measured using the combination of tracking and vertexing information in DIS events at HERA are presented. The measured cross sections are compared with NLO QCD predictions in the FFNS, generated with the HVQDIS program and corrected for hadronisation and radiation effects. Finally, a comparison with the measurement based on secondary vertex tagging will be presented to illustrate the agreement and improvement between the different techniques of signal extraction.
The tables of single and double differential jet cross sections in charm events as function of the transverse jet energy, E_T^{jet}, the pseudorapidity, η^{jet}, the photon virtuality, Q^2, and the Bjorken variable, x, are given in Appendix A. In figures 6.1 and 6.2 single differential jet cross sections as a function of the transverse jet energy, E_T^{jet}, and the pseudorapidity, η^{jet}, of the selected jets and a comparison with next-to-leading order QCD predictions are shown. The differential cross section

in E_T^{jet} falls off by three orders of magnitude, and is well-described by theoretical predictions, which implies a reasonable understanding of the underlying parton dynamics. The single differential cross section in η^{jet} agrees reasonably well with next-to-leading order QCD prediction.
In figures 6.3 and 6.4 single differential charm jet cross sections as a function of the photon virtuality, Q^2, and the Bjorken scaling variable, x, in DIS events at HERA are shown. The differential cross section in Q^2 falls off by three orders of magnitude and is well-described by the theoretical predictions. This allows to measure $F_2^{c\bar{c}}$ in this regime with higher precision than in previous analyses, due to the extension of the kinematic region towards lower values of the transverse jet energy, E_T^{jet} and gives confidence for the extraction of $F_2^{c\bar{c}}$.
In figure 6.5, 6.6 and 6.7 differential charm jet cross sections as a function of the Bjorken scaling variable, x, are shown for various values of the photon virtuality, Q^2. The double differential cross sections in Q^2 and x will be used to extract the charm contribution, $F_2^{c\bar{c}}$, to the structure functions of the proton. As the extrapolation from the visible cross sections to the full kinematic phase space is performed using theoretical models, the extraction procedure requires a reasonable agreement between the measured cross sections and theoretical predictions. Generally, the NLO QCD predictions agree reasonably well with the differential cross sections, allowing extraction of $F_2^{c\bar{c}}$ with reduced extrapolation uncertainties.
In general NLO QCD predictions in the fixed-flavour number scheme are affected by multiple scale problems in the kinematic regions of high photon virtuality, Q^2, and transverse quark momentum, p_T, due to logarithmic terms that need to be resummed. However, no significant deviations between data and theoretical predictions were observed for the present measurement even at high Q^2 and high E_T^{jet}. This observation confirms inclusive measurements performed with the ZEUS [134, 135] and H1 detectors [58–60, 138] as well as combined results from both collaborations [62].

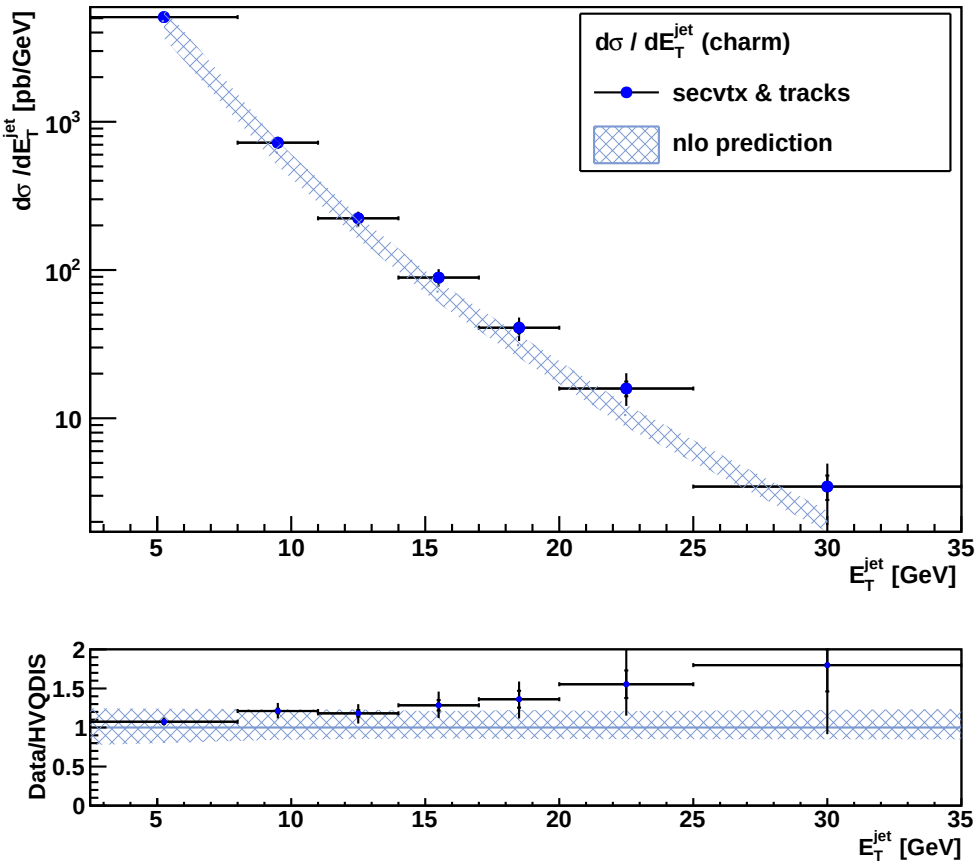

Figure 6.1: Differential charm jet cross section as a function of the transverse jet energy E_T^{jet} in DIS events at HERA. The measurement is based on the combination of tracking and vertexing information, and compared with NLO QCD predictions generated with the HVQDIS program, corrected for hadronisation and radiation effects.

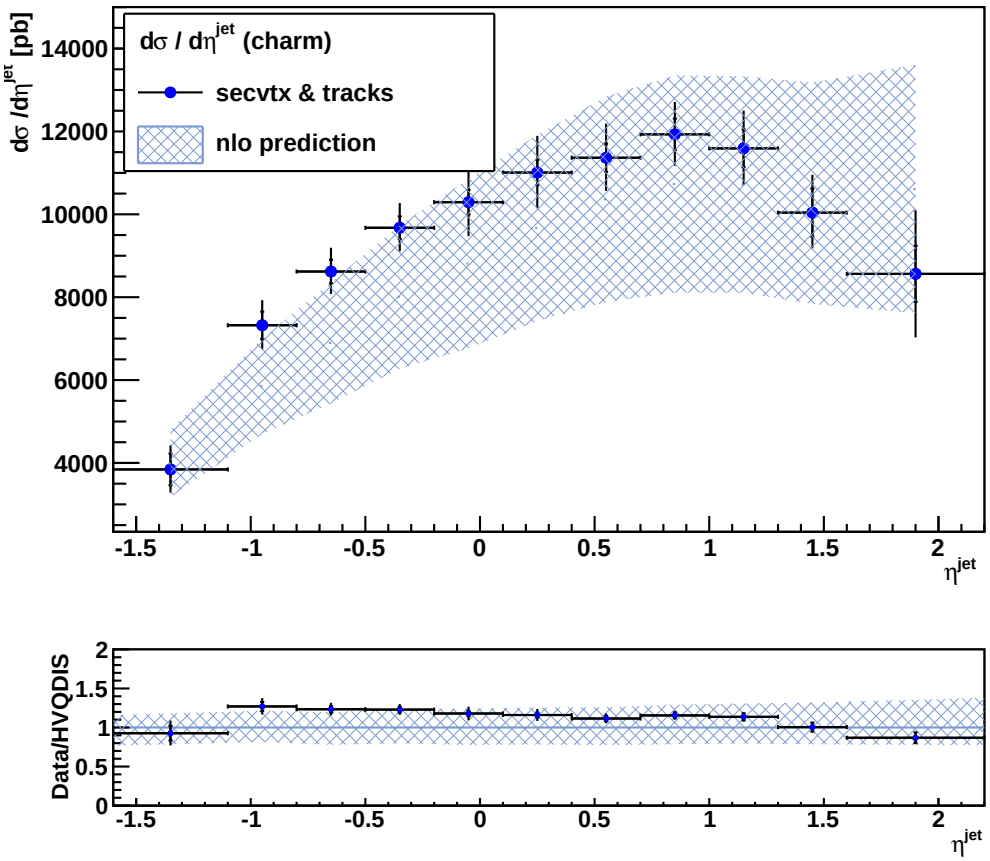

Figure 6.2: Differential charm jet cross section as a function of the pseudorapidity η^{jet} of the jets in DIS events at HERA. The measurement is based on the combination of tracking and vertexing information, and compared with NLO QCD predictions generated with the HVQDIS program, corrected for hadronisation and radiation effects.

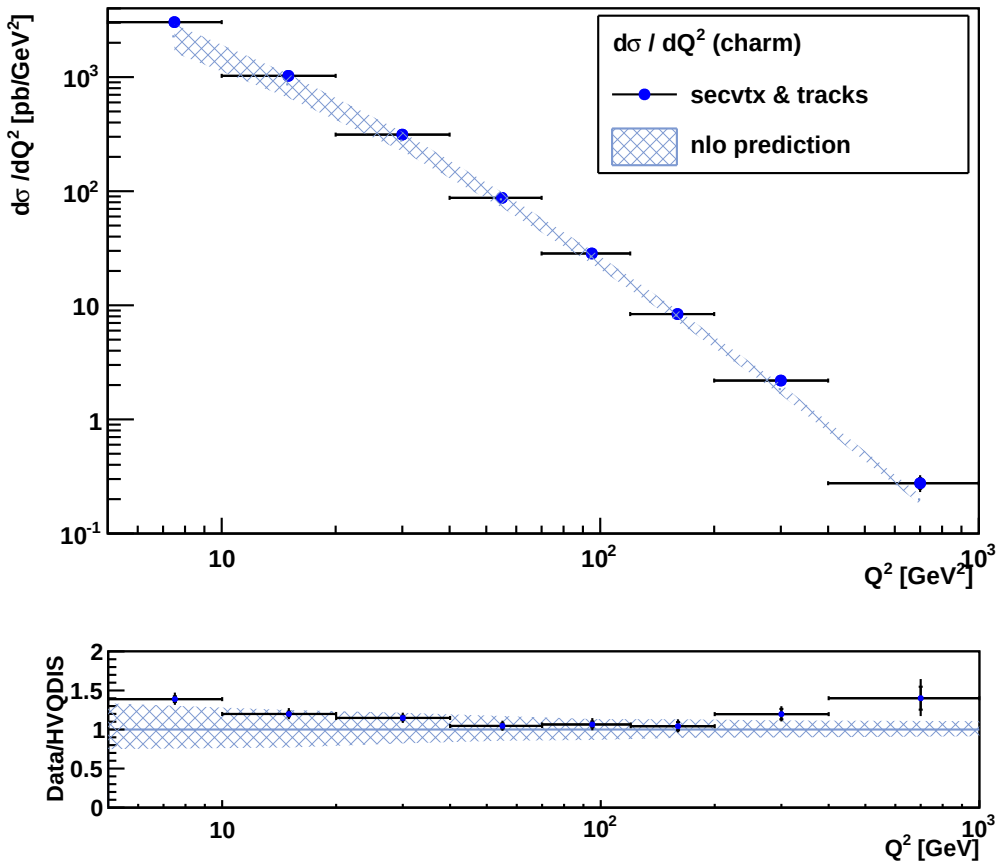

Figure 6.3: Differential charm jet cross section as a function of the photon virtuality Q^2 in DIS events at HERA. The measurement is based on the combination of tracking and vertexing information, and compared with NLO QCD predictions generated with the HVQDIS program, corrected for hadronisation and radiation effects.

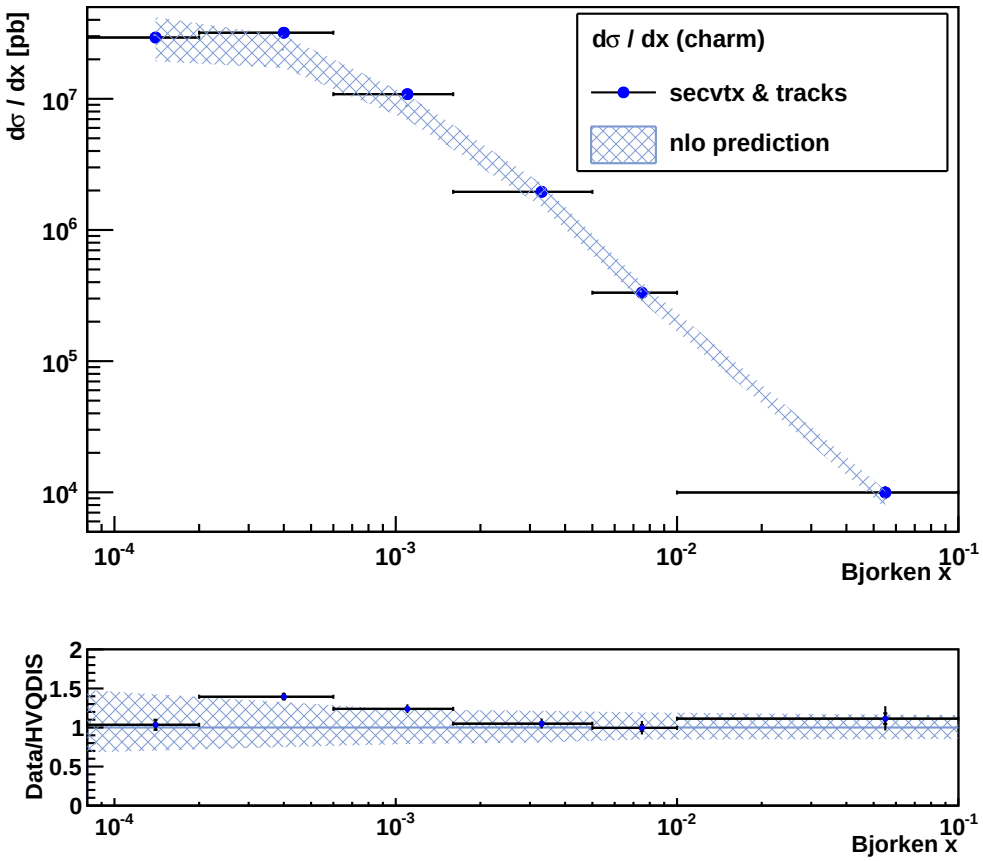

Figure 6.4: Differential charm jet cross section as a function of the Bjorken scaling variable x in DIS events at HERA. The measurement is based on the combination of tracking and vertexing information, and compared with NLO QCD predictions generated with the HVQDIS program, corrected for hadronisation and radiation effects.

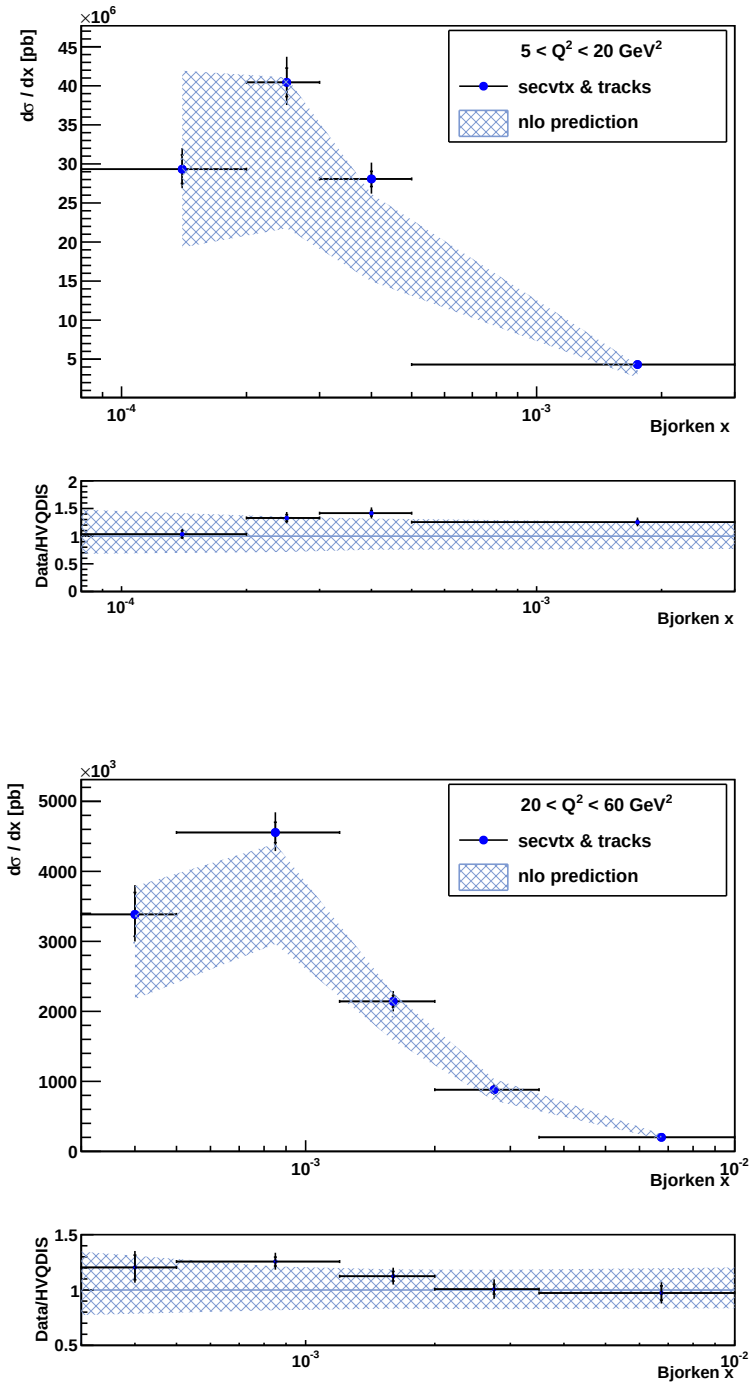

Figure 6.5: Differential charm jet cross section as a function of the Bjorken scaling variable x for the the photon virtuality $5 < Q^2 < 20\,\mathrm{GeV}^2$ and $20 < Q^2 < 60\,\mathrm{GeV}^2$. The measurement is based on the combination of tracking and vertexing information, and compared with NLO QCD predictions generated with the HVQDIS program, corrected for hadronisation and radiation effects.

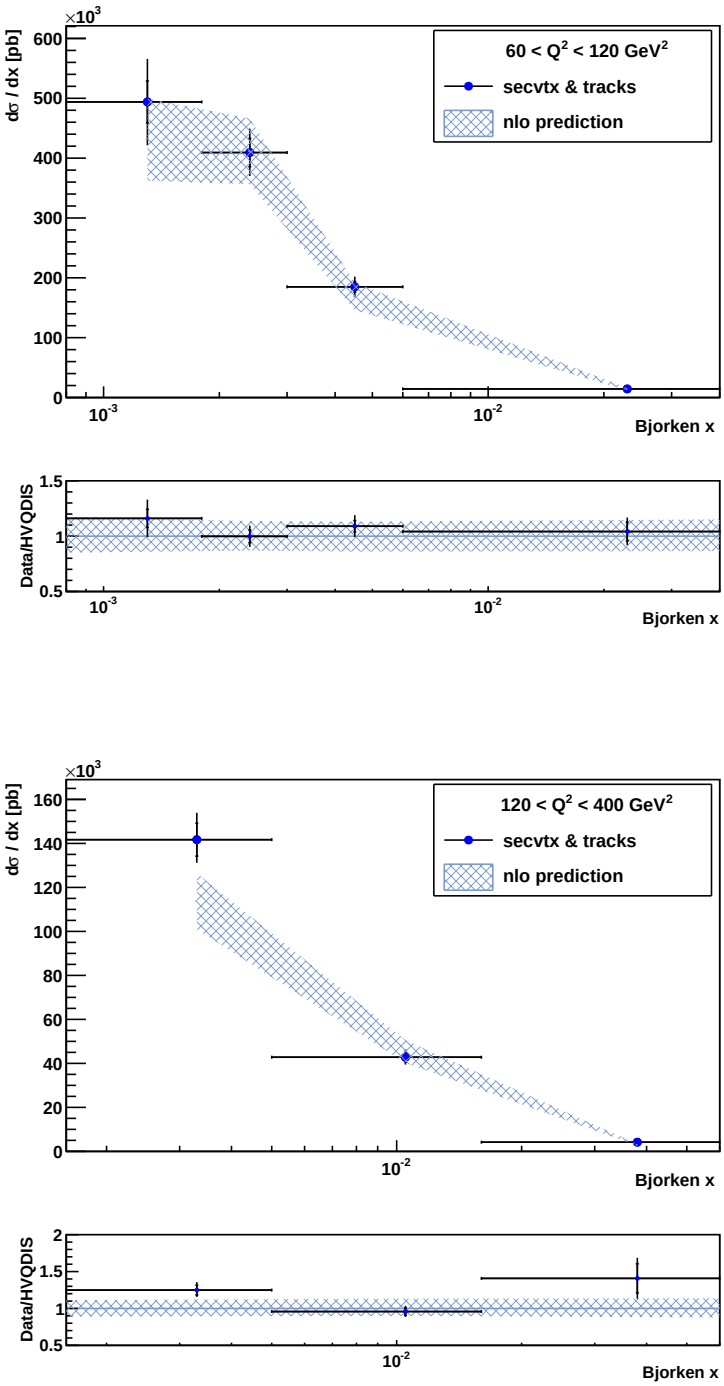

Figure 6.6: Differential charm jet cross section as a function of the Bjorken scaling variable x for the the photon virtuality $60 < Q^2 < 120\,\mathrm{GeV}^2$ and $120 < Q^2 < 400\,\mathrm{GeV}^2$. The measurement is based on the combination of tracking and vertexing information, and compared with NLO QCD predictions generated with the HVQDIS program, corrected for hadronisation and radiation effects.

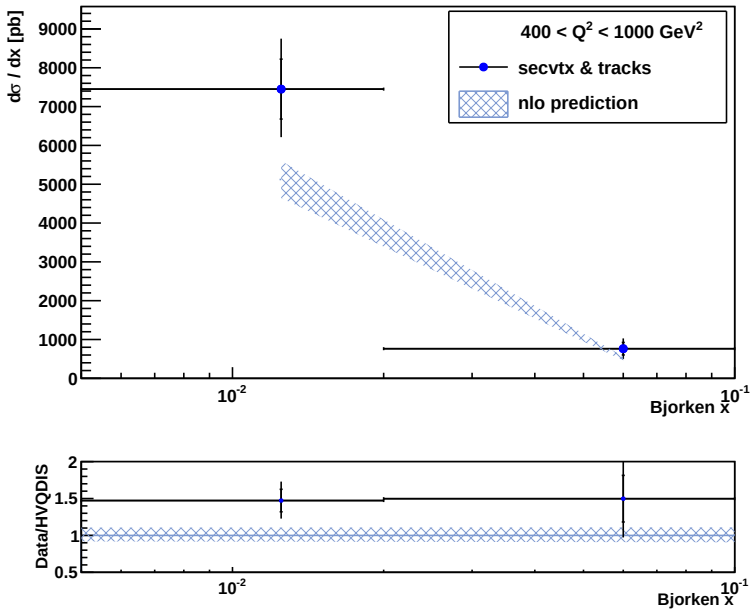

Figure 6.7: Differential charm jet cross section as a function of the Bjorken scaling variable x for the the photon virtuality $400 < Q^2 < 1000$ GeV^2. The measurement is based on the combination of tracking and vertexing information, and compared with NLO QCD predictions generated with the HVQDIS program, corrected for hadronisation and radiation effects.

6.5 Comparison of Techniques

In this section the differential charm jet cross sections as a function of the photon virtuality, Q^2, and Bjorken scaling variable, x, measured with the combined secondary vertexing and tracking technique are compared to cross sections extracted with the secondary vertexing method within the same analysis framework. The comparison is crucial to prove the consistency of the combined vertexing and tracking technique, demonstrate the improvement from the combination, and gain confidence in the method of signal extraction that will be used to extract the charm contribution, $F_2^{c\bar{c}}$, to the structure function of the proton.
In figure 6.8 a comparison between the single differential charm jet cross sections as a function of Q^2 and x extracted with the combined technique and the corresponding cross sections extracted with the secondary vertexing technique is shown. The differential cross sections in Q^2 and x fall by three orders of magnitude and show a good agreement for the different techniques of signal extraction.
In figures 6.9, 6.10 and 6.11 a comparison between the differential cross sections in x, extracted with the combined and the secondary vertexing technique, is shown for various values of the photon virtuality, Q^2. One observes a good agreement between the measurements, within the statistical uncertainties in the whole kinematic region.
Figure 6.12 shows a comparison between the relative statistical uncertainty of the differential cross sections in x for various values of Q^2 for the secondary vertexing technique and the corresponding uncertainty for the combined vertexing and tracking technique. The comparison illustrates an improvement of the relative statistical uncertainty of about 40 %, which is particularly large in the low and middle Q^2 range. A further comparison of the systematic uncertainties shows that the combination of tracking and vertexing information leads to a reduction of the systematics due to an improved tracking efficiecy. In comparison with the secondary vertexing analysis the combination has reduced the uncertainty from the tracking inefficiency from 3% to below 1% (see section 6.3), while the other systematic uncertainties have stayed the same.
It can be concluded that the combined secondary vertexing and tracking technique is consistent with the secondary vertexing technique in the whole kinematic region of Q^2 and x. The combination of secondary vertexing and tracking information results in an improved statistical precision with reduced systematic uncertainties due to the improved tracking efficiency. In the next chapter it will be explained how the double differential cross sections shown in figures 6.5, 6.6 and 6.7 are used to extract $F_2^{c\bar{c}}$ with higher precision than in previous measurements.

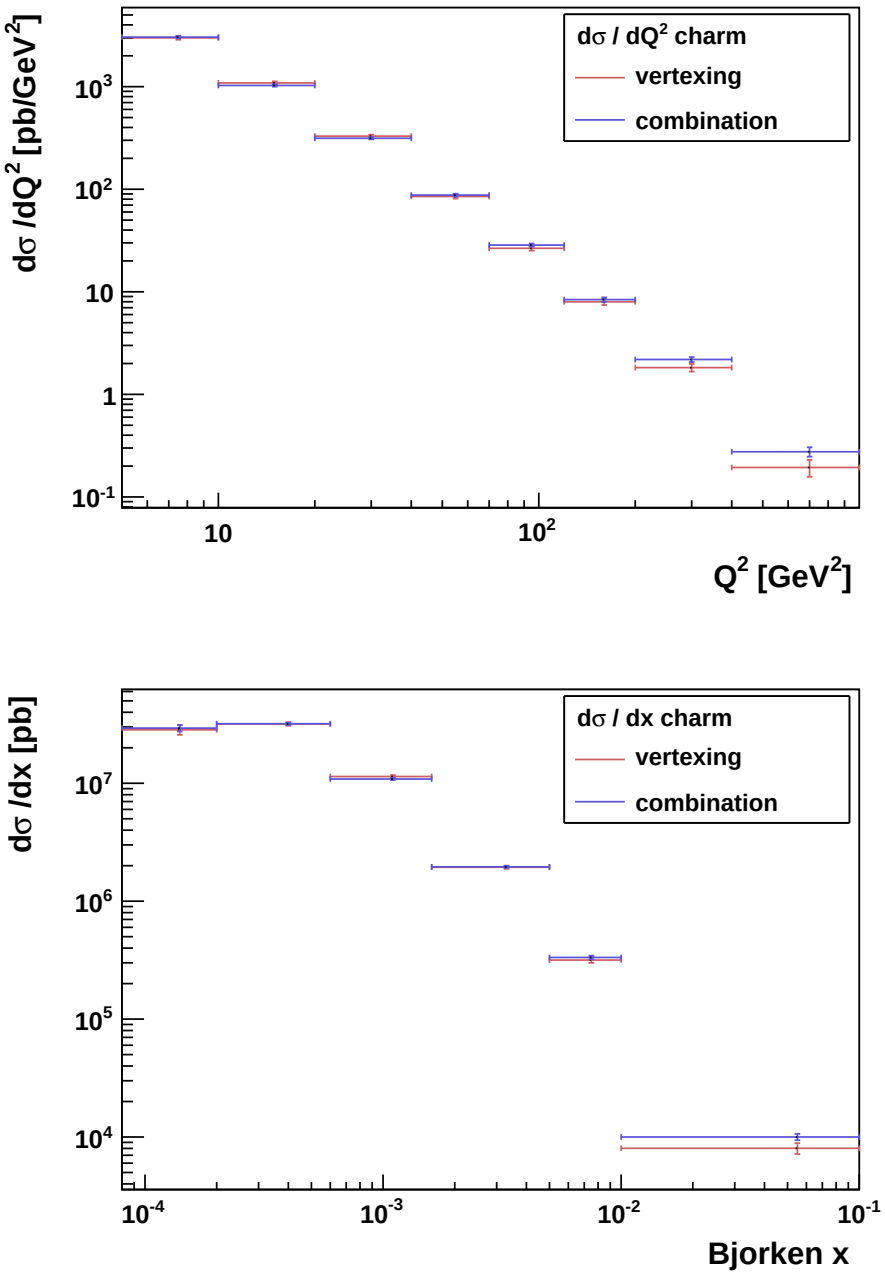

Figure 6.8: Differential charm jet cross sections as function of the photon virtuality, Q^2, Bjorken scaling variable, x, in DIS. A comparison between the combination of impact parameter and secondary vertexing tagging and the secondary vertexing technique is shown within the same analysis framework to illustrate the agreement between results based on different techniques of signal extraction. The error bars represent the statistical uncertainties of the respective measurement.

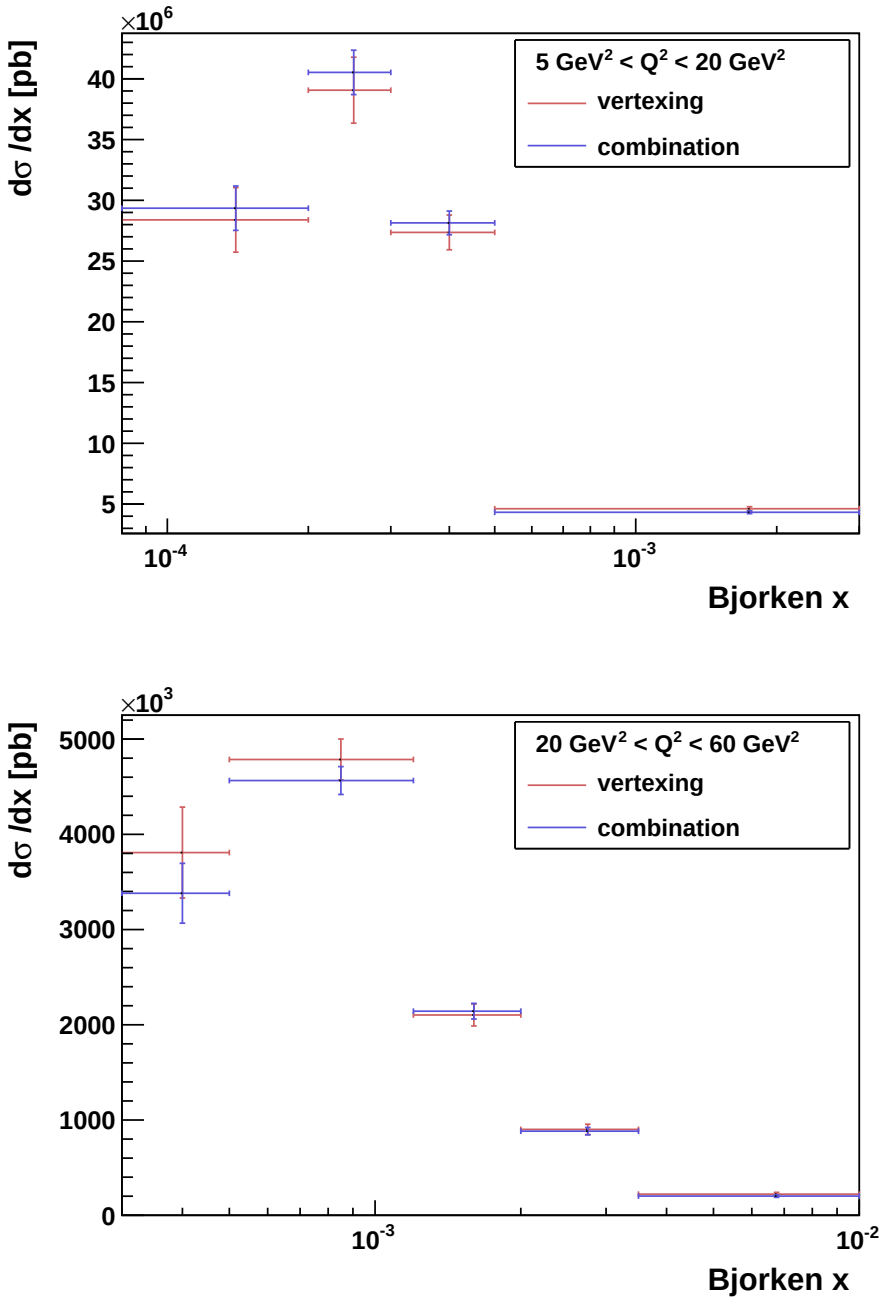

Figure 6.9: Differential charm jet cross sections as function of the Bjorken scaling variable x for the photon virtuality $5 < Q^2 < 20$ GeV^2 and $20 < Q^2 < 60$ GeV^2 in DIS. A comparison between the combination of impact parameter and secondary vertexing tagging and the secondary vertexing technique is shown within the same analysis framework to illustrate the agreement between results based on different techniques of signal extraction. The error bars represent the statistical uncertainties of the respective measurement.

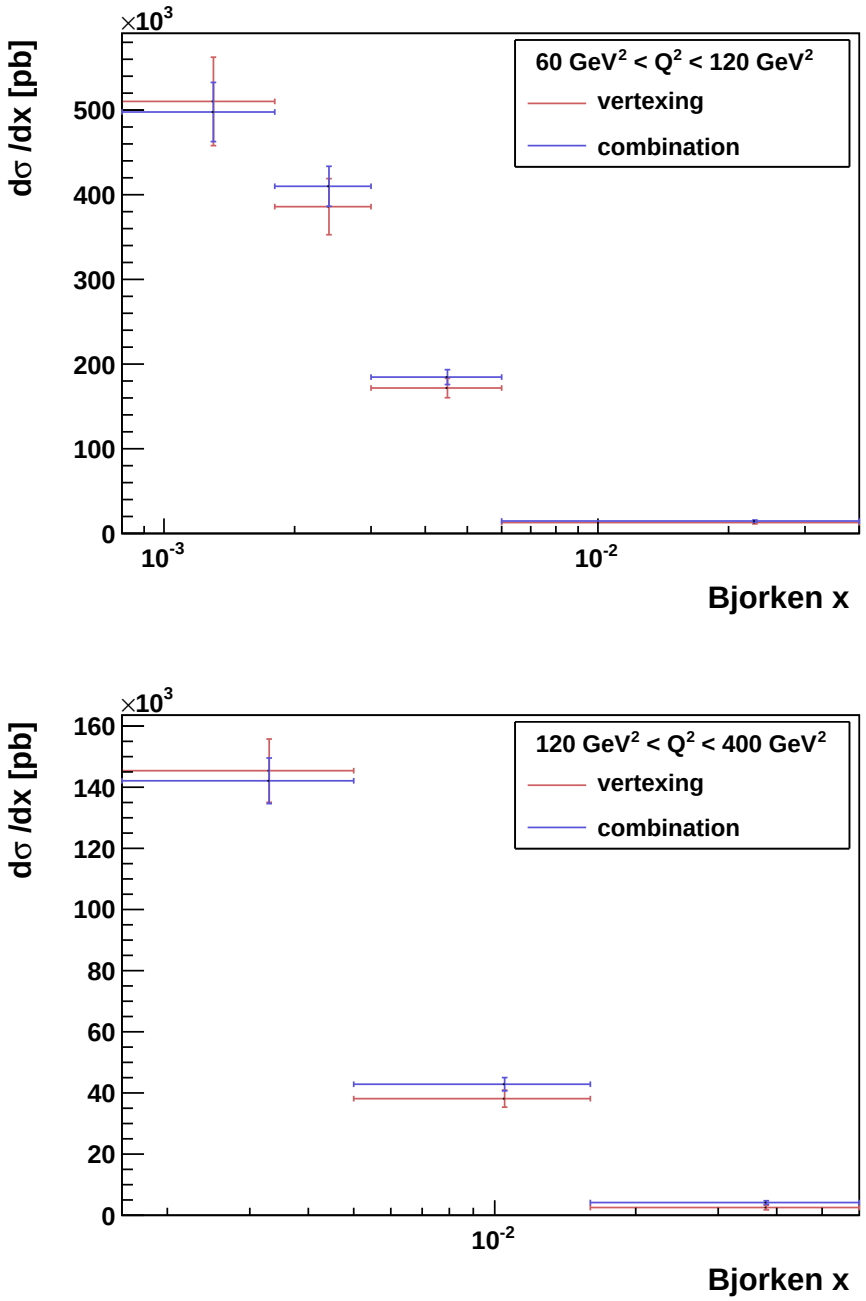

Figure 6.10: Differential charm jet cross sections as function of the Bjorken scaling variable x for the photon virtuality $60 < Q^2 < 120\,\mathrm{GeV}^2$ and $120 < Q^2 < 400\,\mathrm{GeV}^2$ in DIS. A comparison between the combination of impact parameter and secondary vertexing tagging and the secondary vertexing technique is shown within the same analysis framework to illustrate the agreement between results based on different techniques of signal extraction. The error bars represent the statistical uncertainties of the respective measurement.

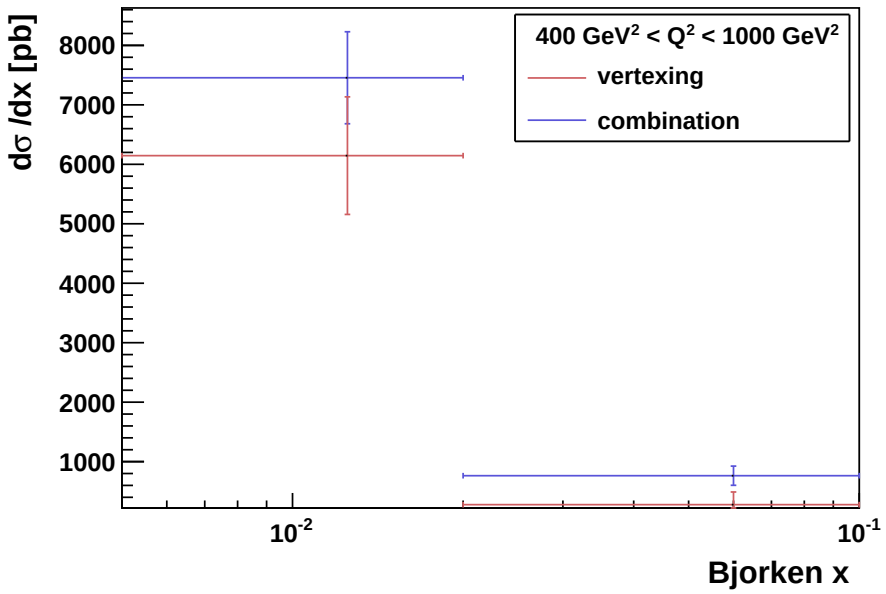

Figure 6.11: Differential charm jet cross sections as function of the Bjorken scaling variable x for the photon virtuality $400 < Q^2 < 1000$ GeV^2 in DIS. A comparison between the combination of impact parameter and secondary vertexing tagging and the secondary vertexing technique is shown within the same analysis framework to illustrate the agreement between results based on different techniques of signal extraction. The error bars represent the statistical uncertainties of the respective measurement.

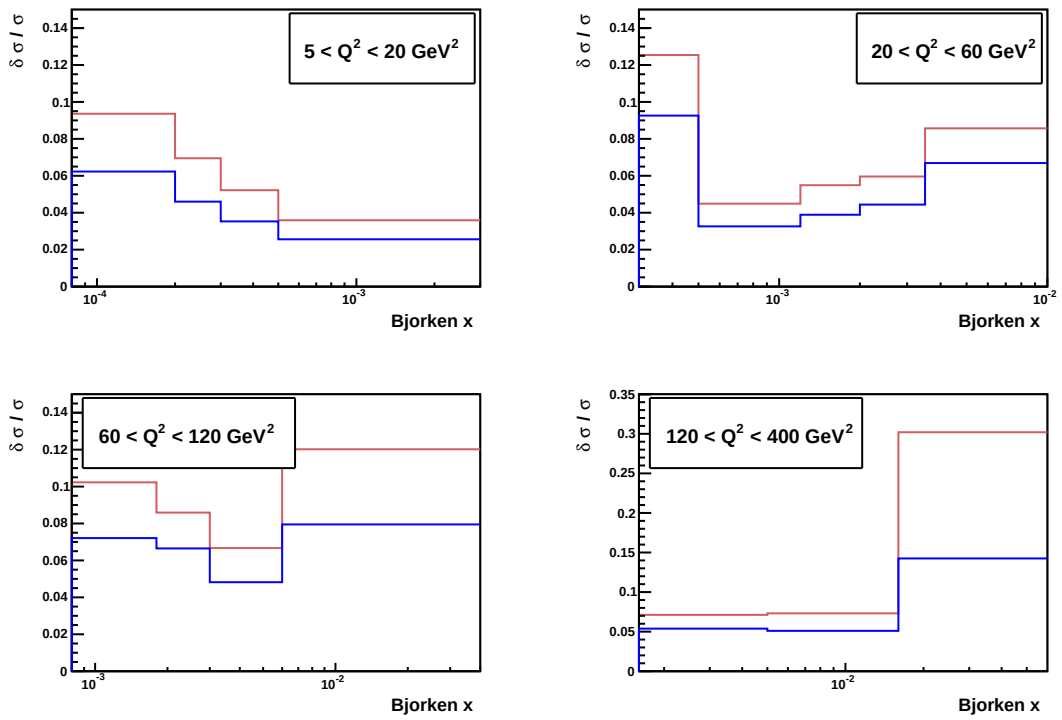

Figure 6.12: Comparison of relative statistical uncertainties of differential cross sections in x for various values of Q^2 for the combined technique and the secondary vertexing technique.

Chapter 7

Extraction of $F_2^{c\bar{c}}$ Using Combination

In order to compare different measurements one needs to extrapolate to a common phase space. As theoretical calculations are typically performed for inclusive quantities (e.g. [28, 29, 34]), the extrapolation is performed to the full phase space. In this chapter the extrapolation of the double-differential cross sections to the full phase space and the extraction of the charm contribution, $F_2^{c\bar{c}}$, to the structure function of the proton will be performed. The values of $F_2^{c\bar{c}}$ measured with the combined tracking and vertexing algorithm will subsequently be compared to previous measurements based on the secondary vertexing technique and to NLO QCD predictions using the parton density function set HERAPDF 1.0.

7.1 Extraction of $F_2^{c\bar{c}}$

As particle detectors have a limited acceptance the measured double-differential cross sections in Q^2 and x will be constrained to a restricted phase space in pseudorapidity η^{jet} and transverse jet energy E_T^{jet}. In order to compare different measurements and extract the charm contribution, $F_2^{c\bar{c}}$, to the structure function of the proton an extrapolation to the full kinematic phase space is performed. The extrapolation is based on NLO QCD predictions in the FFNS obtained from the HVQDIS [139] program:

$$F_{2,exp}^{c\bar{c}}(x_i, Q_j^2) = \frac{d^2\sigma_{exp}^{c\bar{c}}(x_i, Q_j^2) \,/\, dx_i \, dQ_j^2}{d^2\sigma_{theo}^{c\bar{c}}(x_i, Q_j^2) \,/\, dx_i \, dQ_j^2} \; F_{2,theo}^{c\bar{c}}(x_i, Q_j^2), \tag{7.1}$$

where the values x_i and Q_j^2 define a bin in the $x - Q^2$ plane. $F_{2,exp}^{c\bar{c}}(x_i, Q_j^2)$ represents the experimental value of the charm contribution to the structure function of the proton, and $F_{2,theo}^{c\bar{c}}(x_i, Q_j^2)$ is the theoretical value from NLO QCD

calculations in this bin. Here $d^2\sigma^{c\bar{c}}_{exp}(x_i, Q^2_j)/dx_i dQ^2_j$ is the differential cross section measured with the combined secondary vertexing and tracking method and $d^2\sigma^{c\bar{c}}_{theo}(x_i, Q^2_j)/dx_i dQ^2_j$ the predicted double-differential cross section from the HVQDIS program.
For the calculation of the theoretical quantities required to extract $F_2^{c\bar{c}}$, the same HVQDIS settings were used as for the computation of the theoretical predictions, which were compared with the measured differential cross sections in chapter 6. The values of $F^{c\bar{c}}_{2,theo}(x_i, Q^2_j)$ were extracted from the inclusive charm quark production cross section in the vicinity of each point in the $x - Q^2$ plane:

$$\frac{d^2\sigma^{c\bar{c}}}{dxdQ^2} = \frac{2\pi\alpha_s^2}{Q^2 x}\Big[\Big(1 + \big(1-y\big)^2\Big)F^{c\bar{c}}_{2,theo}(x_i, Q^2_j) - y^2 F^{c\bar{c}}_L(x_i, Q^2_j)\Big], \tag{7.2}$$

where $F^{c\bar{c}}_L(x_i, Q^2_j)$ is the contribution from the longitudinal structure function, which needs to be subtracted. The running of the strong coupling constant, α_s, was taken into account for the extraction of $F^{c\bar{c}}_{2,theo}(x_i, Q^2_j)$.
For the calculation of the theoretical uncertainties three different parameters were varied separately. First of all, the PDF uncertainties were propagated from the experimental uncertainties of the fitted data. Subsequently, the charm quark mass was varied by ± 0.2 GeV, and finally the renormalisation and factorisation scales were varied by a factor of two. The uncertainty on the extrapolation was calculated by simultaneously varying the settings of the HVQDIS program for the calculation of $d^2\sigma^{c\bar{c}}_{theo}(x_i, Q^2_j)/dx_i dQ^2_j$ and $F^{c\bar{c}}_{2,theo}(x_i, Q^2_j)$, and adding the respective uncertainties in quadrature.
As the extrapolation is based on theoretical assumptions a reasonable agreement between the double-differential cross sections in Q^2 and x and next-to-leading order QCD predictions is important to assure that one can proceed with the extraction procedure. From figures 6.5, 6.6 and 6.7 one can conclude that the next-to-leading order QCD predictions are in reasonable agreement with the measured double-differential cross sections. On the other hand, it is crucial to maximise the phase space in order be less reliant on theoretical assumptions and consequently reduce extrapolation uncertainties. This is the reason why the cut on the transverse jet energy, E_T^{jet}, has been relaxed to 2.5 GeV in the present analysis. Relaxing the cut on the transverse energy will significantly reduce extrapolation uncertainties in the low Q^2 and low x region compared to previous analyses [134, 135] with the ZEUS detector.

7.2 Results for $F_2^{c\bar{c}}$

The estimated values for the charm contribution, $F_2^{c\bar{c}}$, to the proton structure function extracted with the combined vertexing and tracking technique are given in Appendix B. Figure 7.1 shows the results for $F_2^{c\bar{c}}$ as a function of the Bjorken

scaling variable, x, for different values of photon virtuality, Q^2. The values extracted with the combined secondary vertexing and tracking technique are compared to a previous measurement based on the secondary vertexing technique [134]. Both measurements are compared to next-to-leading order QCD predictions in the fixed flavour number scheme using HERAPDF 1.0 [65] as parton density for the proton. It can be seen that the measurements based on different techniques of signal extraction are generally in reasonable agreement. The inner error bars, which represent the statistical uncertainties, are smaller for the combined tracking and vertexing technique.
Regardless of the technique of signal extraction the improved agreement with NLO QCD predictions also has to be attributed to the extended phase space, which results in reduced extrapolation uncertainties. The extrapolation factors, which represent a measure of the inclusiveness of the measurement, are typically between 1 and 2 for the present measurement, based on the combined vertexing and tracking technique. The same extrapolation factors used to be about 2 in the middle Q^2 regime and about 4 in the low Q^2 regime for the previously performed secondary vertexing measurement. This means that the extension of the phase space has significantly reduced the extrapolation uncertainties [134, 135] and consequently the dependence on theoretical predictions.
At low $Q^2 < 25\,\mathrm{GeV}^2$ the description of the data is worse than at higher Q^2 values. This may indicate a somewhat larger gluon density and these data will improve the extraction of the proton PDFs. In the future PDF sets will be extracted using a combination of inclusive DIS and charm measurements [62] based on combined HERA I and HERA II data. This would include the most precise measurements of the H1 and ZEUS collaborations, reduce the uncertainty on the quark and gluon density and subsequently improve the comparison with the present measurement.

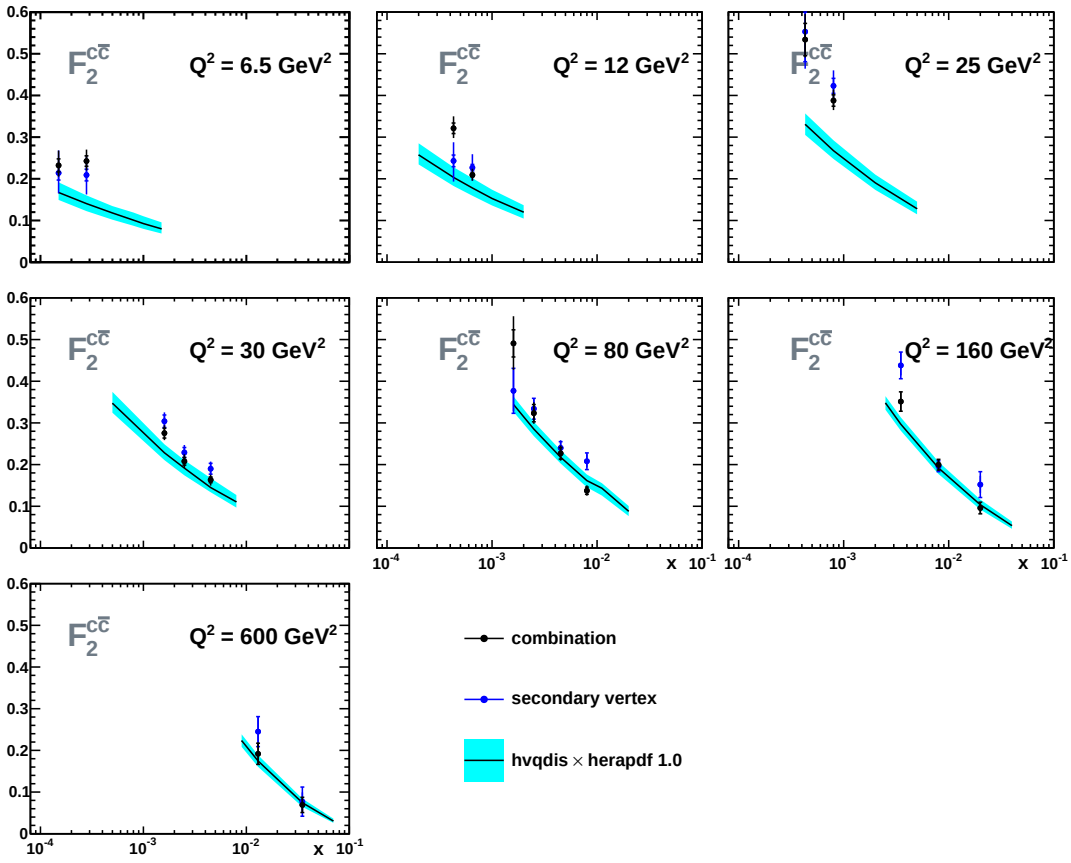

Figure 7.1: The charm contribution, $F_2^{c\bar{c}}$, to the structure function of the proton as a function of x for different values of Q^2, extracted on the basis of the combined secondary vertexing and tracking technique. The results of the combined method are compared to the values of a previous measurement (preliminary) based on the secondary vertexing technique. In the secondary vertexing measurement the cuts $-1.6 < \eta^{\text{jet}} < 2.2$, $E_T^{\text{jet}} > 4.2$ GeV were applied for the jet selection. Both measurements are compared to NLO QCD predictions (black) in the FFNS, estimated using the parton density function HERAPDF 1.0 for the proton. The blue band represents the theoretical uncertainties originating from the variation of the charm mass, the factorisation and renormalisation scale.

Chapter 8

Conclusions and Outlook

8.1 Conclusions

A novel algorithm has been developed to detect charm quarks in deep inelastic scattering events at HERA. The combined algorithm exploits secondary vertexing and tracking information to perform the most inclusive measurement of charm production in DIS events with the ZEUS detector. In events containing a well-reconstructed secondary vertex the decay length significance and secondary vertex mass are used to extract the heavy quark content of the data sample. In events without a well-reconstructed secondary vertex the impact parameter of jet-associated tracks is used for the signal extraction. Finally, in events containing a jet associated to a vertex that did not pass the secondary vertex selection, the signed impact parameter of jet-associated tracks is used additionally for the extraction of the heavy quark content of the data sample.
Single and double differential cross sections of charm production in deep inelastic scattering events have been measured employing the novel algorithm in the kinematic range $E_T^{\rm jet} > 2.5\,{\rm GeV}$, $-1.6 < \eta^{\rm jet} < 2.2$, $0.02 < y < 0.7$ and $5 < Q^2 < 1000\,{\rm GeV}^2$. In comparison with previous analyses performed with the ZEUS detector the cut on the transverse jet energy, $\mathrm{E_T^{jet}}$, has been relaxed in order to obtain sensitivity to the charm mass threshold. The measurement has been found to be in agreement with results of the secondary vertexing analysis within the same analysis framework and with next-to-leading order QCD prediction in the fixed-flavour number scheme generated with the HVQDIS program. In comparison with the secondary vertexing analysis the combination of tracking and vertexing information has reduced the relative statistical error by about 40 %, the most dramatic improvement being in the low Q^2 and low x region. The systematic uncertainties have been found to be comparable with the secondary vertexing analysis. However, the combination of tracking and vertexing information has improved the control and stability of the measurement, and reduced the uncertainty originating from the tracking inefficiency.

Finally, the charm contribution to the structure function of the proton has been extracted. The estimated values of $F_2^{c\bar{c}}$ have been found to be in agreement with next-to-leading order QCD predictions in the fixed-flavour number scheme using HERAPDF 1.0 as the parton density function. In comparison with previously performed secondary vertexing analyses the combined algorithm has improved the agreement with theoretical predictions and reduced the extrapolation uncertainties due to the relaxed cut on the transverse jet energy, E_T^{jet}, which makes the estimated values less dependent on theoretical predictions.

8.2 Outlook

The combined vertexing and tracking algorithm, which has been presented in this thesis, allows for the most inclusive and most precise measurements of charm production cross sections in DIS events at HERA to be made with the ZEUS detector. The algorithm exploits information that has not been considered previously in inclusive measurements based on the decay length significance and secondary vertex mass. A possible extension would not require a well-reconstructed secondary vertex or jet reconstructed with the k_{T} clustering algorithm, but simply require a reference axis to define a sign for the impact parameter of tracks. A possible choice for the reference axis would be the direction of the scattered electron that is reconstructed in DIS events. This requirement would allow for the exploitation of additional tracks in the previously analysed events, which are not associated to jets reconstructed with the k_{T} clustering algorithm, and for the inclusion of additional events not containing a well-reconstructed jet. Furthermore, one could consider the inclusion of additional variables with the potential to improve the separation between charm and beauty quarks, and feed these variables into a neural network to enhance the sensitivity of the present analysis.

Appendix A

Single and Double Differential Charm-Jet Cross Sections

Q^2 (GeV^2)	$\mathrm{d}\sigma/\mathrm{d}Q^2$ (pb/GeV^2)	Δ_{stat} (pb/GeV^2)	Δ_{sys} (pb/GeV^2)	$\mathrm{C_{had}}$	$\mathrm{C_{rad}}$
5 : 10	3034	80	+164/–139	1.29	0.98
10 : 20	1026	26	+59/–50	1.23	0.99
20 : 40	313	7.85	+16.65/–15.45	1.20	0.98
40 : 70	87.43	2.80	+4.83/–4.40	1.19	0.97
70 : 120	28.46	1.02	+1.92/–1.72	1.20	0.97
120 : 200	8.38	0.41	+0.56/–0.49	1.21	0.96
200 : 400	2.19	0.12	+0.14/–0.12	1.23	0.95
400 : 1000	0.28	0.03	+0.04/–0.04	1.24	0.87
x	$\mathrm{d}\sigma/\mathrm{d}x$ (pb)	Δ_{stat} (pb)	Δ_{sys} (pb)	$\mathrm{C_{had}}$	$\mathrm{C_{rad}}$
0.00008 : 0.0002	29325000	1825000	+2050000/–1750000	1.86	0.96
0.0002 : 0.0006	31897500	737500	+1720000/–1370000	1.46	0.98
0.0006 : 0.0016	10852000	217000	+581000/–532000	1.20	0.99
0.0016 : 0.005	1952647	41176	+119118/–109706	1.02	0.99
0.005 : 0.01	332400	12200	+26400/–24200	0.95	1.00
0.01 : 0.1	9967	611	+978/–900	0.91	0.88

Table A.1: Table of differential jet cross sections in charm events as a function of the photon virtuality Q^2, and Bjorken scaling variable x. The values refer to the measurement performed in the kinematic range $5 < Q^2 < 1000\,\mathrm{GeV}^2$, $0.02 < y < 0.7$, $E_T^{\mathrm{jet}} > 2.5\,\mathrm{GeV}$ and $-1.6 < \eta^{\mathrm{jet}} < 2.2$ using a combination of secondary vertexing and tracking information.

$E_T^{\rm jet}$ (GeV)	$\mathrm{d}\sigma/\mathrm{d}E_T^{\rm jet}$ (pb/GeV)	$\Delta_{\rm stat}$ (pb/GeV)	$\Delta_{\rm sys}$ (pb/GeV)	$\mathrm{C_{had}}$	$\mathrm{C_{rad}}$
2.5 : 8	5083	123	+286/–258	1.25	0.98
8 : 11	723	17	+67/–61	1.12	0.97
11 : 14	223	7.67	+23.00/–25.67	1.09	0.96
14 : 17	89	4.67	+11.67/–10.67	1.07	0.93
17 : 20	40.67	3.33	+6.33/–6.67	1.06	0.93
20 : 25	15.80	1.80	+3.80/–3.20	1.04	0.85
25 : 35	3.50	0.60	+1.30/–1.40	0.99	0.88
$\eta^{\rm jet}$	$\mathrm{d}\sigma/\mathrm{d}\eta^{\rm jet}$ (pb)	$\Delta_{\rm stat}$ (pb)	$\Delta_{\rm sys}$ (pb)	$\mathrm{C_{had}}$	$\mathrm{C_{rad}}$
–1.6 : -1.1	3844	384	+438/–410	0.91	0.99
–1.1 : -0.8	7323	327	+507/–477	0.98	0.98
–0.8 : -0.5	8620	287	+497/–460	1.03	0.98
–0.5 : -0.2	9677	273	+530/–497	1.07	0.98
–0.2 : 0.1	10293	297	+783/–763	1.12	0.98
0.1 : 0.4	11007	307	+830/–803	1.19	0.98
0.4 : 0.7	11363	337	+750/–727	1.27	0.98
0.7 : 1.0	11930	380	+683/–653	1.36	0.98
1.0 : 1.3	11590	457	+790/–760	1.44	0.98
1.3 : 1.6	10040	580	+703/–637	1.62	0.97
1.6 : 2.2	8563	677	+1378/–1375	2.22	0.97

Table A.2: Table of differential jet cross sections in charm events as a function of the pseudorapidity η^{jet}, and transverse jet energy $E_T^{\rm jet}$. The values refer to the measurement performed in the kinematic range $5 < Q^2 < 1000\,\mathrm{GeV}^2$, $0.02 < y < 0.7$, $E_T^{\rm jet} > 2.5$ GeV and $-1.6 < \eta^{\rm jet} < 2.2$ using a combination of secondary vertexing and tracking information.

$5 < Q^2 < 20$ GeV^2					
x	$\mathrm{d}\sigma/\mathrm{d}x$[pb]	Δ_{stat}[pb]	Δ_{sys}[pb]	$\mathrm{C_{had}}$	$\mathrm{C_{rad}}$
0.00008 : 0.0002	29325000	1825000	+2008333/–1600000	1.86	0.96
0.0002 : 0.0003	40440000	1820000	+2720000/–2250000	1.59	0.98
0.0003 : 0.0005	28075000	975000	+1850000/–1605000	1.41	0.98
0.0005 : 0.003	4316400	110800	+266400/–230800	1.08	1.00
$20 < Q^2 < 60$ GeV^2					
x	$\mathrm{d}\sigma/\mathrm{d}x$[pb]	Δ_{stat}[pb]	Δ_{sys}[pb]	$\mathrm{C_{had}}$	$\mathrm{C_{rad}}$
0.0003 : 0.0005	3385000	315000	+275000/–225000	1.80	0.97
0.0005 : 0.0012	4555714	145714	+248571/–221429	1.43	0.97
0.0012 : 0.0020	2142500	82500	+122500/–116250	1.21	0.98
0.0020 : 0.0035	881333	38667	+67333/–64667	1.11	0.99
0.0035 : 0.01	200769	13231	+15077/–14308	0.94	0.99
$60 < Q^2 < 120$ GeV^2					
x	$\mathrm{d}\sigma/\mathrm{d}x$[pb]	Δ_{stat}[pb]	Δ_{sys}[pb]	$\mathrm{C_{had}}$	$\mathrm{C_{rad}}$
0.0008 : 0.0018	494000	35000	+63000/–63000	1.59	0.97
0.0018 : 0.003	409167	23333	+32500/–30833	1.31	0.99
0.003 : 0.006	185000	8667	+14667/–14000	1.17	0.98
0.006 : 0.04	14324	1147	+1294/–1206	0.96	0.93
$120 < Q^2 < 400$ GeV^2					
x	$\mathrm{d}\sigma/\mathrm{d}x$[pb]	Δ_{stat}[pb]	Δ_{sys}[pb]	$\mathrm{C_{had}}$	$\mathrm{C_{rad}}$
0.0016 : 0.0050	141765	7353	+9706/–7353	1.41	0.97
0.0050 : 0.016	42818	2182	+2727/–2545	1.20	1.00
0.016 : 0.06	4159	591	+591/–568	0.98	0.80
$400 < Q^2 < 1000$ GeV^2					
x	$\mathrm{d}\sigma/\mathrm{d}x$[pb]	Δ_{stat}[pb]	Δ_{sys}[pb]	$\mathrm{C_{had}}$	$\mathrm{C_{rad}}$
0.005 : 0.02	7467	733	+1067/–933	1.33	0.88
0.02 : 0.1	763	163	+213/–213	1.11	0.84

Table A.3: Table of differential jet cross sections in charm events as a function of the Bjorken scaling variable x for different values of photon virtuality Q^2. The values refer to the measurement performed in the kinematic range $5 < Q^2 < 1000\,\mathrm{GeV}^2$, $0.02 < y < 0.7$, $E_T^{\mathrm{jet}} > 2.5\,\mathrm{GeV}$ and $-1.6 < \eta^{\mathrm{jet}} < 2.2$ using a combination of secondary vertexing and tracking information.

Appendix B

The Charm Contribution to the Proton Structure Function

Q^2	x	$F_2^{c\bar{c}}$	Δ_{stat}	Δ_{sys}	Δ_{extr}	$\mathcal{F}$
6.5	0.00015	0.232	0.015	+0.016/-0.013	+0.028/-0.018	1.89
6.5	0.00028	0.242	0.012	+0.016/-0.013	+0.018/-0.013	2.10
12	0.00043	0.321	0.012	+0.021/-0.018	+0.019/-0.014	1.98
12	0.00065	0.209	0.004	+0.013/-0.011	+0.007/-0.008	1.37
25	0.00043	0.534	0.039	+0.044/-0.036	+0.043/-0.023	2.29
25	0.0008	0.388	0.014	+0.021/-0.019	+0.016/-0.013	1.87
30	0.0016	0.275	0.012	+0.016/-0.015	+0.011/-0.007	1.43
30	0.0025	0.208	0.009	+0.016/-0.015	+0.005/-0.005	1.22
30	0.0045	0.163	0.007	+0.012/-0.012	+0.002/-0.007	0.97
80	0.0016	0.491	0.033	+0.062/-0.063	+0.019/-0.010	2.02
80	0.0025	0.323	0.021	+0.025/-0.024	+0.005/-0.006	1.49
80	0.0045	0.227	0.014	+0.018/-0.017	+0.006/-0.003	1.26
80	0.008	0.137	0.009	+0.012/-0.011	+0.003/-0.003	0.98
160	0.0035	0.351	0.023	+0.024/-0.018	+0.007/-0.005	1.68
16	0.008	0.200	0.013	+0.013/-0.012	+0.005/-0.004	1.31
16	0.02	0.096	0.014	+0.013/-0.013	+0.002/-0.001	1.10
600	0.013	0.192	0.025	+0.027/-0.025	+0.003/-0.004	1.64
600	0.035	0.069	0.018	+0.019/-0.019	+0.001/-0.001	1.20

Table B.1: The charm contribution, $F_2^{c\bar{c}}$ to the structure function of the proton for given values of Q^2 and x. The values were extracted from double differential cross sections measured using the combined secondary vertexing and tracking technique. The extrapolation factor, $\mathcal{F}$, is quoted for each $Q^2 - x$ bin. The statistical, Δ_{stat}, systematic, Δ_{sys}, and extrapolation, Δ_{extr}, uncertainty of $F_2^{c\bar{c}}$ are quoted separately.

Appendix C

Systematic Uncertainties

$d\sigma/dQ^2$							
bin	BR	BF	FF	DIS (E_e)	DIS (y_{el})	DIS (E-p_z)	EM
1	0.0231	0.0000	0.0090	0.0096	0.0080	0.0107	0.0040
2	0.0261	0.0139	0.0084	0.0098	0.0095	0.0171	0.0007
3	0.0299	0.0084	0.0104	0.0006	0.0038	0.0077	0.0010
4	0.0308	0.0160	0.0097	0.0020	0.0012	0.0007	0.0047
5	0.0204	0.0236	0.0088	0.0020	0.0123	0.0062	0.0032
6	0.0323	0.0284	0.0069	0.0027	0.0065	0.0011	0.0090
7	0.0278	0.0277	0.0084	0.0089	0.0025	0.0015	0.0020
8	0.0417	0.0414	0.0109	0.0491	0.0643	0.0032	0.0317
bin	E_T^{jet}	Q^2	LF	Sig Ex	Trk Eff	δ (imp)	δ (vtx)
1	0.0044	0.0009	0.0186	0.0099	0.0146	0.0020	0.0120
2	0.0037	0.0003	0.0119	0.0148	0.0147	0.0072	0.0154
3	0.0015	0.0009	0.0149	0.0142	0.0210	0.0054	0.0122
4	0.0006	0.0008	0.0260	0.0070	0.0151	0.0000	0.0153
5	0.0009	0.0003	0.0330	0.0199	0.0321	0.0023	0.0140
6	0.0007	0.0003	0.0234	0.0282	0.0178	0.0101	0.0047
7	0.0013	0.0005	0.0167	0.0090	0.0280	0.0206	0.0118
8	0.0009	0.0002	0.0556	0.0365	0.0319	0.0118	0.0197

Table C.1: Relative systematic uncertainties for the single differential cross section as function of Q^2. The table quotes results of upward variations of the following sources of systematic uncertainties: branching ratios (BR), fragmentation fractions (BF), the fragmentation function (FF), the DIS selection (E_e, y_{el}, E-p_z), the electromagnetic energy scale (EM), the calorimeter scale (E_T^{jet}), the Q^2 reweighting (Q^2), the light flavour asymmetry (LF), the signal extraction (Sig Ex), the tracking inefficiency (Trk Eff), the impact parameter smearing (δ(imp)) and the decay length smearing (δ(vtx)).

$d\sigma/dQ^2$							
bin	BR	BF	FF	DIS (E_e)	DIS (y_{el})	DIS (E-p_z)	EM
1	–0.0231	–0.0011	–0.0090	–0.0096	–0.0080	–0.0107	–0.0040
2	–0.0261	0.0000	–0.0084	–0.0098	–0.0095	–0.0171	–0.0007
3	–0.0299	0.0000	–0.0104	–0.0006	–0.0038	–0.0077	–0.0010
4	–0.0308	0.0000	–0.0097	–0.0020	–0.0012	–0.0007	–0.0047
5	–0.0204	0.0000	–0.0088	–0.0020	–0.0123	–0.0062	–0.0032
6	–0.0323	0.0000	–0.0069	–0.0027	–0.0065	–0.0011	–0.0090
7	–0.0278	0.0000	–0.0084	–0.0089	–0.0025	–0.0015	–0.0020
8	–0.0417	0.0000	–0.0109	–0.0491	–0.0643	–0.0032	–0.0317
bin	E_T^{jet}	Q^2	LF	Sig Ex	Trk Eff	δ (imp)	δ (vtx)
1	–0.0072	–0.0011	–0.0186	–0.0099	–0.0146	–0.0020	–0.0120
2	–0.0034	–0.0003	–0.0119	–0.0148	–0.0147	–0.0072	–0.0154
3	–0.0038	–0.0010	–0.0149	–0.0142	–0.0210	–0.0054	–0.0122
4	–0.0029	–0.0009	–0.0260	–0.0070	–0.0151	0.0000	–0.0153
5	–0.0021	–0.0002	–0.0330	–0.0199	–0.0321	–0.0023	–0.0140
6	–0.0020	–0.0002	–0.0234	–0.0282	–0.0178	–0.0101	–0.0047
7	–0.0036	–0.0006	–0.0167	–0.0090	–0.0280	–0.0206	–0.0118
8	–0.0011	0.0000	–0.0556	–0.0365	–0.0319	–0.0118	–0.0197

Table C.2: Relative systematic uncertainties for the single differential cross section as function of Q^2. The table quotes results of downward variations of the following sources of systematic uncertainties: branching ratios (BR), fragmentation fractions (BF), the fragmentation function (FF), the DIS selection (E_e, y_{el}, E-p_z), the electromagnetic energy scale (EM), the calorimeter scale (E_T^{jet}), the Q^2 reweighting (Q^2), the light flavour asymmetry (LF), the signal extraction (Sig Ex), the tracking inefficiency (Trk Eff), the impact parameter smearing (δ(imp)) and the decay length smearing (δ(vtx)).

$d\sigma/dx$							
bin	BR	BF	FF	DIS (E_e)	DIS (y_{el})	DIS (E-p_z)	EM
1	0.0295	0.0068	0.0116	0.0157	0.0191	0.0219	0.0039
2	0.0229	0.0026	0.0094	0.0129	0.0058	0.0072	0.0037
3	0.0294	0.0079	0.0094	0.0022	0.0060	0.0055	0.0009
4	0.0296	0.0129	0.0088	0.0007	0.0046	0.0080	0.0006
5	0.0243	0.0118	0.0093	0.0028	0.0128	0.0026	0.0034
6	0.0314	0.0118	0.0085	0.0033	0.0231	0.0261	0.0039
bin	E_T^{jet}	Q^2	LF	Sig Ex	Trk Eff	δ (imp)	δ (vtx)
1	0.0054	0.0001	0.0052	0.0205	0.0135	0.0110	0.0203
2	0.0026	0.0007	0.0115	0.0033	0.0155	0.0079	0.0130
3	0.0024	0.0024	0.0189	0.0145	0.0172	0.0071	0.0129
4	0.0012	0.0119	0.0202	0.0174	0.0259	0.0034	0.0121
5	0.0003	0.0322	0.0346	0.0121	0.0371	0.0019	0.0098
6	0.0003	0.0358	0.0371	0.0070	0.0475	0.0135	0.0141
$d\sigma/dx$							
bin	BR	BF	FF	DIS (E_e)	DIS (y_{el})	DIS (E-p_z)	EM
1	–0.0295	0.0000	–0.0116	–0.0157	–0.0191	–0.0219	–0.0039
2	–0.0229	0.0000	–0.0094	–0.0129	–0.0058	–0.0072	–0.0037
3	–0.0294	0.0000	–0.0094	–0.0022	–0.0060	–0.0055	–0.0009
4	–0.0296	0.0000	–0.0088	–0.0007	–0.0046	–0.0080	–0.0006
5	–0.0243	0.0000	–0.0093	–0.0028	–0.0128	–0.0026	–0.0034
6	–0.0314	0.0000	–0.0085	–0.0033	–0.0231	–0.0261	–0.0039
bin	E_T^{jet}	Q^2	LF	Sig Ex	Trk Eff	δ (imp)	δ (vtx)
1	–0.0038	–0.0001	–0.0052	–0.0205	–0.0135	–0.0110	–0.0203
2	–0.0049	–0.0010	–0.0115	–0.0033	–0.0155	–0.0079	–0.0130
3	0.0000	–0.0029	–0.0189	–0.0145	–0.0172	–0.0071	–0.0129
4	–0.0032	–0.0126	–0.0202	–0.0174	–0.0259	–0.0034	–0.0121
5	–0.0067	–0.0302	–0.0346	–0.0121	–0.0371	–0.0019	–0.0098
6	–0.0033	–0.0301	–0.0371	–0.0070	–0.0475	–0.0135	–0.0141

Table C.3: Relative systematic uncertainties for the single differential cross section as function of Bjorken x. The table quotes results of upward and downward variations of the following sources of systematic uncertainties: branching ratios (BR), fragmentation fractions (BF), the fragmentation function (FF), the DIS selection (E_e, y_{el}, E-p_z), the electromagnetic energy scale (EM), the calorimeter scale (E_T^{jet}), the Q^2 reweighting (Q^2), the light flavour asymmetry (LF), the signal extraction (Sig Ex), the tracking inefficiency (Trk Eff), the impact parameter smearing (δ(imp)) and the decay length smearing (δ(vtx)).

$d\sigma/dE_T^{jet}$							
bin	BR	BF	FF	DIS (E_e)	DIS (y_{el})	DIS (E-p_z)	EM
1	0.0260	0.0165	0.0071	0.0006	0.0015	0.0076	0.0012
2	0.0285	0.0169	0.0080	0.0054	0.0070	0.0181	0.0019
3	0.0284	0.0217	0.0075	0.0066	0.0025	0.0119	0.0013
4	0.0363	0.0502	0.0066	0.0038	0.0050	0.0097	0.0085
5	0.0339	0.0272	0.0070	0.0383	0.0237	0.0178	0.0010
6	0.1284	0.0854	0.0027	0.0631	0.0360	0.0265	0.0067
7	0.2744	0.0000	0.0198	0.0880	0.0776	0.0396	0.0143
bin	E_T^{jet}	Q^2	LF	Sig Ex	Trk Eff	δ (imp)	δ (vtx)
1	0.0059	0.0096	0.0198	0.0263	0.0073	0.0086	0.0184
2	0.0778	0.0015	0.0137	0.0066	0.0189	0.0070	0.0127
3	0.0853	0.0062	0.0214	0.0241	0.0133	0.0062	0.0114
4	0.1076	0.0067	0.0048	0.0125	0.0157	0.0092	0.0163
5	0.1159	0.0110	0.0185	0.0593	0.0137	0.0022	0.0240
6	0.1427	0.0098	0.0588	0.0045	0.0097	0.0132	0.0636
7	0.2051	0.0051	0.0503	0.0924	0.0418	0.0176	0.0354
$d\sigma/dE_T^{jet}$							
bin	BR	BF	FF	DIS (E_e)	DIS (y_{el})	DIS (E-p_z)	EM
1	–0.0260	0.0000	–0.0071	–0.0006	–0.0015	–0.0076	–0.0012
2	–0.0285	0.0000	–0.0080	–0.0054	–0.0070	–0.0181	–0.0019
3	–0.0284	0.0000	–0.0075	–0.0066	–0.0025	–0.0119	–0.0013
4	–0.0363	0.0000	–0.0066	–0.0038	–0.0050	–0.0097	–0.0085
5	–0.0339	0.0000	–0.0070	–0.0383	–0.0237	–0.0178	–0.0010
6	–0.1284	0.0000	–0.0027	–0.0631	–0.0360	–0.0265	–0.0067
7	–0.2744	–0.0532	–0.0198	–0.0880	–0.0776	–0.0396	–0.0143
bin	E_T^{jet}	Q^2	LF	Sig Ex	Trk Eff	δ (imp)	δ (vtx)
1	–0.0015	–0.0111	–0.0198	–0.0263	–0.0073	–0.0086	–0.0184
2	–0.0706	–0.0016	–0.0137	–0.0066	–0.0189	–0.0070	–0.0127
3	–0.1035	–0.0062	–0.0214	–0.0241	–0.0133	–0.0062	–0.0114
4	–0.1078	–0.0072	–0.0048	–0.0125	–0.0157	–0.0092	–0.0163
5	–0.1409	–0.0125	–0.0185	–0.0593	–0.0137	–0.0022	–0.0240
6	–0.1111	–0.0124	–0.0588	–0.0045	–0.0097	–0.0132	–0.0636
7	–0.2412	–0.0050	–0.0503	–0.0924	–0.0418	–0.0176	–0.0354

Table C.4: Relative systematic uncertainties for the single differential cross section as function of E_T^{jet}. The table quotes results of upward and downward variations of the following sources of systematic uncertainties: branching ratios (BR), fragmentation fractions (BF), the fragmentation function (FF), the DIS selection (E_e, y_{el}, E-p_z), the electromagnetic energy scale (EM), the calorimeter scale (E_T^{jet}), the Q^2 reweighting (Q^2), the light flavour asymmetry (LF), the signal extraction (Sig Ex), the tracking inefficiency (Trk Eff), the impact parameter smearing (δ(imp)) and the decay length smearing (δ(vtx)).

$d\sigma/d\eta^{jet}$							
bin	BR	BF	FF	DIS (E_e)	DIS (y_{el})	DIS (E-p_z)	EM
1	0.0414	0.0214	0.0084	0.0206	0.0077	0.0489	0.0057
2	0.0257	0.0150	0.0105	0.0283	0.0025	0.0036	0.0027
3	0.0238	0.0032	0.0094	0.0045	0.0013	0.0042	0.0022
4	0.0264	0.0039	0.0089	0.0011	0.0069	0.0011	0.0060
5	0.0295	0.0027	0.0093	0.0197	0.0046	0.0043	0.0004
6	0.0357	0.0093	0.0094	0.0033	0.0093	0.0168	0.0002
7	0.0277	0.0086	0.0087	0.0020	0.0014	0.0116	0.0013
8	0.0257	0.0059	0.0080	0.0072	0.0041	0.0045	0.0063
9	0.0253	0.0116	0.0092	0.0013	0.0100	0.0139	0.0089
10	0.0296	0.0256	0.0097	0.0218	0.0100	0.012	0.0061
11	0.0355	0.0000	0.0091	0.0128	0.0852	0.0346	0.0064
bin	E_T^{jet}	Q^2	LF	Sig Ex	Trk Eff	δ (imp)	δ (vtx)
1	0.0349	0.0053	0.0145	0.0449	0.0541	0.0053	0.0350
2	0.0026	0.0115	0.0204	0.0313	0.0240	0.0019	0.0193
3	0.0001	0.0189	0.0183	0.0054	0.0261	0.0149	0.0156
4	0.0003	0.0222	0.0057	0.0094	0.0252	0.0007	0.0116
5	0.0012	0.0235	0.0157	0.0391	0.0319	0.0096	0.0144
6	0.0013	0.0243	0.0241	0.0215	0.0321	0.0152	0.0126
7	0.0011	0.0238	0.0253	0.0169	0.0295	0.0086	0.0095
8	0.0033	0.0185	0.0224	0.0010	0.0246	0.0057	0.0120
9	0.0022	0.0191	0.0303	0.0128	0.0209	0.0231	0.0130
10	0.0004	0.0159	0.0107	0.0157	0.0219	0.0187	0.0109
11	0.0045	0.0099	0.0228	0.0728	0.0053	0.0934	0.0309

Table C.5: Relative systematic uncertainties for the single differential cross section as function of η^{jet}. The table quotes results of upward variations of the following sources of systematic uncertainties: branching ratios (BR), fragmentation fractions (BF), the fragmentation function (FF), the DIS selection (E_e, y_{el}, E-p_z), the electromagnetic energy scale (EM), the calorimeter scale (E_T^{jet}), the Q^2 reweighting (Q^2), the light flavour asymmetry (LF), the signal extraction (Sig Ex), the tracking inefficiency (Trk Eff), the impact parameter smearing (δ(imp)) and the decay length smearing (δ(vtx)).

$d\sigma/d\eta^{jet}$							
bin	BR	BF	FF	DIS (E_e)	DIS (y_{el})	DIS (E-p_z)	EM
1	–0.0414	0.0000	–0.0084	–0.0206	–0.0077	–0.0489	–0.0057
2	–0.0257	0.0000	–0.0105	–0.0283	–0.0025	–0.0036	–0.0027
3	–0.0238	0.0000	–0.0094	–0.0045	–0.0013	–0.0042	–0.0022
4	–0.0264	0.0000	–0.0089	–0.0011	–0.0069	–0.0011	–0.0060
5	–0.0295	0.0000	–0.0093	–0.0197	–0.0046	–0.0043	–0.0004
6	–0.0357	0.0000	–0.0094	–0.0033	–0.0092	–0.0168	–0.0002
7	–0.0277	0.0000	–0.0087	–0.0020	–0.0014	–0.0116	–0.0013
8	–0.0257	0.0000	–0.0080	–0.0072	–0.0041	–0.0045	–0.0063
9	–0.0253	0.0000	–0.0092	–0.0013	–0.0100	–0.0139	–0.0089
10	–0.0296	0.0000	–0.0097	–0.0218	–0.0100	–0.0212	–0.0061
11	–0.0355	–0.0021	–0.0091	–0.0128	–0.0852	–0.0346	–0.0064
bin	E_T^{jet}	Q^2	LF	Sig Ex	Trk Eff	δ (imp)	δ (vtx)
1	–0.0135	–0.0063	–0.0145	–0.0449	–0.0541	–0.0053	–0.0350
2	–0.0010	–0.0130	–0.0204	–0.0313	–0.0240	–0.0019	–0.0193
3	–0.0017	–0.0214	–0.0183	–0.0054	–0.0261	–0.0149	–0.0156
4	–0.0029	–0.0248	–0.0057	–0.0094	–0.0252	–0.0007	–0.0116
5	–0.0027	–0.0263	–0.0157	–0.0391	–0.0319	–0.0096	–0.0144
6	–0.0022	–0.0271	–0.0241	–0.0215	–0.0321	–0.0152	–0.0126
7	–0.0046	–0.0264	–0.0253	–0.0169	–0.0295	–0.0086	–0.0095
8	–0.0054	–0.0208	–0.0224	–0.0010	–0.0246	–0.0057	–0.0120
9	–0.0060	–0.0215	–0.0303	–0.0128	–0.0209	–0.0231	–0.0130
10	–0.0005	–0.0179	–0.0107	–0.0157	–0.0219	–0.0187	–0.0109
11	–0.0035	–0.0116	–0.0228	–0.0728	–0.0053	–0.0934	–0.0309

Table C.6: Relative systematic uncertainties for the single differential cross section as function of η^{jet}. The table quotes results of downward variations of the following sources of systematic uncertainties: branching ratios (BR), fragmentation fractions (BF), the fragmentation function (FF), the DIS selection (E_e, y_{el}, E-p_z), the electromagnetic energy scale (EM), the calorimeter scale (E_T^{jet}), the Q^2 reweighting (Q^2), the light flavour asymmetry (LF), the signal extraction (Sig Ex), the tracking inefficiency (Trk Eff), the impact parameter smearing (δ(imp)) and the decay length smearing (δ(vtx)).

$5 < Q^2 < 20$ GeV^2							
bin	BR	BF	FF	DIS (E_e)	DIS (y_{el})	DIS (E-p_z)	EM
1	0.0264	0.0068	0.0089	0.0157	0.0191	0.0219	0.0039
2	0.0194	0.0050	0.0113	0.0331	0.0105	0.0012	0.0057
3	0.0314	0.0000	0.0109	0.0043	0.0209	0.0134	0.0082
4	0.0289	0.0111	0.0109	0.0087	0.0010	0.0142	0.0021
bin	E_T^{jet}	Q^2	LF	Sig Ex	Trk Eff	δ (imp)	δ (vtx)
1	0.0054	-0.0001	0.0052	0.0205	0.0135	0.0110	0.0203
2	0.0018	-0.0003	0.0068	0.0208	0.0180	0.0053	0.0147
3	0.0032	-0.0014	0.0157	0.0176	0.0159	0.0088	0.0099
4	0.0056	-0.0020	0.0190	0.0283	0.0129	0.0050	0.0132
bin	BR	BF	FF	DIS (E_e)	DIS (y_{el})	DIS (E-p_z)	EM
1	–0.0192	0.0000	–0.0083	–0.0157	–0.0191	–0.0219	–0.0039
2	–0.0178	0.0000	–0.0110	–0.0331	–0.0105	–0.0012	–0.0057
3	–0.0324	–0.0106	–0.0113	–0.0043	–0.0209	–0.0134	–0.0082
4	–0.0241	0.0000	–0.0104	–0.0087	–0.0010	–0.0142	–0.0021
bin	E_T^{jet}	Q^2	LF	Sig Ex	Trk Eff	δ (imp)	δ (vtx)
1	–0.0038	0.0001	–0.0052	–0.0205	–0.0135	–0.0110	–0.0203
2	–0.0076	0.0002	–0.0068	–0.0208	–0.0180	–0.0053	–0.0147
3	–0.0008	0.0011	–0.0157	–0.0176	–0.0159	–0.0088	–0.0099
4	–0.0049	0.0016	–0.0190	–0.0283	–0.0129	–0.0050	–0.0132

Table C.7: Relative systematic uncertainties for the single differential cross section as function of Bjorken x for the photon virtuality $5 < Q^2 < 20\,\text{GeV}^2$. The table quotes results of upward and downward variations of the following sources of systematic uncertainties: branching ratios (BR), fragmentation fractions (BF), the fragmentation function (FF), the DIS selection (E_e, y_{el}, E-p_z), the electromagnetic energy scale (EM), the calorimeter scale (E_T^{jet}), the Q^2 reweighting (Q^2), the light flavour asymmetry (LF), the signal extraction (Sig Ex), the tracking inefficiency (Trk Eff), the impact parameter smearing (δ(imp)) and the decay length smearing (δ(vtx)).

$20 < Q^2 < 60\,\mathrm{GeV}^2$							
bin	BR	BF	FF	DIS (E_e)	DIS (y_{el})	DIS (E-p_z)	EM
1	0.0518	0.0099	0.0152	0.0245	0.0013	0.0112	0.0216
2	0.0290	0.0107	0.0107	0.0029	0.0034	0.0093	0.0022
3	0.0346	0.0079	0.0100	0.0043	0.0171	0.0142	0.0009
4	0.0353	0.0023	0.0109	0.0106	0.0244	0.0078	0.0035
5	0.0300	0.0230	0.0115	0.0227	0.0024	0.0180	0.0016
bin	E_T^{jet}	Q^2	LF	Sig Ex	Trk Eff	δ (imp)	δ (vtx)
1	0.0014	0.0013	0.0196	0.0005	0.0038	0.0274	0.0250
2	0.0009	0.0014	0.0174	0.0195	0.0146	0.0104	0.0134
3	0.0010	0.0017	0.0085	0.0108	0.0237	0.0089	0.0142
4	0.0023	0.0035	0.0232	0.0453	0.0233	0.0042	0.0150
5	0.0009	0.0065	0.0343	0.0297	0.0139	0.0141	0.0051
bin	BR	BF	FF	DIS (E_e)	DIS (y_{el})	DIS (E-p_z)	EM
1	–0.0306	0.0000	–0.0145	–0.0245	–0.0013	–0.0112	–0.0216
2	–0.0259	0.0000	–0.0112	–0.0029	–0.0034	–0.0093	–0.0022
3	–0.0334	0.0000	–0.0106	–0.0043	–0.0171	–0.0142	–0.0009
4	–0.0298	0.0000	–0.0110	–0.0106	–0.0244	–0.0078	–0.0035
5	–0.0335	0.0000	–0.0123	–0.0227	–0.0024	–0.0180	–0.0016
bin	E_T^{jet}	Q^2	LF	Sig Ex	Trk Eff	δ (imp)	δ (vtx)
1	–0.0020	–0.0009	–0.0196	–0.0005	–0.0038	–0.0274	–0.0250
2	–0.0014	–0.0011	–0.0174	–0.0195	–0.0146	–0.0104	–0.0134
3	–0.0026	–0.0019	–0.0085	–0.0108	–0.0237	–0.0089	–0.0142
4	–0.0033	–0.0039	–0.0232	–0.0453	–0.0233	–0.0042	–0.0150
5	–0.0122	–0.0071	–0.0343	–0.0297	–0.0139	–0.0141	–0.0051

Table C.8: Relative systematic uncertainties for the single differential cross section as function of Bjorken x for the photon virtuality $20 < Q^2 < 60\,\mathrm{GeV}^2$. The table quotes results of upward and downward variations of the following sources of systematic uncertainties: branching ratios (BR), fragmentation fractions (BF), the fragmentation function (FF), the DIS selection (E_e, y_{el}, E-p_z), the electromagnetic energy scale (EM), the calorimeter scale (E_T^{jet}), the Q^2 reweighting (Q^2), the light flavour asymmetry (LF), the signal extraction (Sig Ex), the tracking inefficiency (Trk Eff), the impact parameter smearing (δ(imp)) and the decay length smearing (δ(vtx)).

$60 < Q^2 < 120$ GeV^2							
bin	BR	BF	FF	DIS (E_e)	DIS (y_{el})	DIS (E-p_z)	EM
1	0.0265	0.0091	0.0096	0.0753	0.0025	0.0507	0.0204
2	0.0234	0.0303	0.0096	0.0196	0.0016	0.0220	0.0100
3	0.0199	0.0176	0.0093	0.0120	0.0074	0.0256	0.0097
4	0.0319	0.0158	0.0097	0.0072	0.0348	0.0323	0.0001
bin	E_T^{jet}	Q^2	LF	Sig Ex	Trk Eff	δ (imp)	δ (vtx)
1	0.0006	0.0013	0.0719	0.0086	0.0129	0.0102	0.0216
2	0.0007	0.0014	0.0175	0.0467	0.0184	0.0183	0.0127
3	0.0011	0.0002	0.0293	0.0456	0.0314	0.0015	0.0162
4	0.0023	0.0034	0.0311	0.0158	0.0411	0.0099	0.0292
bin	BR	BF	FF	DIS (E_e)	DIS (y_{el})	DIS (E-p_z)	EM
1	–0.0360	0.0000	–0.0102	–0.0753	–0.0025	–0.0507	–0.0204
2	–0.0349	0.0000	–0.0092	–0.0196	–0.0016	–0.0220	–0.0100
3	–0.0188	0.0000	–0.0110	–0.0120	–0.0074	–0.0256	–0.0097
4	–0.0193	0.0000	–0.0098	–0.0072	–0.0348	–0.0323	–0.0001
bin	E_T^{jet}	Q^2	LF	Sig Ex	Trk Eff	δ (imp)	δ (vtx)
1	–0.0025	–0.0012	–0.0719	–0.0086	–0.0129	–0.0102	–0.0216
2	–0.0007	–0.0015	–0.0175	–0.0467	–0.0184	–0.0183	–0.0127
3	–0.0001	–0.0002	–0.0293	–0.0456	–0.0314	–0.0015	–0.0162
4	–0.0094	–0.0030	–0.0311	–0.0158	–0.0411	–0.0099	–0.0292

Table C.9: Relative systematic uncertainties for the single differential cross section as function of Bjorken x for the photon virtuality $60 < Q^2 < 120\,\text{GeV}^2$. The table quotes results of upward and downward variations of the following sources of systematic uncertainties: branching ratios (BR), fragmentation fractions (BF), the fragmentation function (FF), the DIS selection (E_e, y_{el}, E-p_z), the electromagnetic energy scale (EM), the calorimeter scale (E_T^{jet}), the Q^2 reweighting (Q^2), the light flavour asymmetry (LF), the signal extraction (Sig Ex), the tracking inefficiency (Trk Eff), the impact parameter smearing (δ(imp)) and the decay length smearing (δ(vtx)).

$120 < Q^2 < 400$ GeV^2							
bin	BR	BF	FF	DIS (E_e)	DIS (y_{el})	DIS (E-p_z)	EM
1	0.0307	0.0473	0.0067	0.0004	0.0043	0.0094	0.0015
2	0.0240	0.0282	0.0078	0.0050	0.0005	0.0132	0.0006
3	0.0484	0.0000	0.0147	0.0731	0.0676	0.0343	0.0379
bin	E_T^{jet}	Q^2	LF	Sig Ex	Trk Eff	δ (imp)	δ (vtx)
1	0.0027	0.0008	0.0058	0.0159	0.0076	0.0153	0.0070
2	0.0027	0.0006	0.0223	0.0208	0.0271	0.0180	0.0097
3	0.0090	0.0066	0.0320	0.0148	0.0449	0.0034	0.0215
bin	BR	BF	FF	DIS (E_e)	DIS (y_{el})	DIS (E-p_z)	EM
1	–0.0396	0.0000	–0.0072	–0.0004	–0.0043	–0.0094	–0.0015
2	–0.0302	0.0000	–0.0092	–0.0050	–0.0005	–0.0132	–0.0006
3	–0.0386	–0.0106	–0.0156	–0.0731	–0.0676	–0.0343	–0.0379
bin	E_T^{jet}	Q^2	LF	Sig Ex	Trk Eff	δ (imp)	δ (vtx)
1	–0.0002	–0.0009	–0.0058	–0.0159	–0.0076	–0.0153	–0.0070
2	–0.0045	–0.0009	–0.0223	–0.0208	–0.0271	–0.0180	–0.0097
3	–0.0062	–0.0052	–0.0320	–0.0148	–0.0449	–0.0034	–0.0215
$400 < Q^2 < 1000$ GeV^2							
bin	BR	BF	FF	DIS (E_e)	DIS (y_{el})	DIS (E-p_z)	EM
1	0.0250	0.0630	0.0116	0.0359	0.0710	0.0219	0.0440
2	0.0642	0.0878	0.0030	0.0933	0.0559	0.1508	0.0336
bin	E_T^{jet}	Q^2	LF	Sig Ex	Trk Eff	δ (imp)	δ (vtx)
1	0.0000	0.0000	0.0256	0.0234	0.0209	0.0293	0.0273
2	0.0015	0.0001	0.1203	0.0463	0.0455	0.0158	0.0819
bin	BR	BF	FF	DIS (E_e)	DIS (y_{el})	DIS (E-p_z)	EM
1	–0.0645	0.0000	–0.0128	–0.0359	–0.0710	–0.0219	–0.0440
2	–0.1296	0.0000	–0.0035	–0.0933	–0.0559	–0.1508	–0.0336
bin	E_T^{jet}	Q^2	LF	Sig Ex	Trk Eff	δ (imp)	δ (vtx)
1	–0.0018	0.0000	–0.0256	–0.0234	–0.0209	–0.0293	–0.0273
2	–0.0012	0.0000	–0.1203	–0.0463	–0.0455	–0.0158	–0.0819

Table C.10: Relative systematic uncertainties for the single differential cross section as function of Bjorken x for the photon virtuality $120 < Q^2 < 400\,\text{GeV}^2$ and $400 < Q^2 < 1000\,\text{GeV}^2$. The table quotes results of upward and downward variations of the following sources of systematic uncertainties: branching ratios (BR), fragmentation fractions (BF), the fragmentation function (FF), the DIS selection (E_e, y_{el}, E-p_z), the electromagnetic energy scale (EM), the calorimeter scale (E_T^{jet}), the Q^2 reweighting (Q^2), the light flavour asymmetry (LF), the signal extraction (Sig Ex), the tracking inefficiency (Trk Eff), the impact parameter smearing (δ(imp)) and the decay length smearing (δ(vtx)).

List of Figures

List of Tables

Bibliography

[1] J. D. Bjorken and S. D. Drell. *Relativistic Quantum Fields.* McGraw-Hill, New York, USA, 1965.

[2] R. Devenish and A. Cooper-Sarkar. *Deep Inelastic Scattering.* Oxford University Press, Oxford, UK, 2004.

[3] C. Itzykson and J. B. Zuber. *Quantum Field Theory.* McGraw-Hill, New York, USA, 1980.

[4] G. F. Sterman. *An Introduction to quantum field theory.* Cambridge University Press, Cambridge, UK, 1994.

[5] M. E. Peskin and D. V. Schroeder. *An Introduction to quantum field theory.* Addison-Wesley, Reading, USA, 1995.

[6] S. Weinberg. *Quantum Theory of Fields*, volume 1. Cambridge University Press, Cambridge, 1995.

[7] S. Weinberg. *Quantum Theory of Fields*, volume 2. Cambridge University Press, Cambridge, 1995.

[8] R. K. Ellis, W. J. Stirling, and B. R. Webber. QCD and collider physics. *Camb.Monogr.Part.Phys.Nucl.Phys.Cosmol.*, 8:1–435, 1996.

[9] G. Altarelli. Partons in Quantum Chromodynamics. *Phys.Rept.*, 81:1, 1982.

[10] G. F. Sterman et al. Handbook of perturbative QCD: Version 1.0. *Rev.Mod.Phys.*, 67:157–248, 1995.

[11] Y. L. Dokshitzer, V. A. Khoze, A. H. Mueller, and S.I. Troian. *Basics of perturbative QCD.* Ed. Frontieres, Gif-sur-Yvette, France, 1991.

[12] D. W. Duke and R. G. Roberts. Determinations of the QCD Strong Coupling α_s and the Scale Lambda (QCD). *Phys.Rept.*, 120:275, 1985.

[13] J. D. Bjorken and E. A. Paschos. Inelastic Electron Proton and gamma Proton Scattering, and the Structure of the Nucleon. *Phys.Rev.*, 185:1975–1982, 1969.

[14] D. J. Gross and F. Wilczek. Ultraviolet Behavior of Nonabelian Gauge Theories. *Phys.Rev.Lett.*, 30:1343–1346, 1973.

[15] H. D. Politzer. Reliable Perturbative Results for Strong Interactions? *Phys.Rev.Lett.*, 30:1346–1349, 1973.

[16] G. 't Hooft and M. J. G. Veltman. Regularization and Renormalization of Gauge Fields. *Nucl.Phys.*, B44:189–213, 1972.

[17] J. C. Collins, Davison E. Soper, and G. F. Sterman. Factorization of Hard Processes in QCD. *Adv.Ser.Direct.High Energy Phys.*, 5:1–91, 1988.

[18] G. Altarelli and G. Parisi. Asymptotic Freedom in Parton Language. *Nucl.Phys.*, B126:298, 1977.

[19] Y. L. Dokshitzer. Calculation of the Structure Functions for Deep Inelastic Scattering and e+ e- Annihilation by Perturbation Theory in Quantum Chromodynamics. *Sov.Phys.JETP*, 46:641–653, 1977.

[20] V. N. Gribov and L. N. Lipatov. Deep inelastic e p scattering in perturbation theory. *Sov.J.Nucl.Phys.*, 15:438–450, 1972.

[21] L. N. Lipatov. The parton model and perturbation theory. *Sov.J.Nucl.Phys.*, 20:94–102, 1975.

[22] G. Ingelman and G. A. Schuler. Characteristics of heavy flavour production in ep collisions. *Z.Phys.*, C40:299, 1988.

[23] J. C. Collins and Wu-Ki Tung. Calculating Heavy Quark Distributions. *Nucl.Phys.*, B278:934, 1986.

[24] E. Laenen, S. Riemersma, J. Smith, and W. L. van Neerven. On the heavy quark content of the nucleon. *Phys.Lett.*, B291:325–328, 1992.

[25] E. Laenen, S. Riemersma, J. Smith, and W. L. van Neerven. O(alpha-s) corrections to heavy flavor inclusive distributions in electroproduction. *Nucl.Phys.*, B392:229–250, 1993.

[26] E. Laenen, S. Riemersma, J. Smith, and W. L. van Neerven. Complete O (alpha-s) corrections to heavy flavor structure functions in electroproduction. *Nucl.Phys.*, B392:162–228, 1993.

[27] S. Riemersma, J. Smith, and W. L. van Neerven. Rates for inclusive deep inelastic electroproduction of charm quarks at HERA. *Phys.Lett.*, B347:143–151, 1995.

[28] M. A. G. Aivazis, F. I. Olness, and Wu-Ki Tung. Leptoproduction of heavy quarks. 1. General formalism and kinematics of charged current and neutral current production processes. *Phys.Rev.*, D50:3085–3101, 1994.

[29] M. A. G. Aivazis, J. C. Collins, F. I. Olness, and Wu-Ki Tung. Leptoproduction of heavy quarks. 2. A Unified QCD formulation of charged and neutral current processes from fixed target to collider energies. *Phys.Rev.*, D50:3102–3118, 1994.

[30] F. I. Olness and S. T. Riemersma. Leptoproduction of heavy quarks in the fixed and variable flavor schemes. *Phys.Rev.*, D51:4746–4755, 1995.

[31] M. Buza, Y. Matiounine, J. Smith, R. Migneron, and W. L. van Neerven. Heavy quark coefficient functions at asymptotic values $Q^2 \gg m^2$. *Nucl.Phys.*, B472:611–658, 1996.

[32] J. C. Collins. Hard scattering factorization with heavy quarks: A General treatment. *Phys.Rev.*, D58:094002, 1998.

[33] M. Kramer, F. I. Olness, and D. E. Soper. Treatment of heavy quarks in deeply inelastic scattering. *Phys.Rev.*, D62:096007, 2000.

[34] R. S. Thorne and R. G. Roberts. An Ordered analysis of heavy flavor production in deep inelastic scattering. *Phys.Rev.*, D57:6871–6898, 1998.

[35] R. S. Thorne and R. G. Roberts. A Variable number flavor scheme for charged current heavy flavor structure functions. *Eur.Phys.J.*, C19:339–349, 2001.

[36] Wu-Ki Tung, S. Kretzer, and C. Schmidt. Open heavy flavor production in QCD: Conceptual framework and implementation issues. *J.Phys.*, G28:983–996, 2002.

[37] S. Forte, E. Laenen, P. Nason, and J. Rojo. Heavy quarks in deep-inelastic scattering. *Nucl.Phys.*, B834:116–162, 2010.

[38] R. S. Thorne. A Variable-flavor number scheme for NNLO. *Phys.Rev.*, D73:054019, 2006.

[39] R. D. Ball, V. Bertone, F. Cerutti, L. Del Debbio, S. Forte, et al. Impact of Heavy Quark Masses on Parton Distributions and LHC Phenomenology. *Nucl.Phys.*, B849:296–363, 2011.

[40] R. D. Ball et al. Unbiased global determination of parton distributions and their uncertainties at NNLO and at LO. *Nucl.Phys.*, B855:153–221, 2012.

[41] L.D. Faddeev and V.N. Popov. Feynman Diagrams for the Yang-Mills Field. *Phys.Lett.*, B25:29–30, 1967.

[42] J. D. Bjorken. Current algebra at small distances. *Conf.Proc.*, C670717:55–81, 1967.

[43] J. D. Bjorken. Asymptotic Sum Rules at Infinite Momentum. *Phys.Rev.*, 179:1547–1553, 1969.

[44] A. M. Cooper-Sarkar, R. C. E. Devenish, and A. De Roeck. Structure functions of the nucleon and their interpretation. *Int.J.Mod.Phys.*, A13:3385–3586, 1998.

[45] J. D. Bjorken. Inequality for Backward electron-Nucleon and Muon-Nucleon Scattering at High Momentum Transfer. *Phys.Rev.*, 163:1767–1769, 1967.

[46] Y. Gabellini, J. Kubar, J. l. Meunier, and G. Plaut. A study of QCD scaling violations by direct resolution of Altarelli-Parisi type equations. *Nucl.Phys.*, B211:509–528, 1983.

[47] C. Adloff et al. Inclusive D^0 and $D^{*\pm}$ production in deep inelastic e p scattering at HERA. *Z.Phys.*, C72:593–605, 1996.

[48] J. Breitweg et al. D^* production in deep inelastic scattering at HERA. *Phys.Lett.*, B407:402–418, 1997.

[49] J. Breitweg et al. Measurement of $D^{*\pm}$ production and the charm contribution to 2 in deep inelastic scattering at HERA. *Eur.Phys.J.*, C12:35–52, 2000.

[50] C. Adloff et al. Measurement of $D^{*\pm}$ meson production and $F_2^{c\bar{c}}$ in deep inelastic scattering at HERA. *Phys.Lett.*, B528:199–214, 2002.

[51] S. Chekanov et al. Measurement of $D^{*\pm}$ production in deep inelastic e–p scattering at HERA. *Phys.Rev.*, D69:012004, 2004.

[52] A. Aktas et al. Production of $D^{*\pm}$ Mesons with Dijets in Deep-Inelastic Scattering at HERA. *Eur.Phys.J.*, C51:271–287, 2007.

[53] S. Chekanov et al. Measurement of D mesons production in deep inelastic scattering at HERA. *JHEP*, 0707:074, 2007.

[54] S. Chekanov et al. Measurement of $D^{\pm}$ and D^0 production in deep inelastic scattering using a lifetime tag at HERA. *Eur.Phys.J.*, C63:171–188, 2009.

[55] F. D. Aaron et al. Measurement of the $D^{*\pm}$ Meson Production Cross Section and $F_2^{c\bar{c}}$, at High Q^2, in ep Scattering at HERA. *Phys.Lett.*, B686:91–100, 2010.

[56] F. D. Aaron et al. Measurement of $D^{*\pm}$ Meson Production and Determination of $F_2^{c\bar{c}}$ at low Q2 in Deep-Inelastic Scattering at HERA. *Eur.Phys.J.*, C71:1769, 2011.

[57] A. Aktas et al. Inclusive production of D^+, D^0, D_s^+ and D^{*+} mesons in deep inelastic scattering at HERA. *Eur.Phys.J.*, C38:447–459, 2005.

[58] A. Aktas et al. Measurement of $F_2^{c\bar{c}}$ and $F_2^{b\bar{b}}$ at high Q^2 using the H1 vertex detector at HERA. *Eur.Phys.J.*, C40:349–359, 2005.

[59] A. Aktas et al. Measurement of $F_2^{c\bar{c}}$ and $F_2^{b\bar{b}}$ at low Q^2 and x using the H1 vertex detector at HERA. *Eur.Phys.J.*, C45:23–33, 2006.

[60] F. D. Aaron et al. Measurement of the Charm and Beauty Structure Functions using the H1 Vertex Detector at HERA. *Eur.Phys.J.*, C65:89–109, 2010.

[61] S. Chekanov et al. Measurement of charm and beauty production in deep inelastic ep scattering from decays into muons at HERA. *Eur.Phys.J.*, C65:65–79, 2010.

[62] H. Abramowicz et al. Combination and QCD Analysis of Charm Production Cross Section Measurements in Deep-Inelastic ep Scattering at HERA. *Eur.Phys.J.*, C73:2311, 2013.

[63] A. Glazov. Averaging of DIS cross section data. *AIP Conf.Proc.*, 792:237–240, 2005.

[64] F. D. Aaron et al. Measurement of the Inclusive ep Scattering Cross Section at Low Q^2 and x at HERA. *Eur.Phys.J.*, C63:625–678, 2009.

[65] F. D. Aaron et al. Combined Measurement and QCD Analysis of the Inclusive e+- p Scattering Cross Sections at HERA. *JHEP*, 1001:109, 2010.

[66] S. Alekhin, J. Blumlein, S. Klein, and S. Moch. The 3, 4, and 5-flavor NNLO Parton from Deep-Inelastic-Scattering Data and at Hadron Colliders. *Phys.Rev.*, D81:014032, 2010.

[67] S. Alekhin and S.-O. Moch. Running Heavy-Quark Masses in DIS. 2011.

[68] S. Alekhin and S. Moch. Heavy-quark deep-inelastic scattering with a running mass. *Phys.Lett.*, B699:345–353, 2011.

[69] Serguei Chatrchyan et al. Measurement of the Inclusive W and Z Production Cross Sections in pp Collisions at $\sqrt{s} = 7$ TeV. *JHEP*, 1110:132, 2011.

[70] Vardan Khachatryan et al. Measurements of Inclusive W and Z Cross Sections in pp Collisions at $\sqrt{s} = 7$ TeV. *JHEP*, 1101:080, 2011.

[71] Massimiliano Bellomo. Measurement of the inclusive $W^{\pm}$ and Z/γ^* cross sections in the e and μ decay channels in pp collisions at $\sqrt{s} = 7$ TeV with the ATLAS detector. *PoS*, EPS-HEP2011:325, 2011.

[72] Georges Aad et al. Measurement of the inclusive $W^{\pm}$ and Z/γ^{*} cross sections in the electron and muon decay channels in pp collisions at $\sqrt{s} = 7$ TeV with the ATLAS detector. *Phys.Rev.*, D85:072004, 2012.

[73] G. Aad et al. Measurement of the $W \to \ell\nu$ and $Z/\gamma^{*} \to \ell\ell$ production cross sections in proton-proton collisions at $\sqrt{s} = 7$ TeV with the ATLAS detector. *JHEP*, 1012:060, 2010.

[74] HERA - A Proposal for a Large Electron Proton Colliding Beam Facility at DESY. 1981. DESY-HERA-81-10.

[75] U. Holm (ed) [Zeus Coll]. The ZEUS Detector. Status Report (unpublished). DESY, 1993. available at: http://www-zeus.desy.de/bluebook/bluebook.html.

[76] A. Polini et al. The design and performance of the ZEUS Micro Vertex detector. *Nucl.Instrum.Meth.*, A581:656–686, 2007.

[77] S. Fourletov. Straw tube tracking detector (STT) for ZEUS. *Nucl.Instrum.Meth.*, A535:191–196, 2004.

[78] N. Harnew, G. P. Heath, M. D. Jeffs, J. Nash, G. Salmon, et al. Vertex Triggering Using Time Difference Measurements in the ZEUS Central Tracking Detector. *Nucl.Instrum.Meth.*, A279:290–296, 1989.

[79] B. Foster, G. P. Heath, T. J. Llewellyn, D. M. Gingrich, N. Harnew, et al. The Performance of the Zeus central tracking detector z-by-timing electronics in a transputer based data acquisition system. *Nucl.Phys.Proc.Suppl.*, 32:181–188, 1993.

[80] B. Foster et al. The Design and construction of the ZEUS central tracking detector. *Nucl.Instrum.Meth.*, A338:254–283, 1994.

[81] M. Derrick, D. Gacek, N. Hill, B. Musgrave, R. Noland, et al. Design and construction of the ZEUS barrel calorimeter. *Nucl.Instrum.Meth.*, A309:77–100, 1991.

[82] A. Andresen et al. Construction and beam test of the ZEUS forward and rear calorimeter. *Nucl.Instrum.Meth.*, A309:101–142, 1991.

[83] A. Caldwell, I. Gialas, S. Mishra, J. Parsons, S. Ritz, et al. Design and implementation of a high precision readout system for the ZEUS calorimeter. *Nucl.Instrum.Meth.*, A321:356–364, 1992.

[84] A. Bernstein et al. Beam tests of the ZEUS barrel calorimeter. *Nucl.Instrum.Meth.*, A336:23–52, 1993.

[85] J. Andruszkow et al. First measurement of HERA luminosity by ZEUS lumi monitor. DESY-92-066. 1992.

[86] M. Derrick et al. Measurement of total and partial photon proton cross-sections at 180-GeV center-of-mass energy. *Z.Phys.*, C63:391–408, 1994.

[87] J. Andruszkow et al. Luminosity Measurement in the ZEUS Experiment. *Acta.Phys.Pol.* **B32** *2025.*

[88] W. H. Smith, K. Tokushuku, and L. W. Wiggers. The ZEUS trigger system. DESY-92-150B. 1992.

[89] U. Schneekloth. The HERA luminosity upgrade. 1998.

[90] D. P. Barber, M. Boge, H. D. Bremer, R. Brinkmann, E. Gianfelice-Wendt, et al. The First achievement of longitudinal spin polarization in a high-energy electron storage ring. *Phys.Lett.*, B343:436–443, 1995.

[91] F. D. Aaron et al. Inclusive Deep Inelastic Scattering at High Q^2 with Longitudinally Polarised Lepton Beams at HERA. *JHEP*, 1209:061, 2012.

[92] W. H. Smith, I. Ali, B. Behrens, C. Fordham, C. Foudas, et al. The ZEUS calorimeter first level trigger. *Nucl.Instrum.Meth.*, A355:278–294, 1995.

[93] G. P. Heath, B. Foster, T. L. Short, S.S. Wilson, M. Lancaster, et al. The ZEUS first level tracking trigger. *Nucl.Instrum.Meth.*, A315:431–435, 1992.

[94] A. Quadt, R. C. E. Devenish, S. Topp-Jorgensen, M. Sutton, H. A. J. R. Uijterwaal, et al. The Design and performance of the ZEUS central tracking detector second level trigger. *Nucl.Instrum.Meth.*, A438:472–501, 1999.

[95] U. Behrens, L. Hagge, and W. O. Vogel. THE ZEUS eventbuilder: Experience with a distributed real time parallel transputer system. 1993.

[96] S. Bhadra, M. Crombie, D. P. Kirkby, and R. S. Orr. The ZEUS third level trigger system. *Comput.Phys.Commun.*, 57:321–324, 1989.

[97] G. F. Hartner et al. VCTRAK (3.07./04): Offline Output Information. 1997.

[98] G. F. Hartner et al. VCTRAK Briefing: Program and Math. 1998.

[99] A. Spiridonov. Mathematical Framework for Fast and Rigorous Track Fit for the ZEUS Detector. 2008.

[100] R. Fruhwirth and A. Strandlie. Track fitting with ambiguities and noise: a study of elastic tracking and nonlinear filters. *Comp. Phys. Comm.*, **120**:197, 1999.

[101] G. M. Briskin. Diffractive dissociation in ep deep inelastic scattering. DESY-THESIS-1998-036. 1998.

[102] H. Abramowicz, A. Caldwell, and R. Sinkus. Neural network based electron identification in the ZEUS calorimeter. *Nucl.Instrum.Meth.*, A365:508–517, 1995.

[103] R. Sinkus and T. Voss. Particle identification with neural networks using a rotational invariant moment representation. *Nucl.Instrum.Meth.*, A391:360–368, 1997.

[104] S. Catani, B. Webber, and Y. Dokshitzer. The K(T) clustering algorithm for jets in deep inelastic scattering. *Nucl.Phys.Proc.Suppl.*, 29A:136–143, 1992.

[105] S. Catani, Y. L. Dokshitzer, M. H. Seymour, and B. R. Webber. Longitudinally invariant K_t clustering algorithms for hadron hadron collisions. *Nucl.Phys.*, B406:187–224, 1993.

[106] S. D. Ellis and D. E. Soper. Successive combination jet algorithm for hadron collisions. *Phys.Rev.*, D48:3160–3166, 1993.

[107] R. E. Kalman. A New Approach to Linear Filtering and Prediction Problems. *Transactions of the AMS Journal of Basic Engineering*, **D 82**:35, 1960.

[108] D. Nicholass. Measurement of $D^{\pm}$ meson cross sections in deep inelastic scattering using the ZEUS micro vertex detector. *DIS Conference Proceedings*, pages 809–812, 2007.

[109] A. Spiridonov. Evaluation of Beam Spot Size. 2009.

[110] J. E. Huth, N. Wainer, K. Meier, N. Hadley, F. Aversa, et al. Toward a standardization of jet definitions. 1990.

[111] S. Bentvelsen, J. Engelen, and P. Kooijman. Reconstruction of (x, Q^2) and extraction of structure functions in neutral current scattering at HERA. 1992.

[112] F. Jacquet and A. Blondel. Detection and Study of the charged current event. 1992. Proc. for the Study of an *ep* Facility for Europe. U. Amaldi (ed.). Hamburg. Germany. DESY 79/48 (1979).

[113] N. Metropolis and S. Ulam. The Monte Carlo Method. *J Am Statist Assoc*, 44:335–341, 1949.

[114] T. Sjöstrand. Monte Carlo Generators. pages 51–74, 2006.

[115] R. Brun, F. Bruyant, M. Maire, A. C. McPherson, and P. Zanarini. GEANT3. 1987.

[116] S. Agostinelli et al. GEANT4: A Simulation toolkit. *Nucl.Instrum.Meth.*, A506:250–303, 2003.

[117] J. Allison, K. Amako, J. Apostolakis, H. Araujo, P. A. Dubois, et al. Geant4 developments and applications. *IEEE Trans.Nucl.Sci.*, 53:270, 2006.

[118] H. Jung. Hard diffractive scattering in high-energy e p collisions and the Monte Carlo generator RAPGAP. *Comput.Phys.Commun.*, 86:147–161, 1995.

[119] B. Andersson, G. Gustafson, G. Ingelman, and T. Sjöstrand. Parton Fragmentation and String Dynamics. *Phys.Rept.*, 97:31–145, 1983.

[120] T. Sjöstrand. Jet fragmentation of nearby partons. *Nucl.Phys.*, B248:469, 1984.

[121] B. Andersson. The Lund model. *Camb.Monogr.Part.Phys.Nucl.Phys.Cosmol.*, 7:1–471, 1997.

[122] M. G. Bowler. e+ e- Production of Heavy Quarks in the String Model. *Z.Phys.*, C11:169, 1981.

[123] B. Andersson, G. Gustafson, and B. Soderberg. A General Model for Jet Fragmentation. *Z.Phys.*, C20:317, 1983.

[124] L. Lonnblad. ARIADNE version 4: A Program for simulation of QCD cascades implementing the color dipole model. *Comput.Phys.Commun.*, 71:15–31, 1992.

[125] L. Lonnblad. Rapidity gaps and other final state properties in the color dipole model for deep inelastic scattering. *Z.Phys.*, C65:285–292, 1995.

[126] Y. I. Azimov, Y. L. Dokshitzer, V. A. Khoze, and S. I. Troian. The String Effect and QCD Coherence. *Phys.Lett.*, B165:147–150, 1985.

[127] G. Gustafson. Dual Description of a Confined Color Field. *Phys.Lett.*, B175:453, 1986.

[128] B. Andersson, G. Gustafson, L. Lonnblad, and U. Pettersson. Coherence Effects in Deep Inelastic Scattering. *Z.Phys.*, C43:625, 1989.

[129] K. Charchula, G. A. Schuler, and H. Spiesberger. Combined QED and QCD radiative effects in deep inelastic lepton - proton scattering: The Monte Carlo generator DJANGO6. *Comput.Phys.Commun.*, 81:381–402, 1994.

[130] G. A. Schuler and H. Spiesberger. DJANGO: The Interface for the event generators HERACLES and LEPTO. 1991.

[131] G. Ingelman, A. Edin, and J. Rathsman. LEPTO 6.5: A Monte Carlo generator for deep inelastic lepton - nucleon scattering. *Comput.Phys.Commun.*, 101:108–134, 1997.

[132] A. Kwiatkowski, H. Spiesberger, and H. J. Mohring. HERACLES: An event generator for e p interactions at HERA energies including radiative processes: version 1.0. *Comput.Phys.Commun.*, 69:155–172, 1992.

[133] T. Sjöstrand. High-energy physics event generation with PYTHIA 5.7 and JETSET 7.4. *Comput.Phys.Commun.*, 82:74–90, 1994.

[134] P. G. Roloff. Measurement of charm and beauty production in deep inelastic scattering at HERA. DESY-THESIS-2011-049. 2011.

[135] V. Libov. Measurement of charm production in DIS with inclusive secondary vertices and determination of $F_2^{c\bar{c}}$ with the ZEUS detector at HERA. DESY Thesis. 2012.

[136] A. G. Yagues Molina. Study of beauty photoproduction with the ZEUS experiment at the electron-proton collider HERA. 2007.

[137] V. E. Schonberg. Measurement of beauty and charm photoproduction using inclusive secondary vertexing with the ZEUS detector at HERA. 2010.

[138] F. D. Aaron et al. Measurement of Charm and Beauty Jets in Deep Inelastic Scattering at HERA. *Eur.Phys.J.*, C71:1509, 2011.

[139] B. W. Harris and J. Smith. Charm quark and D*+- cross-sections in deeply inelastic scattering at HERA. *Phys.Rev.*, D57:2806–2812, 1998.

[140] M. R. Whalley, D. Bourilkov, and R. C. Group. The Les Houches accord PDFs (LHAPDF) and LHAGLUE. 2005.

[141] D. Bourilkov, R. C. Group, and M. R. Whalley. LHAPDF: PDF use from the Tevatron to the LHC. 2006.

[142] O. Behnke. Track efficiency tests with K_S^0 decays. Talk at the ZEUS Heavy Flavour Meeting. 25.03.2010. DESY Hamburg.

[143] M. Wing. Setting the jet energy scale for the ZEUS calorimeter. 10th International Conference on Calorimetry in High Energy Physics. Conference Proceedings. pp. 767-772, 2002.

[144] S. Lammers and D. Chapin. Jet Energy Scale Uncertainty. Internal ZEUS Note. ZEUS01-006, 2001.

[145] E. Maddox. Study of heavy quark production at HERA using the ZEUS microvertex detector. 2004.